eman ta zabal zazu

Universidad del País Vasco

Euskal Herriko Unibertsitatea

Exploiting magnetic dipolar interactions in artificially nanostructured systems

Jose Mª Porro Azpiazu

-Phd Thesis-

Supervisor: Prof. Paolo Vavassori

2014

Jose Mª Porro Azpiazu

Supervisor: Prof. Paolo Vavassori

Donostia-San Sebastián, 2014

“Ametsik gabeko bizia,
izarrik gabeko gaua.”

1. Resumen de la tésis

Hoy en día los avances tecnológicos están íntimamente ligados a la miniaturización de los dispositivos que los componen. Los fenómenos físicos que tienen lugar en la nanoescala trasladan los límites de eficiencia de los dispositivos hasta valores de rendimiento nunca antes alcanzados. Precisamente este hecho, junto con la mejora de la tecnología actual o la generación de nuevas tecnologías, es lo que mueve a la comunidad científica a investigar los nuevos límites dados por la nanociencia. Algunos de los sectores tecnológicos actuales, tales como la electrónica, el almacenamiento de datos y la industria de los ordenadores, son los que están continuamente luchando contra los límites de los materiales y dispositivos que existen actualmente, intentando superar dichos límites haciendo dispositivos mejores, más rápidos y más baratos. Otras industrias, tales como la farmacéutica o la médica, también están inmersos en el desarrollo de nuevos materiales y dispositivos novedosos, tales como sensores biofísicos para aplicación en la medicina.

Estos avances tecnológicos vienen junto con otros muchos, como son mejoras en la implementación de dispositivos de magnetorresistencia gigante para cabezas lectoras en discos duros, la investigación sobre los dominios magnéticos en materiales granulares para almacenamiento de datos, detección de campos magnéticos en sensores de automoción, memorias de acceso aleatorio magnéticas (MRAMs) y muchos otros. También en la industria de la información la nanociencia y los nuevos fenómenos que conlleva pueden ser implementados, por ejemplo para fabricar ordenadores cuánticos basados en la electrónica de espín, y algunos otros conceptos más avanzados.

El nanomagnetismo es el estudio de los nuevos fenómenos físicos que surgen cuando los sistemas magnéticos se reducen a la escala nanométrica. El control preciso de la nanoestructura ofrecido por las modernas técnicas de litografía

hace posible fabricar muestras con estructuras por debajo de una micra de tamaño hechas de materiales magnéticos. Este nuevo control sobre el tamaño, los periodos (en muestras con patrones de nanoestructuras definidos) y la simetría de las nanoestructuras permite la fabricación no sólo de nuevos sistemas con un enorme potencial tecnológico, sino también de sistemas en los cuales las propiedades fundamentales de la materia en la nanoescala pueden ser investigadas. La correlación entre las propiedades magnéticas de muestras con patrones de nanoestructuras definidas con el tamaño y la forma de cada unidad que compone la muestra, es un tema de gran importancia que está siendo investigado enormemente en los últimos tiempos. Un aspecto esencial en física fundamental y en la industria de dispositivos de almacenamiento de datos es entender y controlar la inversión de la magnetización en nanoelementos magnéticos. El entendimiento del magnetismo en la escala nanométrica hará posible la fabricación de dispositivos de electrónica de espín, a pesar de que todavía hay muchas cuestiones sin resolver.

Las propiedades magnéticas de estructuras nanométricas están siendo investigadas continuamente, haciendo uso de una gran variedad de técnicas experimentales. En muchos casos no sólo la física de estructuras magnéticas nanométricas es objeto de estudio, sino que también se estudia cómo las técnicas experimentales son capaces de evolucionar. El aumento del esfuerzo dedicado al estudio de sistemas periódicos de nanoestructuras magnéticas conlleva el desarrollo de nuevas técnicas experimentales para investigar su comportamiento.

Los procesos magnéticos están caracterizados por escalas de longitud específicas, y surgen nuevos fenómenos cuando las dimensiones de los materiales magnéticos están en la nanoescala. Las escalas de longitud características del nanomagnetismo tienen orígenes diversos. Muchas de ellas están gobernadas por procesos de minimización energética, tales como la anchura de paredes de dominio, la longitud de exchange o la anisotropía perpendicular en películas magnéticas delgadas. Otras, como las longitudes de difusión o de precesión de espín, son el resultado de procesos de difusión de

energía, momento o magnetización. En un dispositivo magnético nanoestructurado pueden estar implicadas muchas posibles combinaciones de esas escalas de longitudes características, dando lugar a procesos muy diversos en dichos dispositivos.

Probablemente la escala de longitud característica más fundamental es la longitud de exchange. Haciendo un balance de los términos energéticos presentes en un imán nanométrico (exchange, magnetostático, anisotropía y Zeeman) se crean dominios magnéticos en el material. Estos dominios son regiones donde todos los momentos magnéticos están apuntando en la misma dirección. El tamaño de los dominios magnéticos, así como la anchura de las zonas entre dos dominios (las paredes de dominio, donde los espines rotan desde la dirección de un dominio hasta la del otro) está gobernado por esos términos energéticos.

El objetivo de la presente tesis es estudiar el efecto de las interacciones entre estructuras nanomagnéticas, en muestras tanto periódicas como no periódicas, para comprobar el efecto que producen en la magnetización de las nanoestructuras. Así, se han estudiado varios casos diferentes en los cuales las interacciones dipolares están presentes: interacciones dipolares asimétricas y locales, acomodación de la frustración magnética por medio de interacciones dipolares simétricas, y efecto del campo dipolar producido por el desplazamiento de paredes de dominio en la magnetización de nanoestructuras magnéticas adyacentes. Para ello, esta tesis se ha dividido en varios capítulos; en el primer capítulo se resumen los conocimientos básicos del ferromagnetismo necesarios para entender los fenómenos magnéticos estudiados en la tesis, discutiéndose los términos energéticos que contribuyen a la energía total de un material ferromagnético, así como la formación de dominios y paredes de dominio, y el fenómeno de histéresis magnética.

En el capítulo 3 se describe el procedimiento seguido para la fabricación de las muestras objeto de estudio de esta tesis. De entre las múltiples posibilidades que existen para hacer muestras nanométricas se ha seleccionado la técnica de

litografía por haz de electrones. En este capítulo se describe el proceso completo de nanolitografía por medio de esta técnica, basada en la utilización de un haz focalizado de electrones que incide sobre un material polimérico sensible a la exposición de corrientes de electrones.

La técnica en sí consiste en aplicar una capa de un polímero sensible a los electrones (resina) sobre el sustrato en el que se desea obtener las nanoestructuras. Este sustrato con la capa polimérica se expone a un haz de electrones, que recorre un patrón previamente introducido mediante software, con precisión nanométrica. Una vez que el polímero se ha expuesto a la corriente de electrones, se sumerge en un disolvente químico (revelador) que hace que las partes expuestas a la corriente de electrones se disuelvan (en el caso de resina positiva; si la resina es negativa las partes no expuestas son las que se disuelven), quedando el patrón introducido en el software replicado en la resina polimérica. Después, mediante el uso de una técnica de deposición, se deposita el material sobre los restos de resina y el sustrato. Por último, la muestra se somete a un proceso de "lift-off", mediante el cual los restos de resina (y el material depositado encima de ella) se separan del sustrato, quedando por tanto la nanoestructura introducida mediante software replicada en el sustrato utilizado.

En el capítulo 4 se describen las técnicas experimentales utilizadas para la caracterización de las muestras fabricadas por medio de litografía de haz de electrones. Para caracterizar la topografía se ha hecho uso de un microscopio de fuerza atómica (AFM), capaz de medir con resolución nanométrica la superficie de las muestras, mientras que para conocer el espesor de las películas magnéticas depositadas se ha usado la técnica de reflectividad de rayos-X. En lo que respecta a técnicas de caracterización magnética, una de las principales técnicas utilizadas ha sido la microscopía de fuerza magnética (MFM). Haciendo uso de un microscopio de fuerza atómica, si se monta una punta con revestimiento magnético, el campo creado por la punta magnética interacciona con el campo que crea una muestra magnética, posibilitando el estudio de dominios y paredes de dominio de muestras magnéticas. Otra técnica muy utilizada ha sido la magnetometría/microscopía MOKE, basada en el efecto Kerr

magneto-óptico. Por medio de esta técnica ha sido posible medir ciclos de histéresis en muestras magnéticas, tanto en haces de luz reflejados como difractados (en el caso de muestras periódicas), siendo esta última técnica (diffracted-MOKE) muy poderosa en cuanto a resultados de caracterización magnética se refiere. También ha sido posible medir ciclos de histéresis locales en nanoestructuras por medio de la microscopía MOKE.

En el capítulo 5 se introduce el concepto de dinámica de magnetización, explicando en qué consiste y cuáles son las leyes que lo rigen, entre ellas la ecuación de Landau-Lifshitz-Gilbert de la dinámica de magnetización. Esta ecuación es la base del código de simulaciones micromagnéticas OOMMF, usado para realizar la mayoría de simulaciones presentadas en esta tesis, y que también se introduce en este capítulo.

En los siguientes tres capítulos (6, 7 y 8) se describen los resultados experimentales obtenidos. El primero de ellos hace referencia al estudio de interacciones dipolares localmente asimétricas entre nanoelipses ferromagnéticas, estudiando el proceso de inversión de la magnetización en patrones de nanoislas cuya unidad simple está compuesta por cuatro nanoislas, dispuestas de tal forma que las interacciones dipolares entre nanoislas vecinas provoquen una asimetría del campo dipolar que actúa en ellas. Las nanoislas tienen tamaños alargados, por lo que el estado magnético de energía más baja posible en ellas sería tener magnetización uniforme.

En el proceso de investigación de la inversión de la magnetización se ha encontrado que, dependiendo de la dirección en la que se aplique el campo magnético externo, existen dos caminos diferenciados para la inversión de la magnetización. En el caso en el que el campo está aplicado en una dirección arbitraria, la inversión de la magnetización se realiza observando estados de magnetización uniformes en todas las nanoislas. Sin embargo, cuando el campo externo se aplica hasta 2° desviado del eje fácil de dos de las nanoislas que forman el cuadrado unidad, el proceso de inversión ocurre por medio de la formación y desplazamiento de un estado de vórtice magnético en las nanoislas

cuyo eje fácil es perpendicular al campo aplicado. Este estado magnético de vórtice se encuentra estable en remanencia, a pesar de ser energéticamente muy desfavorable respecto al estado de magnetización uniforme. Este hecho es debido a las dinámicas de magnetización inducidas por la asimetría dipolar local presente en las nanoislas que forman la muestra, y este proceso inusual de la inversión de la magnetización se ha encontrado para varios tamaños de nanoislas.

El segundo capítulo experimental trata del acceso al estado fundamental de energía en estructuras artificiales de "spin-ice". Las estructuras artificiales de "spin-ice" son estructuras magnéticas que imitan el comportamiento de las estructuras "spin-ice" formadas por aleaciones de metales y tierras raras que, a su vez, imitan el comportamiento de la estructura cristalina de moléculas de agua cuando se congelan a cero Kelvin. Estas estructuras cristalinas de agua poseen la denominada "entropía residual": cuando se congelan hasta llegar al cero absoluto de temperatura, el estado mínimo de energía no está únicamente determinado; existen dos estados degenerados de mínima energía, dando lugar a un desorden intrínseco en el estado de mínima energía del sistema a cero Kelvin.

En estructuras artificiales de "spin-ice", las nanoelipses ferromagnéticas que las componen pueden tratarse como "macroespines", ya que siempre presentan un estado de magnetización uniforme. Estas nanoelipses son dispuestas geométricamente de tal forma que presentan una simetría que, en el estado de mínima energía del sistema, produce el mismo efecto que en las estructuras cristalinas de agua helada: no hay un estado de mínima energía único. El trabajo desarrollado en esta tesis permite, por medio de un protocolo de demagnetización termal (llevando el sistema por encima de la temperatura de Curie), estudiar el estado de mínima energía formado en la estructura de "spin-ice" de una manera reproducible. Hasta ahora los protocolos de demagnetización de este tipo de estructuras no habían conseguido llegar a estados de ordenación del estado fundamental de energía tan grandes de una manera reproducible, por lo que este hecho supone un avance enorme en el estudio de estructuras artificiales de "spin-ice".

Por último, en el último capítulo de la parte de experimentos de la tesis se expone el efecto que produce el campo dipolar producido por una pared de dominio, la cual se desplaza por un conducto estrecho, en la magnetización de nanoislas localizadas en las proximidades de dicho conducto. En conductos estrechos y alargados hechos de material magnético es posible producir pulsos de campo ultrarrápidos e intensos, por medio de la introducción de paredes de dominio magnéticas. Para comprender mejor la forma y la intensidad de los pulsos de campos creados por paredes de dominio, es posible colocar nanoelipses ferromagnéticas en las proximidades del conducto por el que se desplaza la pared de dominio, de tal forma que estas actúen de sensor del pulso de campo creado. Así, dependiendo de la intensidad y forma del pulso de campo creado en la nanoisla, por medio de microscopía de fuerza magnética es posible comprobar si el pulso ha inducido un proceso de inversión de la magnetización en las nanoislas adyacentes al conducto. En esta tesis se ha estudiado la creación y desplazamiento de paredes de dominio en conductos estrechos y delgados, y el efecto que producen sobre la magnetización de partículas adyacentes, llegando a la conclusión de que es posible invertir la magnetización de dichas partículas en determinadas situaciones que son expuestas en este capítulo.

2. Introduction

2.1. Ferromagnetism at the nanoscale: nanomagnetism

Technology is, nowadays, miniaturizing more and more the devices. The phenomena occurring in the nanoscale place ultimate limits on device performance, improve current technology or generate new one, being these ultimate material or device engineering interests the ones moving and driving the research in this topic. Some technological sectors as the electronics, data storage and computer industry are the ones that continuously push the limits of their actual materials and devices, trying to make things better, faster and cheaper. Some other industries as medical technology are also involved in the development of novel materials and devices, such as biological physics sensors for medicine. These advances come together with improvements in the implementation of giant magnetoresistive devices for read heads in data storage, the investigations into domains in granular media for data storage, magnetic field sensing for automotive sensors, magnetic random access memories (MRAMs) and many others. Also in the information technology these novel phenomena can be implemented in order to fabricate quantum computers based on spin-electronics and some other more advanced concepts.

Nanomagnetism is the study of the novel physical phenomena appearing when magnetic systems are reduced to the nanoscale. The precise control of microstructure offered by modern lithography now makes it possible to produce samples composed of sub-micron structures in magnetic films. This new control over the sizes, periods and symmetry of the nanostructures enables not only the fabrication of new systems of potential technological interest, but also systems in which fundamental properties of mesoscopic matter can be investigated. The correlation of the magnetic properties of arrays of patterned structures to the size and shape of the single unit, as well as to the array spacing, is a central issue that is still being subject of many recent investigations. A key issue in

fundamental physics and data storage technology is to understand and control the magnetic switching of small magnetic elements. Much of the drive for these investigations is the hope that understanding magnetism at these length scales will enable advanced spintronic devices to be realized. In spite of the considerable effort so far devoted to investigate these problems, there are still many unanswered questions.

The magnetic properties of nanostructures are continuously being investigated using a variety of experimental techniques. In many cases it is not only the mesoscopic physics of magnetic nanostructures (dots, wires and holes) what is being probed, but also how the techniques themselves probe these novel structures must be evaluated. The ever increasing efforts devoted to the study of nanosize particle arrays is leading to the development of novel techniques for their investigation.

Magnetic processes are characterized by specific length scales, and novel phenomena arise when the dimensions of the magnetic materials are in the nanometer range. The characteristic length scales of nanomagnetism have various origins. Energy minimizations govern many of these length scales, such as domain walls width, exchange length or thin film perpendicular anisotropy; whereas others like the spin diffusion and spin precession lengths are the result of diffusion processes for energy, momentum or magnetization. In a nanoscaled magnetic device a wide variety of combinations of several of those characteristic length scales might be involved, being therefore the phenomena that appear on these devices very diverse.

Maybe the most fundamental of all the characteristic length scales is the exchange length. By balancing the energy associated with the exchange length, together with the other energy terms (magnetostatic, anisotropy and Zeeman, which are defined in the next section) present in a nanoscaled magnet, magnetic domains of different sizes and shapes are created. Magnetic domains are regions where all the spins inside that region of the material are pointing towards the same direction; i.e., the magnetization inside a magnetic domain is uniform. The

size of the magnetic domains, and the width of the regions between two neighboring domains (the so-called domain walls, where the spins are rotating from the direction followed by all the spins of one of the neighboring domains towards the direction to which all the spins in the other neighboring domain are pointing) are governed by these four energy terms. Many different types of domains exist depending on what energy contributions are dominant in each particular case, and also on the magnetic history of the material. Two nice reviews on nanomagnetism and its characteristic length scales and competing energy terms can be found in [1] and [2].

2.2. Energy contributions in nanomagnetism

The energy of every magnetic specimen depends on its magnetic structure. The total magnetization in a ferromagnet, in a static equilibrium state, is arranged so that the total energy is minimized, and that minimum can be either a local or a global minimum. The magnetic history of a ferromagnetic sample, called the hysteresis (which will be introduced in the next section), is decisive for the selection of the equilibrium configuration. In micromagnetism (and nanomagnetism) the most important contributions to the total energy are the exchange, magnetostatic and anisotropy energy terms, and when an external field is applied to a ferromagnetic sample, also the Zeeman energy term contributes to the total energy of the system. The four energy terms will be briefly discussed in the following paragraphs.

2.2.1. Exchange energy

The exchange energy term is responsible for the characteristic property of every ferromagnetic material, which is their tendency to keep neighboring magnetic moments parallel. It is determined by the angle between neighboring spins. The energy required to align anti-parallel one atomic spin with respect to its neighbors is called the exchange energy. It is a quantum-mechanical phenomenon induced by the Coulombic electrostatic interaction between

neighboring electrons, and the combination of the Pauli exclusion principle (two spins cannot possess the same m_s quantum number if they are in the same orbital and, therefore, will align antiparallel) and the Hund's rule (degenerated orbitals will tend to be occupied by a single electron, before filling them in pairs). The expression for this energy term follows:

$$E_{exchange} = -2\sum_{i>j} J_{ij}\vec{S}_i \cdot \vec{S}_j \qquad (2\text{-}1)$$

being J the exchange integral linking the i-th electron with spin S_i to the j-th electron with spin S_j., and is positive for ferromagnetic materials. The exchange integral involves the wavefunctions of the two interacting electrons, taking into account the antisymmetry of the electron wavefunctions. From the exchange integral another fingerprint quantity of ferromagnetism arises: the exchange stiffness constant A, strictly related to the exchange integral.

The exchange energy has a characteristic length over which the interaction among neighboring spins is no longer dominated by this energy term; it measures the relative strength of the exchange and magnetostatic energy terms, and is characteristic for each magnetic material. As an example, the exchange length of Permalloy is 5.3nm. There are some materials for which the exchange integral is negative, forcing neighboring spins to anti-align; those are the antiferromagnetic materials.

2.2.2. Magnetostatic energy

The magnetostatic energy is related to the magnetic field produced by the ferromagnetic sample itself or by different macroscopic regions of the material. Each magnetic moment composing a ferromagnetic sample contributes to a total magnetic field $\vec{H}_d$ inside the sample, which is often called 'demagnetizing field'. A sketch of the demagnetizing field on a uniformly magnetized sample can be observed in Figure 2-1.

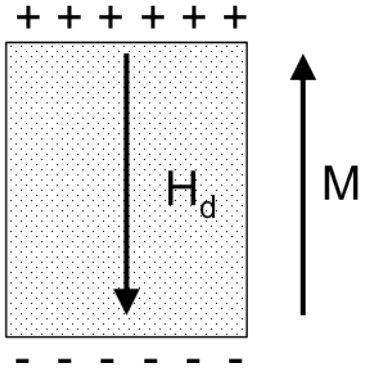

Figure 2-1: demagnetizing field created by the magnetic charges of a ferromagnetic sample, opposing to the direction of the magnetization.

The divergence of the magnetization inside the body is a source of free surface magnetic poles, which give rise to stray fields and, therefore, the sum of the potential energy of each magnetic moment inside the body in this field gives rise to the magnetostatic energy. The sinks and sources of magnetization act like magnetic charges that are always balanced. The magnetostatic energy is given by:

$$E_{magnetostatic} = -\frac{1}{2}\mu_0 \int_{sample} \vec{H}_d \cdot \vec{M} dV \qquad (2\text{-}2)$$

Different terms are used in literature to name the demagnetizing field, such as the magnetic stray field, the dipolar field, or the magnetostatic field. This field is created by the magnetic volume charges $\rho = -\vec{\nabla} \cdot \vec{M}$ and the magnetic surface charges $\sigma = \vec{M} \cdot \vec{n}$, where $\vec{n}$ is a unit vector perpendicular to the surface, and can be written as follows:

$$\vec{H}_d(\vec{r}) = -\frac{1}{4\pi}\left\{\int_{vol} \frac{(\vec{r}-\vec{r}\prime)\rho(\vec{r}\prime)}{|\vec{r}-\vec{r}\prime|^3} dV' - \int_{surf} \frac{(\vec{r}-\vec{r}\prime)\sigma(\vec{r}\prime)}{|\vec{r}-\vec{r}\prime|^3} dS'\right\} \qquad (2\text{-}3)$$

It can be shown that total stray field energy is always positive definite [3] and, therefore, it is not possible to arrange the magnetization in such a way that the stray field lowers the total energy. This means that, in order to minimize the

magnetostatic energy in a ferromagnetic sample, the sources of the stray field have to be minimized [4].

In a finite size uniformly magnetized ferromagnetic nanoelement, the volume charges are negligible compared to the surface charges, and the demagnetizing field can be written as a tensor relation as follows:

$$\vec{H}_d(\vec{r}) = -\widetilde{N} \cdot \vec{M}(\vec{r}) \qquad (2\text{-}4)$$

where $\widetilde{N}$ is a tensor containing demagnetizing factors. For an ellipsoid, this tensor takes a diagonal form and its three diagonal coefficients are the demagnetizing factors along the principal axes [5].

2.2.3. Anisotropy energy

Magnetic anisotropy means a dependence of the energy of a magnetic material on the direction along which its magnetization is aligned. The directions towards which the energy is minimum are called 'easy axes', whereas the directions where the energy is maximum are the 'hard axes'. There are several types of anisotropy, being the most common one the magnetocrystalline anisotropy, which is defined as the energy required to rotate the entire magnetization vector of the magnetic material without moving it or changing the relative orientation between spins. It results from the interaction between the crystalline fields of the magnetic material and the spin-orbit coupling. Therefore, when the magnetic moments are directed along the easy axes the energy is minimized. Along the hard axes the energy is maximized.

The simplest case of magnetocrystalline anisotropy is the uniaxial anisotropy, in which there is one preferred direction for the magnetic moments to be aligned parallel to it: the easy axis. The expression for the uniaxial anisotropy energy is given by:

$$E_{uniaxial} = K_u \cdot \left[1 - \left(\vec{M} \cdot \vec{k}\right)^2\right] \cdot V \qquad (2\text{-}5)$$

where K_u is the first order uniaxial anisotropy constant, and $\vec{k}$ is a unit vector parallel to the easy axis. The cubic magnetocrystalline anisotropy is another typical anisotropy case. The expression for the anisotropy energy for a cubic crystal is written as:

$$E_{cubic} = \left\{K_1\left[m_1^2 m_2^2 + m_1^2 m_3^2 + m_2^2 m_3^2\right] + K_2 m_1^2 m_2^2 m_3^2\right\} \cdot V \qquad (2\text{-}6)$$

where K_1 and K_2 are the first and second order magnetocrystalline anisotropy constants along the easy axis directions, and m_i are the components of the magnetization vector. The exchange energy dominates over the anisotropy energy, being their ratio on the orders between 10^{-3} and 10^{-5}.

Besides the magnetocrystalline anisotropy, another common source of magnetic anisotropy in finite objects is the so-called shape anisotropy, which describes how the particle shape can lead to the existence of preferred directions (easy axes) of the magnetization orientation in a ferromagnetic sample. As an example, an elongated ferromagnetic nanoisland with negligible magnetocrystalline anisotropy can have properties similar to those of a spherical particle with uniaxial magnetocrystalline anisotropy. Being that the case, Eq.(2-5) presented previously for the uniaxial magnetocrystalline anisotropy can be used as a shape anisotropy term, if the anisotropy constant is written as follows:

$$K = \frac{1}{2}\mu_0 M_S^2 \Delta N \qquad (2\text{-}7)$$

where ΔN is the difference between the demagnetizing factors along the in-plane short and long axes of the nanoisland. Nevertheless, the physical origin of the uniaxial magnetocrystalline anisotropy and the shape anisotropy is completely different.

2.2.4. Zeeman energy

The fourth energy contribution is the Zeeman energy, which is the potential energy of the magnetic body in the external applied field. It is given by the following expression:

$$E_{Zeeman} = -\mu_0 \int \vec{H}_{ext} \cdot \vec{M} dV \qquad (2\text{-}8)$$

being $\vec{H}_{ext}$ the external applied field. This energy term is only contributing when an external magnetic field is present, and its contribution to the total energy of the magnetic material depends on the strength of the external field. Therefore, for strong magnetic fields acting on a magnetic material this energy term will be the dominant one.

2.3. Magnetic domains & domain walls

Finite size magnetic bodies are often subdivided into domains, which are magnetized in different directions (i.e. the spins present in each magnetic domain point in the same direction, but the spins of different domains point in different directions). Weiss first proposed that a ferromagnetic material contains a certain amount of small regions called domains, within each of which the local magnetization reaches the saturation value [6]. The direction of the magnetization in different domains is not required to be parallel, and the regions that separate two domains with different magnetization directions are called domain walls. This existence of domains explains the observation that in some magnetic materials it is possible to attain saturation magnetization (all the spins in the magnet point in the same direction) in the whole sample by the application of a very weak magnetic field. This occurs because the applied magnetic field does not need to 'order' the magnetic moments macroscopically but to cause the domains to align, which can be accomplished by moving the domain walls, which is energetically almost costless (compared to the energy cost of aligning the spins in non-magnetic materials). It could also happen that the net magnetization

in a magnetic specimen is zero when a magnetic field is not being applied to it, which is a manifestation of the existence of domains where the magnetization is saturated on each of them, but the directions of their spins are such that the net magnetization of the specimen is zero [7].

The existence of magnetic domains is a well-established experimental fact, as they have been observed by different techniques. The oldest observations include the Bitter pattern [8], where tiny magnetic particles suspended in a liquid are attracted to the high surface field at the walls that separate the domains, revealing therefore the presence of these domain walls.

Another method to detect domains and domain walls is based on scanning the magnetic field near the sample by a very small Hall probe [9], and more recent methods include passing a current through the sample and measuring the Hall effect at different points, oppositely magnetized domains give an opposite sign of the Hall voltage [10]. Modern techniques such as Magnetic Force Microscopy (MFM), which is a technique used in the present thesis, are capable of imaging the magnetic domains or the boundaries between them (domain walls) [11].

The two main mechanisms by which the magnetization can rotate continuously, from the direction of one domain towards the other, are the so-called Bloch and Néel domain wall types. They are the simplest wall types, and represent idealized situations; in reality more domain wall types can be found, such as cross-tie, asymmetric Bloch or asymmetric Néel walls, which are domain walls that display combinations of both fundamental types: the Bloch and Néel walls.

2.3.1. Bloch wall

Bloch domain walls are likely to be found in bulk ferromagnetic materials with uniaxial anisotropy, and the magnetization in the domain wall remains always perpendicular to the wall normal, around which it rotates by 180° in the domain

wall region (see Figure 2-2). The involved energy terms in a Bloch wall are the exchange and anisotropy energies. The exchange energy is minimized if the domain wall is wide; i.e. if the transition from one domain to the other occurs over a large distance smoothly, because the angles between neighboring magnetic moments are small. On the contrary, the anisotropy energy term tends to reduce the width of the domain wall as much as possible in order to align the magnetization with the easy axes of the anisotropic sample.

A common definition of the domain wall width δ_B [12] can be written in the following form:

$$\delta_B = \pi\sqrt{A/K} \tag{2-9}$$

where A and K are the exchange stiffness and anisotropy constants of the ferromagnetic material. The energy density of a Bloch wall, which is defined as the energy per unit area of the domain wall, is:

$$\gamma_B = 4\sqrt{AK} \tag{2-10}$$

An important property of the Bloch wall is that the magnetization distribution is free of divergence, meaning that there are no bulk charges formed which do not create any magnetostatic field. Neglecting the surface charges, as bulk material is assumed, there are no sources of magnetic charges and, therefore, it is legitimate to neglect the magnetostatic energy term for the derivation of Eqs.(2-9) and (2-10).

2.3.2. Néel wall

On the contrary to what occurs with Bloch walls, Néel walls are likely to be found in thin ferromagnetic nanostructures and films. The main difference between the two domain wall types is that in Néel walls magnetostatic fields are not negligible, as in thin films the relative impact of the magnetostatic energy

connected to the field created by the surface charges is much larger. Louis Néel demonstrated that it is energetically more favorable for the magnetic moments to perform the change of the magnetization direction by rotating them in the thin film plane [13] (see Figure 2-2).

In this type of walls the competing interactions are given by the magnetostatic and exchange energies, with the magnetostatic term tending to keep the domain wall as small as possible, being balanced by the tendency of the exchange term to avoid strong inhomogeneities of the magnetization. The domain wall width and energy densities for a Néel wall are given by similar expressions to Eqs.(2-9) and (2-10), but the anisotropy constant changes from the case of a Bloch wall to here. Whereas in a Bloch wall the magnetostatic energy term can be neglected, in a Néel wall the anisotropy constant can be cast as a sum of the pure anisotropy plus an 'stray field constant', $K=K_a+K_d$, where the stray field constant has this shape: $K_d = \mu_0 M_S^2/2$.

The selection between the two domain wall types is primarily given by the thickness of the magnetic material. In thick samples Block walls are preferred, whereas for thin samples Néel walls are more favorable to occur. In Figure 2-2 the two domain wall types (Bloch and Néel) are schematized.

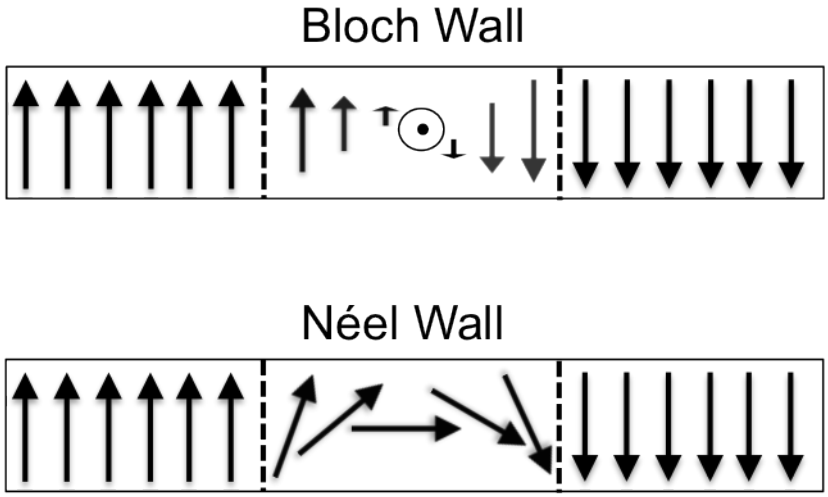

Figure 2-2: Schematics of a Bloch and a Néel walls in a ferromagnetic material.

2.3.3. Domain walls in thin ferromagnetic nanostripes

In thin, narrow and long ferromagnetic nanostructures, tipically few hundreds of nanometers wide and few tens of nanometers thick (nanostripes), another class of domain walls has recently moved into the focus of interest of nanomagnetism. The domain walls formed in nanostripes are the so-called head-to-head or tail-to-tail walls, because the magnetization along the stripe is usually parallel to the long axis of the nanostructure (apart from the domain wall region).

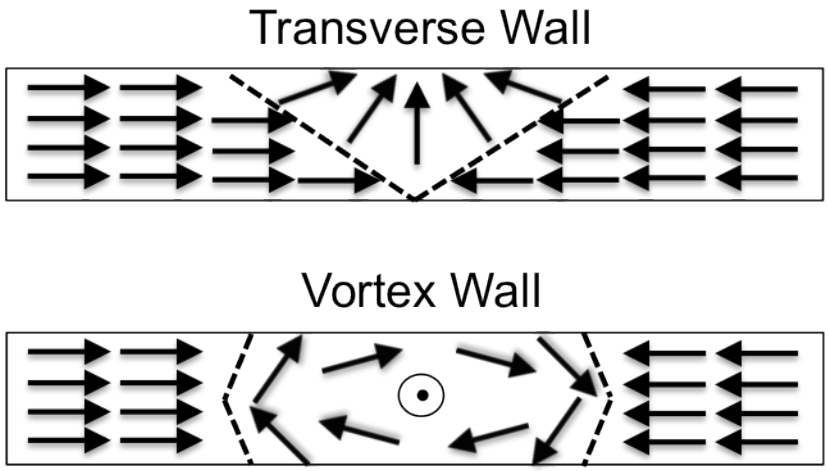

Figure 2-3: Schematics of a transverse and a vortex wall in a ferromagnetic nanostripe.

Two different domain wall types have been observed in nanostripes: transverse and vortex walls, sketched in Figure 2-3. In the case of the transverse wall the spins are rotating in the plane of the nanostripe, whereas in the case of the vortex wall the spins curl clockwise or counter-clockwise around a vortex core, where the magnetization is pointing out of the plane of the nanostripe. The transverse domain wall exhibits a V-shaped wall in order to minimize its energy.

The energies of the transverse and vortex domain walls depend on the geometry and material of the nanostripe. An analytical calculation of the energies as a function of these two parameters is found in [14]. Assuming that the difference in stray field energies between the two types of domain walls is effectively the stray field of the in-plane component of the transverse domain wall (in the case

of the vortex wall this component of the stray field is much smaller), the magnetostatic energy difference can be written as:

$$\Delta E_{magn} \approx -\frac{1}{8}\mu_0 M_S^2 t^2 w \qquad (2\text{-}11)$$

where t is the thickness and w the width of the nanostripe, and M_S is the magnetization saturation of the material of which the nanostripe is made. For the difference in the exchange it is considered that it is the one given by the vortex in the vortex wall:

$$\Delta E_{exch} \approx 2\pi t A \cdot ln\frac{r_{max}}{r_{min}} \qquad (2\text{-}12)$$

where A is the exchange constant of the material, and r_{max} and r_{min} are the outer and inner radius of the vortex. The outer radius is usually taken to be half of the width of the nanostripe, and the inner radius is given by the vortex core radius. From these two equations it is possible to deduce a phase diagram (Figure 2-4) that determines which is the energetically favorable domain wall in a nanostripe made of a certain material and with defined width and thicknesses.

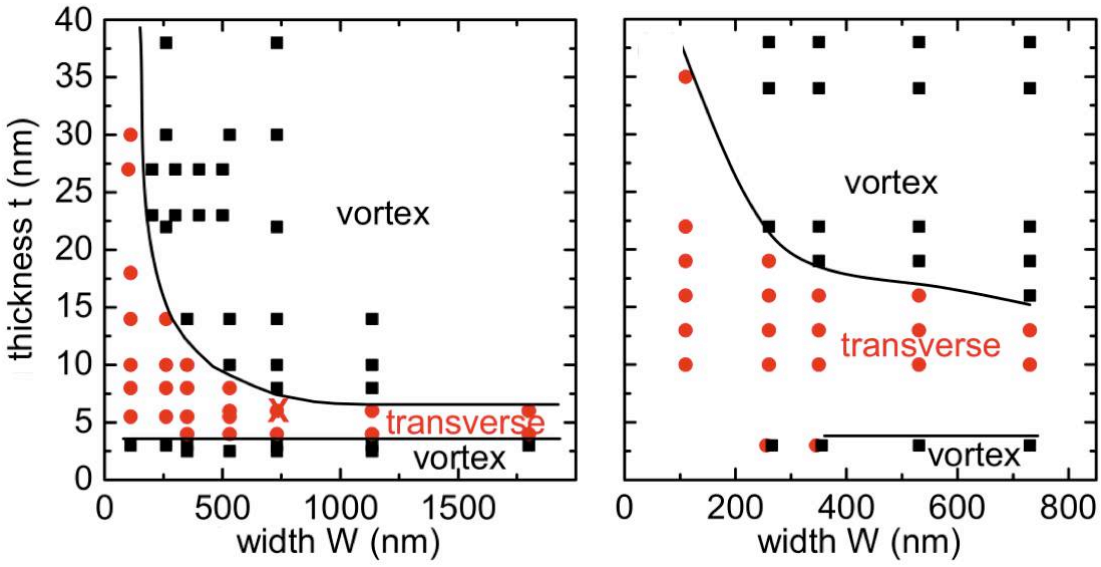

Figure 2-4: Phase diagrams for head-to-head domain walls in Permalloy (left) and Cobalt (right) nanostripes, showing the regions in which vortex and transverse domain walls are energetically preferred as a function of the dimensions of the nanostripe. Adapted from [15].

2.4. Hysteresis loops

One of the most distinctive fingerprints of ferromagnetism is the observation of the magnetic hysteresis phenomenon. A hysteresis loop is a curve obtained by applying a cyclic magnetic field to a ferromagnetic material and recording the changes that it provokes on the magnetization of the material. It is well known that ferromagnetic materials exhibit large spontaneous magnetization at low magnetic field, and even in the absence of any field, because the magnetic moments composing the ferromagnet are strongly coupled to an internal field that is proportional to the magnetization: the molecular field. Pier Weiss proposed this idea in 1907. Due to the existence of this molecular field, below a critical temperature, which is called the Curie temperature T_C and is characteristic of each ferromagnetic material, the magnetic moments exhibit long-range order and the ferromagnetic material presents a spontaneous magnetization M_S, also characteristic of the material.

But the existence of a molecular field implies that every ferromagnetic material would always be spontaneously magnetized to saturation, and small magnetic fields would not be capable of reducing the total magnetization of a ferromagnet to zero. This 'problem' was also solved by Weiss, who proposed that a ferromagnetic material is divided into domains, as has been mentioned in the previous section. As a consequence of the existence of magnetic domains, when the magnetization is averaged over volumes large enough to contain many domains, the value of the total magnetization of the ferromagntet is determined by the relative orientation and size of the domains.

The differences in shape of the hysteresis loops are a consequence of the variety of possible magnetic domain structures. The competing energy terms defined in the previous section (exchange, magnetostatic and anisotropy, plus Zeeman when under the action of an external field) define the domain structure of a ferromagnetic material. Exchange energy favors uniform magnetization configurations, magnetostatic energy favors magnetization configurations giving a null average magnetic moment, anisotropy energy favors the magnetization to

be oriented along certain directions and Zeeman favors aligning the magnetization with the direction of the external field. Depending on the strength of each energy term the domain structure will change. When the external field varies in time, the energy balance between the four energy terms rearranges the domain structure of the ferromagnet, and the domain walls that separate magnetic domains are displaced. The domains that have their net magnetization pointing in the direction in which the external field is applied are energetically favored and grow, 'eating' the surrounding domains and eventually forcing them to disappear. When the external field reaches certain intensity, the ferromagnet has all its magnetic moments aligned to the applied field. When the field is reversed, domains of reversed magnetization are formed, which will progressively increase in size via domain wall displacements, up to a point in which the external field is so intense that a single domain of reversed magnetization is formed.

Apart from the formation and motion of magnetic domains, there are other magnetization reversal mechanisms in ferromagnetic materials, such as the coherent rotation of the magnetization in uniformly magnetized samples. This reversal mechanism can be explained by means of the so-called Stoner-Wohlfarth model, which is discussed in Chapter 8 of this thesis, and states that the magnetic moments in a uniformly magnetized sample can be considered as a macrospin, which rotates in order to align to the external applied field.

A magnetization reversal process in a ferromagnetic sample is sketched in Figure 2-5, including coherent rotation (from (a) to (b) and from (e) to (f)) and domains nucleation and propagation (between (b) and (e)). The different configurations of the magnetic domains in the sample are also sketched as insets of the hysteresis loop shown in Figure 2-5.

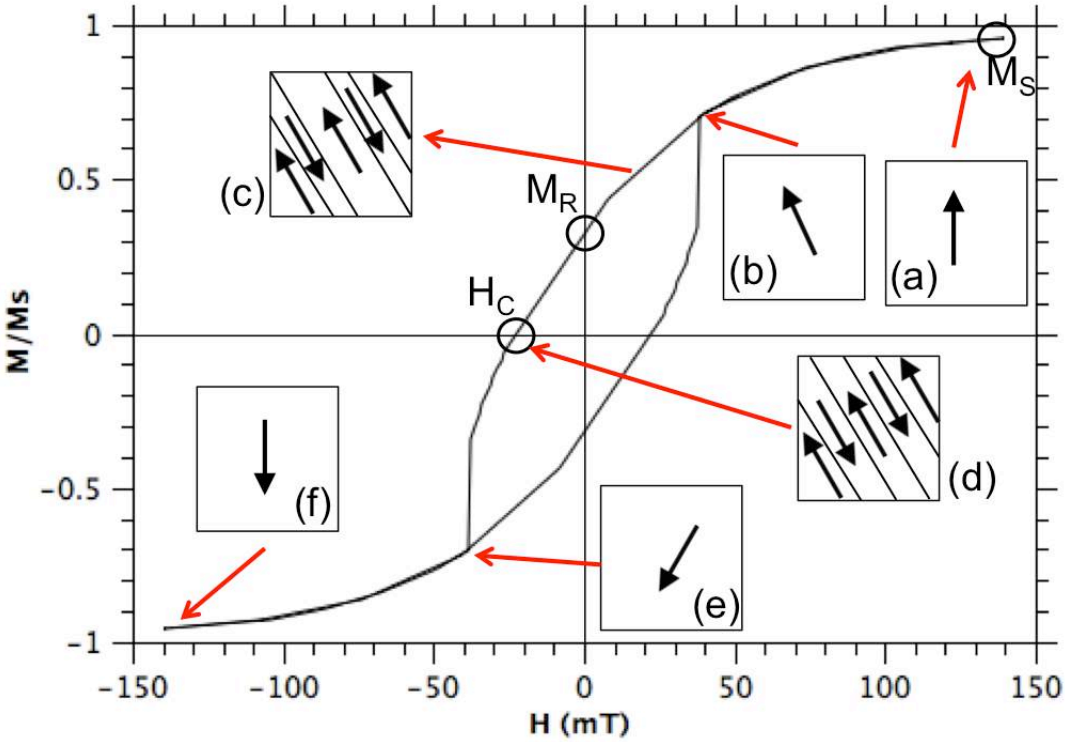

Figure 2-5: Hysteresis loop of a ferromagnetic material with insets of different domain configurations in a magnetization reversal process, and with the magnetization saturation, remanence and coercive fields marked in the loop.

There are three different magnitudes sketched in Figure 2-5; the magnetization saturation (M_S), that is characteristic of the material, and the remanent magnetization (M_R) and the coercive field (H_C), which characterize a hysteresis loop. The magnetization saturation has already been introduced previously. The remanent magnetization is the magnetization remaining in a ferromagnetic material after applying a large external field and then removing it. This quantity represents the fact that a ferromagnet can be spontaneously magnetized even in the absence of any external field. The coercive field is the field needed to bring the ferromagnet to zero magnetization.

2.5. References

[1] C. Kittel, *Rev.Mod.Phys*. **21**, 541-83 (1949)

[2] A. Hubert and R. Schäfer, *Magnetic Domains-the analysis of Magnetic Microstructures*, Springer Ed., Berlin (1998)

[3] A. Aharoni, *Introduction to the Theory of Ferromagnetism*, Oxford Science Publications, Clarendon Press (1996)

[4] W. F. Brown Jr., *Magnetostatic Principles in Ferromagnetism*, North-Holland Publishing Company, Amsterdam (1962)

[5] A. Aharoni, *J. Appl. Phys.* **83**, 3432 (1998)

[6] P. Weiss, *Comptes Rendus* **143**, 1136-1149 (1906)

[7] S. Blundell, *Magnetism in Condensed Matter,* Oxford Ed. (2001)

[8] D. J. Craik and R. S. Tebble, *Repts. Prog. Phys.* **24**, 116-66 (1961)

[9] R. Carey *et al.*, *Magnetic domains and techniques for their observation,* Academic Press, New York (1966)

[10] K. Onishi, H. Tonomura and Y. Sakurai, *J. Appl. Phys*. **50**, 7624-6 (1979)

[11] C. Schönenberger and S. F. Alvarado, *Z. Phys. B* **80**, 373-83 (1990)

[12] B. A. Lilley, *Phil. Mag.* **41**, 792 (1950)

[13] L. Néel, *C. R. Acad. Sci. París* **237**, 1468 (1953)

[14] R. D. McMichael and M. J. Donhaue, *IEEE Trans. Magn.* **33**, 4167 (1997)

[15] M. Kläui, *J. Phys.: Condens. Matter* **20**, 313001 (2008)

3. Nanofabrication

3.1. Introduction & tool description

The development of both fundamental and applied sciences is closely related to the potential observed in nanoscaled materials. Challenges such as synthesis, manipulation and characterization of new nanomaterials are the new frontiers of experimental science, whereas also theoretical physics has a key role in the development of this new science to assist knowledge advances with models and simulations. Also, theoretical models can be used to help technology producing new tools, or improving the already existing ones, as it is the case in [1], where a model describes the interaction between a measuring tool and the measured structure. Another big advantage that nanoscience brings to the scientific community is the possibility to integrate materials that are, in the macroscale, incompatible. The principles of physics, chemistry and biology change when going from the bulk to the nanometer scale, and it makes possible to integrate materials at the atomic and molecular levels, as is the case of nanobiotechnology. As an example, elongated nanotubes formed by carbon atoms (carbon nanotubes) with diameters on the order of 10 nanometers have been studied to help curing cancer [2], and scientists are studying the possibility substituting the carbon nanotubes by Tobacco Mosaic Viruses (TMV), which have the same shape and size than carbon nanotubes, that can be found in nature and are more biocompatible with human tissues [3].

There are two main methodologies in nanofabrication: the top-down approach, where a nanodevice is fabricated starting from a bulk material, manipulating and gradually removing or subtracting bits of the material to reach the nanoscale; and the bottom-up approach, consisting of manipulating and directly assembling nanoscale building blocks such as atomic or molecular elements. In both methods, sketched in Figure 3-1, a perfect control of the fabrication and environmental conditions is required, and for this reason many of the

nanotechnology fabrication methods are mostly operated with highly sophisticated equipment and under vacuum conditions in clean-room laboratories, which are laboratories where low levels of dust particles, acoustic and electromagnetic noises and vibrations are maintained, and are usually classified in terms of the maximum amount of dust particles that are present by squared meter [4]. Some examples of nanofabrication methods in the top-down approach are: photolithography, electron-beam lithography, ion-beam lithography, nano-imprint lithograpy, colloidal lithography and scanning-probe lithography. Some examples of bottom-up nanofabrication methods are: plasma arcing, chemical vapor deposition, molecular beam epitaxy, sol-gel synthesis and molecular self-assembly.

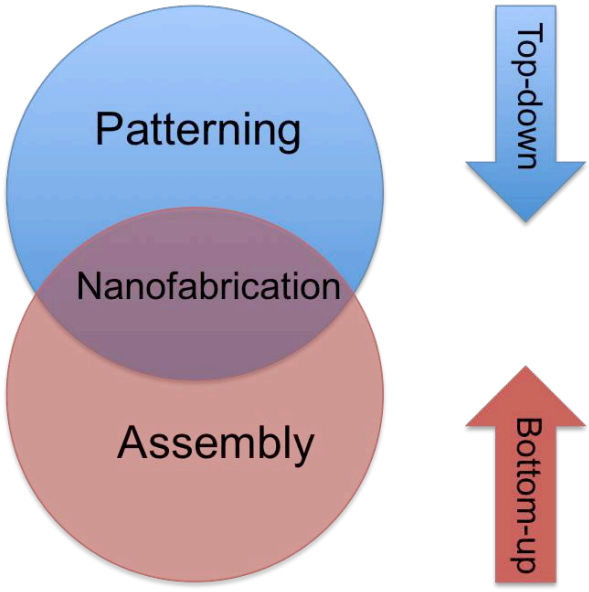

Figure 3-1: Description of the top-down and bottom-up approaches

It is precisely a combination of both top-down and bottom-up approaches what brings nanotechnology the most sophisticated nanostructures. As an example, a combination between electron-beam Lithography (top-down) and self-assembly of molecules (bottom-up) provides a nice platform for the study of single-molecule transistors [5]. As already mentioned, the top-down approach provides a good nanofabrication method to miniaturize bulk materials, and is basically composed by lithography techniques. Among all the different lithographic techniques, all of them share the same principle: transferring a pattern from one

media to another [6], each technique using a different transfer media. Photolithography is served by light as transfer media, and has a high yield that makes the technique ideal for semiconductors industry. Nano-imprint lithography uses a scaffold as transfer media, and scanning-probe lithography uses the microscope probe as transfer media. In the case of charged particles' beam lithography the beam is the transfer media, which irradiates a surface covered by a polymeric layer (resist) sensitive to the charged beam. In the case of electron-beam lithography the transfer media is a beam of electrons, responsible for the energy absorption by the polymeric chains in the resist when it is irradiated.

Yet in the 1960's the first evidence of a nanofabrication process involving an electron beam can be found [7], when the tools consisted of electron microscopes using a Gaussian beam to directly write the patterns on substrates without using any kind of mask, already with sub-micron resolution. These attempts were the first ones in which an electron microscope was modified to use Gaussian beams (converged at the maximum possible to get the smallest possible beam diameter), and the resolution was already below one micron. The electron-beam lithography process is, basically, composed of five steps: spin-coating of the polymer sensitive to the electron beam, exposure to the beam of the resist, developing of the resist, deposition of the material of which the patterned nanostructures will be made, and lift-off of the rest of resist and deposited material. A big amount of different parameters and conditions, which will be described in this chapter, are involved in the processing and their control and good adjustment is crucial for a good output of the process. Two of the main advantages of electron-beam lithography with respect to different lithographic techniques are its flexibility, as it does not use any mask, and its very high resolution, which is the main reason for being one of the widest used techniques for fabrication in nanoscience research [8].

The electron-beam lithography tool with which all the nanostructures studied in this thesis have been done is a Raith 150-two Electron-Beam Lithography (EBL) system, which can be observed in Figure 3-2. The main components of an EBL

are the ones also present in a scanning electron microscope (SEM), which are an electron source, the electron optical elements and the electromagnetic deflection unit, which are complemented with a pattern generator, the responsible of converting the software-designed patterns into electronic commands to move the electron beam over the resist. The design of the pattern to be fabricated can be done using CAD design software and imported with the Raith EBL software, directly designed with the Raith EBL software or even importing greyscale bitmaps into the Raith EBL software. Nevertheless, the final output of the nanostructure to be fabricated with the EBL system may differ from the input design given to the pattern generator, as there is a limiting resolution, which is in the range of 10 nm [9]. This resolution depends on the interaction of the electrons from the electron beam and the resist polymeric molecule, and on the post-exposure processing of the resist. Mainly, the resolution is determined by four different factors that are, namely, the delocalization between electrons and resist molecules during the exposure of the resist to the electron beam (due to the Coulomb interaction), the dispersion of secondary electrons in the polymeric resist, the scattered backward radiation due to the collisions of the electrons with the substrate and the molecular dynamics of the development process after the exposure. With this EBL tool it is also possible to reproduce a multilayer design in which two different materials are deposited, at different times after two different exposures, with predetermined contact points between the two materials. In this case, perfect mark recognition by the EBL software is required, so that the overlay occurs at the desired positions. Another characteristic of this EBL system is the proximity effect correction tool, which allows writing dense patterns with small gaps in between them. Electron scattering in neighboring exposure regions results in additional exposure events, and due to this some regions of the pattern would come out overexposed. With the proximity effect correction tool different adjacent parts of the design are assigned different electron dose values locally, so that in the parts where overexposure would occur less dose is assigned [10].

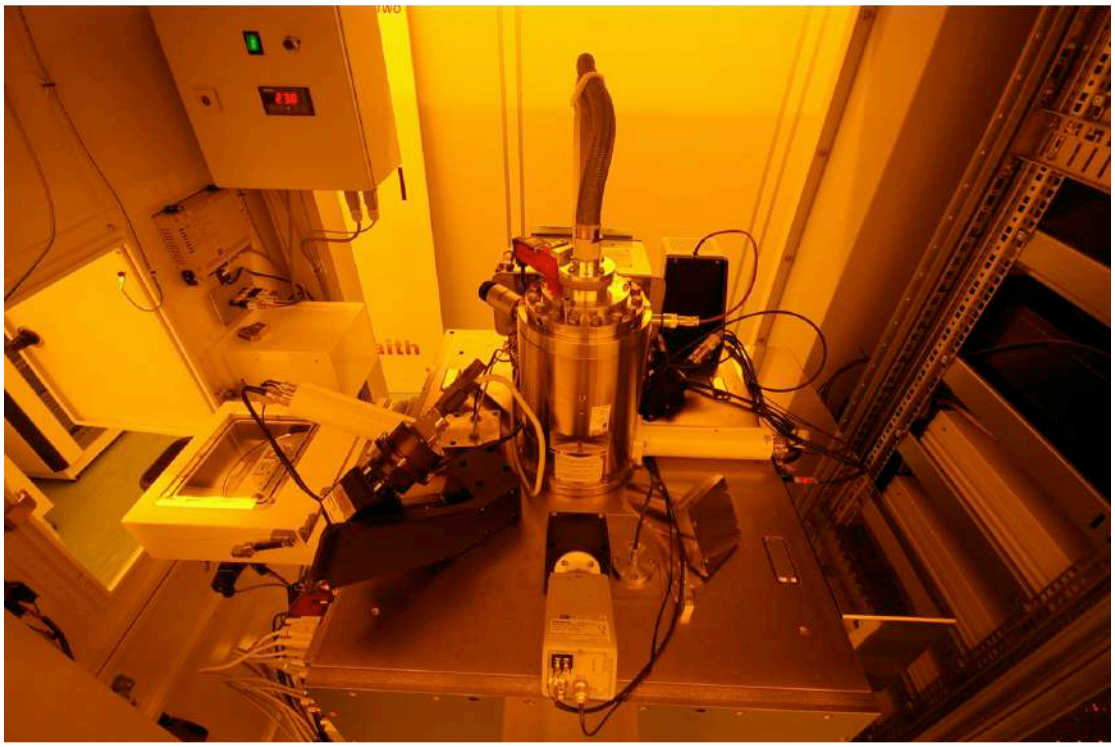

Figure 3-2: Raith 150-two Electron Beam Lithography tool present in the class-100 cleanroom at CIC nanoGUNE.

To finish with this introduction to the nanofabrication with an electron-beam lithography tool a collection of the main applications is described. In the semiconductor industry it serves as a good complement to photolithography, as it is used as mask fabrication for that technique. Also, this EBL technique is used for research and development of fundamental science applications [11], allowing researchers to fabricate nanoelectronic devices, patterned nanostructures, optically active nanomaterials, etc., making it suitable for research in a wide variety of disciplines.

3.2. Resists technology

A key issue in the electron beam lithography technique is an appropriate selection of the resist material involved in the process. The resist is a material sensitive to an electron beam (an EBL resist, not any kind of resist; e.g. a photoresist is sensitive to a certain wavelength light and not to electrons), which supports the recording of the latent image that will be transferred to the

substrate where the pattern will be fabricated. The electron beam modifies the resist composition of the exposed areas, and pattern features are materialized with the development process after the exposure. In an electron-beam lithography process many physical and chemical effects are involved, and a complete understanding of them is needed for an optimum performance.

There are many different types of resists sensitive to an electron beam, but one of the most common classification divides them into two groups, depending on their composition: inorganic and organic resists. The performance of each kind of resist varies depending mainly on one parameter, which is the energy of the electrons that modify the resists. In the case of inorganic resists, the highly energetic electrons are the ones that modify the resist during the exposure to the electron beam, whereas in the case of organic resist the lower energy (secondary) electrons are the ones that chemically modify the resist. This gives rise to the fact that inorganic resists have demonstrated a high-resolution performance and a low sensitivity. Nonetheless, the usage of inorganic resists presents additional difficulties concerning the subsequent nanofabrication steps, being this fact the one that limits their actual use [12].

The most widely used resists in electron beam lithography are the organic resists, and they can be further divided in positive or negative resist materials, whose behavior under exposure is sketched in Figure 3-3. The first ones, the positive resists, work by degradation of the exposed parts of the material due to the modification that secondary electrons coming from inelastic collisions cause on their chemical composition, provoking the break of the polymeric chains. The parts of the polymer exposed to the electron beam are more soluble than the rest of the polymeric chains, and they are removed when the resist is put in the developer after exposure, leaving the non-exposed parts of the resist still attached to the substrate, being the latter prepared for the deposition of the material of which the nanostructures will be made. Negative resists have a completely different behavior when exposed to the electron beam. In this case, the secondary electrons provoke a cross-linking of the polymer changes, causing a further solid-state polymerization of the negative resist. This causes, contrary

to what occurs with the positive resists, a decrease of the solubility of the areas exposed to the electron beam. Therefore, when the resist is sunk into the developer after exposure the non-exposed parts will be dissolved first than the exposed ones, leaving therefore the substrate with resist only on the exposed parts of the polymer.

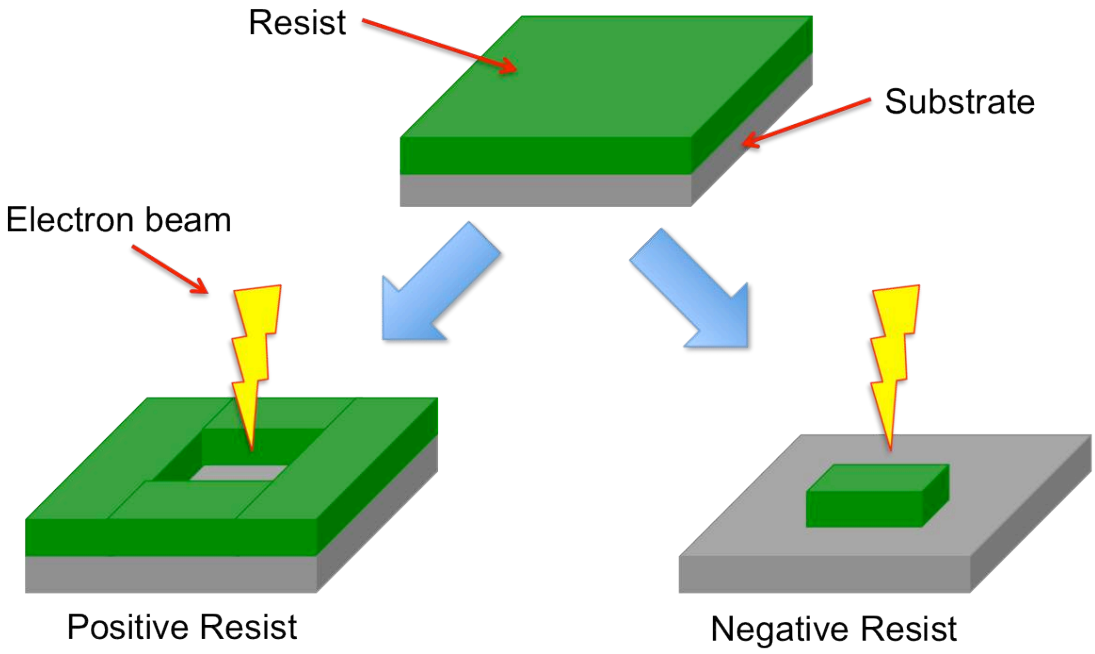

Figure 3-3: Effect of the electron irradiation on positive and negative resists

Before being able to fabricate nanostructures with the desired dimensions by EBL, one has to select an appropriate resist (positive or negative) and its thickness, depending on different parameters amongst which the most important one is the final thickness of the nanostructures to be fabricated. Once the optimum resist has been selected, the key parameter to be taken into account is the resist thickness, which should be desirably at least three times thicker than the nanostructure to be fabricated. This resist thickness is controlled by the spin-coating velocity of the resist on top of the surface of the substrate, which leads to different resist thicknesses depending on the molecular weight of the resist, the solvent on which it is dissolved (Anisole, Chlorobenzene, etc.), the resist-solvent proportion and the viscosity of the resist-solvent solution.

The nanostructures fabricated that are scope of study in this thesis have been made using organic positive resists, mainly PMMA (Poly-methyl methacrylate) based resists and its derivates. Indeed, already sub-10 nm patterning with PMMA has been reported [13,14]. Besides using PMMA-based resists, also LOR (PGMI,poly-methyl glutarimide-based) resists have been used. Both kind of resists and their behavior will now be described in more detail.

3.2.1. PMMA-based resists

The first attempts of direct EBL writing with a polymeric resist were performed with PMMA, and nowadays it continues being the most used. Apart from being used in EBL writing, it is used as resist for photolithography with X-rays and deep UV radiation. It has a high resolution that permits defining small nanostructures on the limit of the actual resolution of the technique (i.e. around 10 nm), and the slow dissolution rate in the developer (which is methyl isobutyl ketone, MIBK, usually mixed with isopropanol, IPA, on a 1:3 ratio) allows a better control of the developing process. The different types of commercialized PMMA resists are classified depending on the solvent (as previously mentioned, chlorobenzene or anisole), the proportion of PMMA in the solvent and the average weight of the molecular chains. So far, 950K (kiloDalton) and 495K molecular weight PMMA resists are the most used, being the final resolution higher with higher molecular weights, due to the smaller size of the chain scission products in higher molecular weight polymers.

The nanostructures made for the experiments described in this thesis have been fabricated using two different PMMA-based resists: 950K PMMA A2 (PMMA with 950kDa molecular weight dissolved in anisole at 2%) and 495K PMMA A2 (PMMA with 495kDa molecular weight dissolved in anisole at 2%).

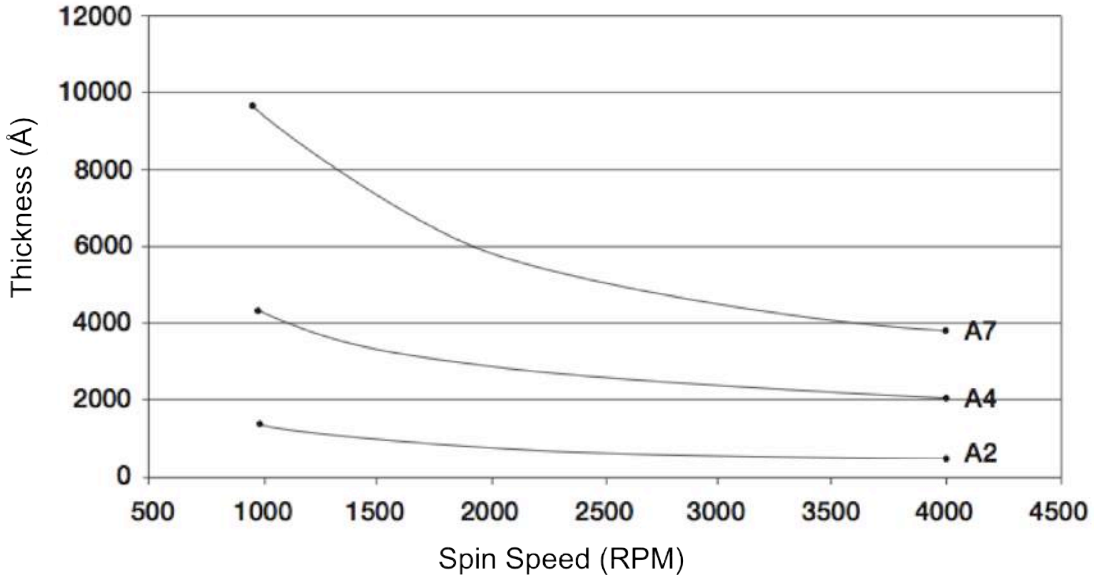

Figure 3-4: Spin speed Vs Thickness curves for 950K PMMA resist spin coating. 'AX' at the end of each curve stands for the percentage of PMMA dissolved in Anisole.

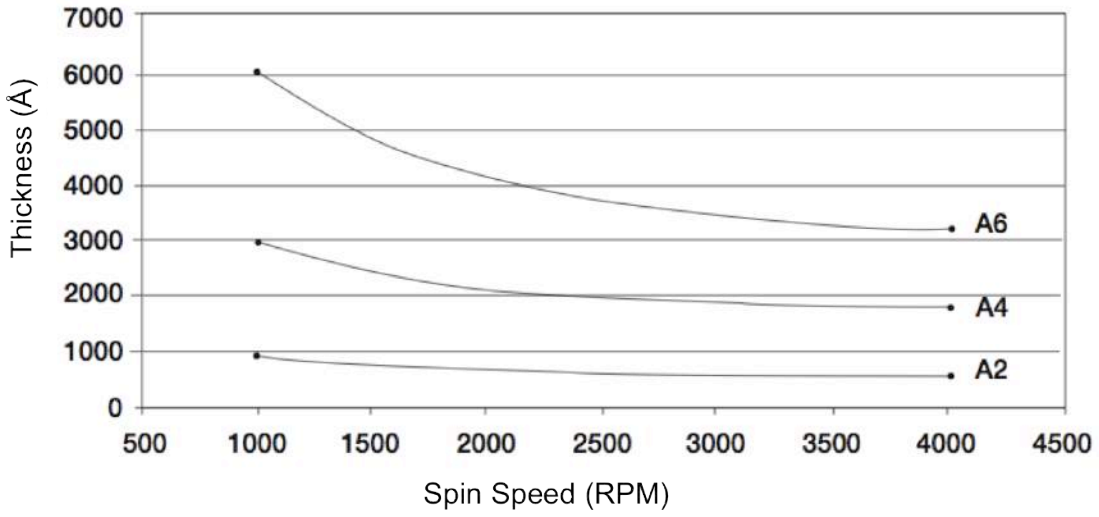

Figure 3-5: Spin speed Vs Thickness curves for 495K PMMA resist spin coating. 'AX' at the end of each curve stands for the percentage of PMMA dissolved in Anisole.

The spin-coating curves observed in Figure 3-4 andFigure 3-5 vary depending on the environment and equipment being used, and are used as a guide to the eye

for the spin-coating of the PMMA resists on the substrate, explained in section 3.2.3, before the electron exposure.

3.2.2. LOR resists

The LOR resists are lift-off PMGI-based resists that are used in combination with conventional positive resists for multiple-layer resist processes. They are used as bottom layer in a bilayer (or multilayer) resist exposure process where the upper layer is sensitive to the electron beam, and their function is usually to produce a good undercut profile between the top layer and the substrate for a better lift-off processing. They are designed for applications requiring high-resolution imaging, easy process tuning, high yields and superior deposition line width control. Some of the main applications using LOR or PGMI-based resists include Giant MagnetoResistance (GMR) and MagnetoResistance (MR) heads, wireless devices and opto-electronic devices.

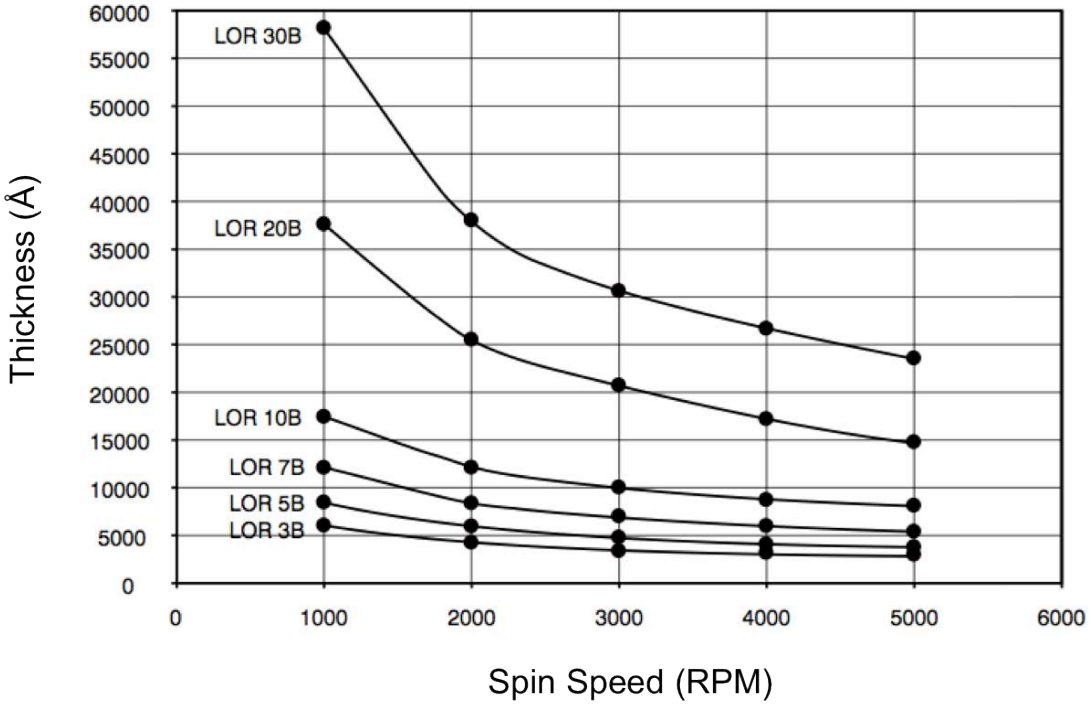

Figure 3-6: Spin speed Vs Thickness curves for LOR B resist spin coating. 'XB' at the end of each curve stands for the percentage of LOR dissolved in the solvent.

One of the best advances that LOR resists provide with respect to the usage of a PMMA-based resist as underlayer to get an undercut profile on the resists is that their dissolution rate is optimized for a maximum undercut control. As in the case of PMMA, there are also different LOR resists: LOR-A series and LOR-B series, with different dissolution rates, which allows to select one of the other depending on the processing and the undercut profile characteristics needed. The spin-coating curves for LOR resists are shown in Figure 3-6.

3.2.3. Spin-coating recipes

As previously stated, the thickness of the resist layer to be exposed to the electron beam is a key parameter in this nanolithography process. Before coating the substrate where the nanostructures will be fabricated, it has to be cleaned so that the resist layer is the most uniform possible. EBL has been reported to be used with different substrates, including insulating (i.e. glass) substrates to study plasmonics [15, 16] or semiconducting (i.e. silicon) substrates to study the magnetic properties of nanoelements [17]. The first action to perform is to cut the substrate into pieces of $1cm^2$ (or the desired dimensions), where the resist will be spin-coated. In order to clean the substrate a recipe involving different solvents has been used. This recipe consists of performing series of ultrasonic bathes in organic and inorganic solvents, followed by a plasma asher treatment (to remove any remaining organic molecule on top of the substrate), and consists of:

- 10 minutes ultrasonic bath on TCE (trichloroethylene).
- 10 minutes ultrasonic bath on acetone.
- 10 minutes ultrasonic bath on IPA (isopropanol).
- 3 minutes plasma asher treatment, in Ar and O atmospheres at 100W power.

After cleaning the substrate it is ready to spin-coat the resist. Different combination of resists have been used for the optimization of the

nanofabrication process, with the aim of fabricating reproducibly small nanostructures with sizes on the order of sub-100nm dimensions with gaps between them below the 30nm size. The first recipe used consists of a single layer of 950K PMMA A2 resist, which is spin-coated at a speed of 2000rpm for 60 seconds, followed by a post-bake of the resist at 195^0 C for one minute. The final thickness of the resist is around 100nm, being the nanostructures fabricated with this recipe not thicker than 25nm. Then, the spin-coated resist is exposed to the electron beam and developed afterwards, and the lithography process is completed with the deposition of the material and the lift-off, as sketched in Figure 3-7.

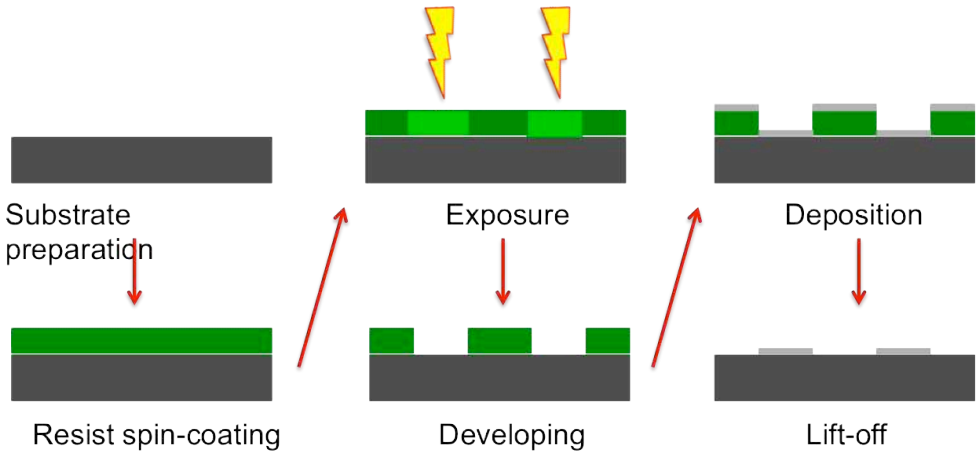

Figure 3-7: Single-layer resist Electron Beam Lithography process.

The final nanofabrication results obtained with this recipe (and with all the recipes described in this section) will be discussed at the end of this chapter, after the rest of the lithographic steps have been discussed. This is the only single-layer spin-coating recipe that has been used for the nanofabrication of structures in this thesis, but bi-layer resist recipes have also been implemented. One of them is a recipe involving two PMMA-based resists, where the underlayer resist is 495K PMMA A2, and the overlayer resist is 950K PMMA A2. The objective of this double-layer resist is to obtain an undercut profile between the two resist layers, which allows to have a deposition of the metals in which the edges of the nanostructures to be fabricated are not in contact with the resist walls, contrary to what happens in the case of a single-layer resist procedure.

The difference in molecular weights of the 495K and 950K PMMA resists provokes a slight difference in the dissolution rates at the developing stage, giving rise to the appearance of an undercut profile in the bi-layer resist profile, as sketched in Figure 3-8. Firstly, a 495K PMMA A2 resist layer is spin-coated on top of the substrate at a speed of 4000rpm for 60 seconds, followed by a post-bake of the resist layer at 195^0 C for 60 seconds. Afterwards, a 950K PMMA A2 resist layer is spin-coated on top of the previously spin-coated resist layer, at a speedo of 4000rpm for 60 seconds, followed by another post-bake of this resist layer at 195^0 C for 60 seconds. The total thickness of the two resists is on the order of 110nm.

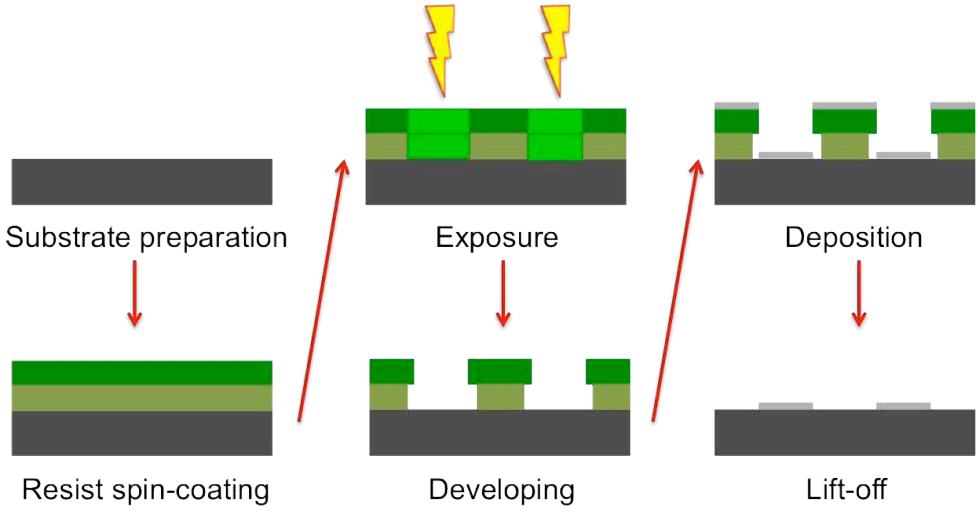

Figure 3-8: Double-layer 495K A2 & 950K A2 PMMA resist Electron Beam Lithography process.

Apart from these two PMMA-based resist processes, a third process involving both PMMA and LOR resists. This third and last resist spin-coating procedure is the one that has given the best performance for the nanofabrication of our structures. In this case, the double-layer process involves a bottom layer of LOR 01B resist and a top layer of 950K PMMA A2 resist. The main advantage of this process is that, as the two resists are based on different polymers, at the developing stage two different chemicals are used to develop each layer separately, which permits to have a much better control on the undercut profile, as two different developing times can be implemented in the whole process. The bottom layer of LOR 01B resist is spin-coated at a speed of 4000rpm for 60

seconds, followed by a post-bake at 225^0 C for 15 minutes. Afterwards, the top layer of 950K PMMA A2 resist is spin-coated at a speed of 4000rpm for 60 seconds, followed by a post-bake at 195^0 C for 1 minute. In this case the bottom layer of LOR 01B is much thicker than the one of 495K PMMA A2 used in the previous recipe, and is on the order of 300nm, whereas the 950K PMMA A2 layer is on the order of 60nm. A sketch of the double-layer resist procedure involving PMMA and LOR resists can be observed in Figure 3-9.

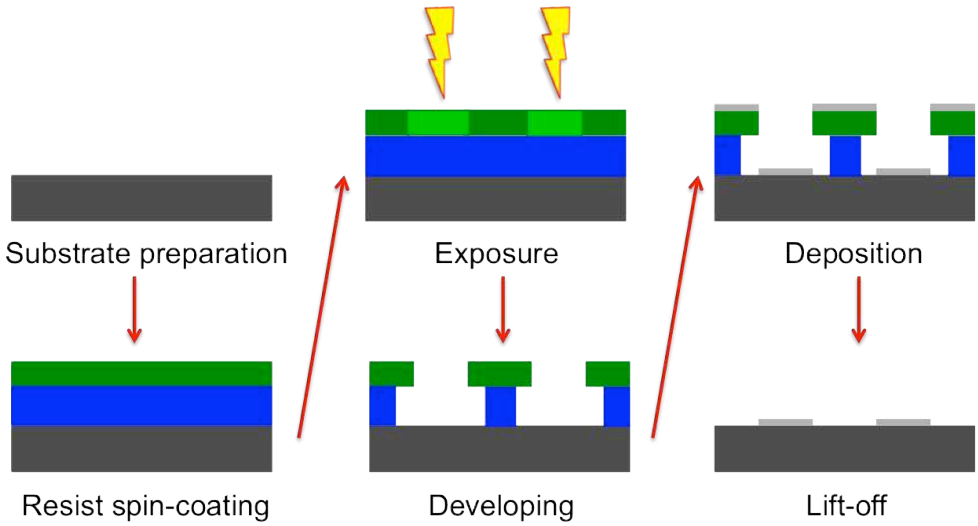

Figure 3-9: Double-layer LOR 01B & 950K A2 PMMA resist Electron Beam Lithography process.

The different results obtained with the three recipes described here will be discussed at the end of this chapter, as the final shape of the nanostructures is determined by a good adjustment of all the parameters involving the whole nanofabrication process.

3.3. Exposure

The physical phenomenon that leads to the chemical modification of the resist layer is the exposure of the resist to the electron beam. Therefore, understanding how the electron beam affects the properties of the polymeric resist is necessary in order to have a complete understanding of the whole electron-beam lithography process. As previously stated, the exposure of the resist to the

electron beam results into either cutting the main polymer chains (positive resist) or cross-linking of the polymers (negative resist). This process occurs because of the dissipation of energy in the range of 5eV from scattered electrons (secondary electrons) by the incident electron beam. In order to simulate the effect of an incident electron beam on the polymer chains the total energy dissipated in scattering events of secondary electrons is calculated, due to the fact that the energy losses in the resist upon exposure are accumulated as the amount of chemical changes. This simulation of the energy dissipation in the scattering events is performed using Monte Carlo calculations. Many models have been proposed to calculate the energy deposited in a material by electron scattering events, but the most widely used one in the case of elastic scattering is the theory of Rutherford scattering, whereas in the case of inelastic scattering it is the Bethe-Bloch formulation [18]. The simulation described here follows all the incoming and secondary electrons until they have small enough energies to provoke scattering events that modify the properties of the polymers.

Partial wave expansion is used to simulate the elastic scattering events, using plane waves connected to the wave function around the atomic potential, being the differential scattering cross-section given by:

$$\frac{d\sigma_m}{d\Omega} = |f_k(\theta)|^2 \qquad (3\text{-}1)$$

$$f_k(\theta) = \frac{1}{k}\sum_l (2l+1) exp(i\delta_l) sin\delta_l P_l(cos) \qquad (3\text{-}2)$$

being σ_m the cross-section of elastic scattering for the m-th atom, Ω the scattering solid angle, $f_k(\theta)$ the scattering amplitude, k the wave number of the incident electron, θ the scattering angle, δ_l the phase shift of the l-th partial wave and $P_l(cos\theta)$ the Legendre function. The phase shift is derived from solving the Schrödinger equation for the wave function with angular momentum $\hbar\sqrt{l(l+1)}$, as described in [19]. By integrating Eq.(3-1) the total scattering cross-section σ_m and the main free path Λ are derived:

$$\sigma_m = \int \frac{d\sigma_m}{d\Omega} d\Omega = \frac{4\pi}{k^2} \sum_l (2l+1) sin^2 \delta_l \quad (3\text{-}3)$$

$$\Lambda = 1/\sum_m N_m \, \sigma_m \quad (3\text{-}4)$$

where N_m is the amount of atoms m per unit volume, and the scattering angle θ is derived from the scattering cross-section (Eq.(3-1)) and uniform random numbers. In the case of inelastic scattering processes, the formula used in the simulation is the one derived by Gryzinski. With it one can derive the differential scattering cross-sections for the electron excitations [20]:

$$\frac{d\sigma_{mi}}{d\Delta \mathrm{E}} = n_{mi} \frac{\pi e^4}{\Delta E^3} \frac{E_{mi}}{E} \left(\frac{E}{E+E_{mi}}\right)^{3/2} \left(1 - \frac{\Delta E}{E}\right)^{E_{mi}/(E_{mi}+E)} \times \left\{ \frac{\Delta E}{E_{mi}} \left(1 - \frac{\Delta E}{E}\right) + \frac{4}{3} ln \left[2.7 + \left(\frac{E-\Delta E}{E_{mi}}\right)^{1/2} \right] \right\} \quad (3\text{-}5)$$

being σ_{mi} the inelastic scattering cross-section, n_{mi} the number of electrons in the i-th orbital of atom m, ΔE the dissipated energy, E_{mi} the average energy of electrons in the i-th orbital of atom m and E the energy of the incident electrons. Again, by integrating this equation the scattering cross-section and mean free paths are derived:

$$\sigma_{mi} = \int_{E_{mi}}^{E} \frac{d\sigma_{mi}}{d\Delta \mathrm{E}} d\Delta \mathrm{E} \quad (3\text{-}6)$$

$$\Lambda = 1/\sum_m (N_m \sum_i \sigma_{mi}) \quad (3\text{-}7)$$

From Eq.(3-6), the dissipated energy $E_1$is calculated by using a uniform random number R (from 0 to 1) from the formula:

$$R = \frac{1}{\sigma_{mi}} \int_{E_{mi}}^{E_1} \frac{d\sigma_{mi}}{d\Delta \mathrm{E}} d\Delta \mathrm{E} \quad (3\text{-}8)$$

A more detailed derivation of the equations written here for the Monte Carlo simulations of the energy losses in scattering events, responsible for the physical

changes on the polymers forming the resist, can be found in [18] and [19]. With the implementation of these equations, Monte Carlo simulations of the trajectories of the electrons with two different accelerating voltages for the electron beams have been performed, on a system composed by a PMMA layer 350nm thick on top of a Si substrate, which can be observed in Figure 3-10, taken from [21].

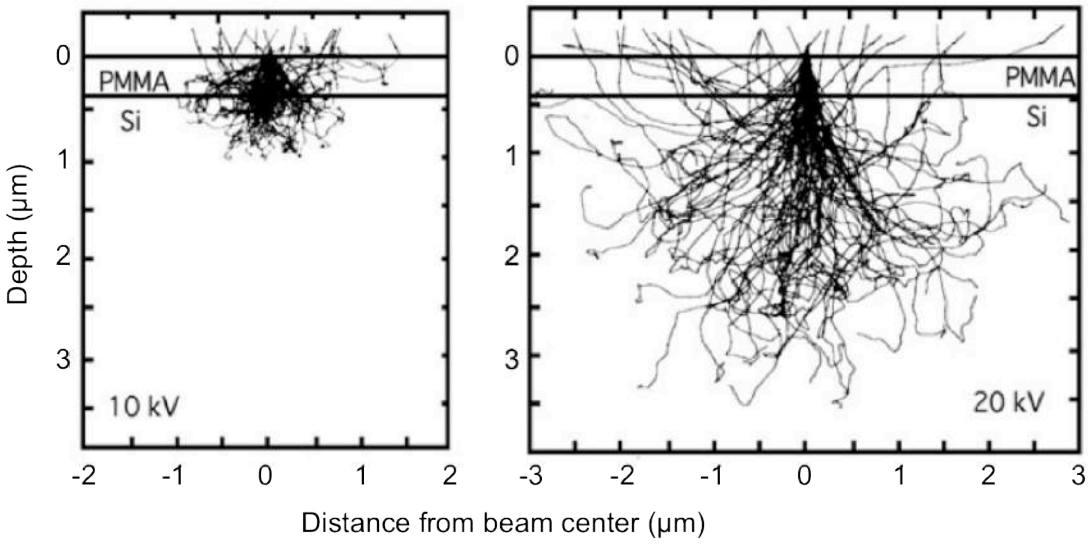

Figure 3-10: Monte Carlo simulations of electron scattering in a system composed by a 350nm thick PMMA layer and a Si substrate, from an incoming electron beam with acceleration voltage 10 kV (left) and 20 kV (right) [21].

The results show how the secondary (scattered) electrons penetrate on the resist and the substrate, with a big increase, in the 20 kV accelerating voltage case, of the backscattered electrons responsible for the proximity effect that causes a bigger exposure of electrons than what is desired in neighboring nanostructures.

The energy of the electrons that penetrate the resist and, therefore, suffer the scattering events cascade is determined by different parameters, being the main one the accelerating voltage of the electron beam. Therefore, a good adjustment of all the parameters involving the lithography process, together with an appropriate selection of the resist to be used, determine the final resolution of

the nanostructures. The main parameters to be adjusted prior to the exposure of the resist are listed and defined hereafter:

- Accelerating voltage: The voltage to which the electrons are accelerated before they exit the electron gun. It affects the electron scattering into the resist, and defines the wavelength of the electrons that hit the resist. The bigger the voltage, the more scattering events and backscattered electrons provoking proximity effect.

- Working distance: distance between the resist surface and the gun exit aperture. Shorter working distance produces a smaller beam size, whereas larger working distance lead to larger exposure areas. This parameter is the one responsible of the focusing (changing the working distance means changing the focusing). A bad setting of this parameter provokes image blurring.

- Aperture size: last variable diaphragm that is crossed by the electrons before escaping the gun. This parameter is very important for the lithographic work. Smaller aperture gives smaller beam size (diameter), better resolution, less aberrations and increased depth of field, which is good for high-precision work. But it also reduces probe current and signal to noise ratio. These effects make more demanding the electron beam focusing (space charge effects) and alignment. Larger aperture results in higher electron beam current and signal to noise ratio, reduced resolution and depth of field. This makes it possible the use of shorter dwell times and/or larger step size during the exposure, parameters explained later on this parameter list.

- Aperture angle: this parameter is defined by the aperture size and the working distance. The final resolution of the writing process depends on the aperture angle and the accelerating voltage in the following way:

$$d = \frac{\lambda}{a} \qquad (3\text{-}9)$$

where d is the minimum resolved distance when writing, λ is the wavelength of the electrons hitting the resist and a is the aperture angle.

- Aperture alignment: it corrects the position of the aperture to avoid beam shifting while moving the electron beam over the resist in the writing process.

- Stigmation: this parameter corrects the asymmetries present in electron lenses. A bad setting of the stigmation provokes distortion on the nanostructures that are being written.

- Write field size: it defines the area of the resist that can be reached by the electron gun without moving the column, using only the beam deflection (electromagnets).

- Beam current: this is the electron current reaching the sample for the particular aperture and high voltage selected.

- Area dose: the minimum dose required to fully develop an area of the resist, i.e. fully remove resist during the development step.

- Dwell time: the time the beam stays at each location to expose a single dot.

- Step size: the length of the beam displacement during each dwell time. Usually 5 - 15nm for WF size of 60 - 100μm and 100 - 200nm for WF size of 800 - 1500μm (i.e. bonding pads).

These last four parameters are interdependent: the current, together with the step-size, resist sensitivity and dwell time, are the factors determining the dose

of electrons, viz., the total charge per unit area, to which the resist is exposed, being the formula relating them the following one:

$$Area\ Dose = \frac{Dwell\ Time \times Current}{Step\ Size^2} \tag{3-10}$$

When writing any nanostructure by electron-beam lithography, a first selection of the accelerating voltage, the working distance, the aperture size and the write field has to be made, depending on the characteristics and dimensions of the nanostructure to be written (e.g. for small nanostructures with small gaps between them, a relatively low accelerating voltage to avoid proximity effect is needed, and also small aperture size, working distance and write field to increase resolution). Once a first selection of these parameters has been performed, an adjustment of the writing parameters (i.e. area dose, step size, dwell time) is needed. For this purpose an array of test nanostructures with different area doses and/or step sizes and dwell times is written, and after finishing the whole lithographic process the test sample is checked. The good parameters are selected from the structures with the correct sizes and shapes.

3.4. Post-exposure processing: developing

The developing step is the one in which the parts of the resist that have been exposed (positive resist) or not exposed (negative resist) to the electron beam under the correct exposure parameters are removed. During this step the latent pattern (bright parts of the resist in Figure 3-6, Figure 3-7 and Figure 3-8) is converted into a physical resist profile, leaving the desired portions of the substrate uncovered, without resist, ready for the material deposition. The developing is based on the differences on the solubility of the polymer resist sorted when the polymer has been exposed to the electron beam and when it has not been exposed. In the case of positive resists, the parts of the polymer that have been exposed to the electrons have smaller molecular weights and, therefore, are isotropically dissolved in the developer faster than the non-exposed ones, whereas in the case of negative resist the cross-linking of the

polymer chains of the resist resulting from the exposure to the electron beam causes these exposed zones to have a higher molecular weight than the non-exposed ones, which are isotropically dissolved faster on the developer.

It is usual to combine two resists with different molecular weights to provoke an enhanced undercut profile in the resist profile after the developing stage, as observed in Figure 3-8 and Figure 3-9. The simplest bi-layer resist process is the one involving two PMMA resists, where the top resist has a higher molecular weight than the lower one [22]. The low molecular weight PMMA layer is more sensitive than the high molecular weight PMMA, and therefore the resist is developed with an enhanced undercut profile. In our case, two double layer resist processes have been implemented; one with a 950K PMMA A2 resist layer spin-coated on top of a 495K PMMA A2 resist layer, which yields an undercut profile that can be observed in Figure 3-11 after developing, and a second one involving a 950K PMMA A2 resist layer spin-coated on top of a LOR 01B resist layer. The main advantage of this second bi-layer protocol with respect to the first one is that the undercut profile can be controlled in the developing stage, as the two resists have different developers and the developing time of each resist layer can be controlled separately.

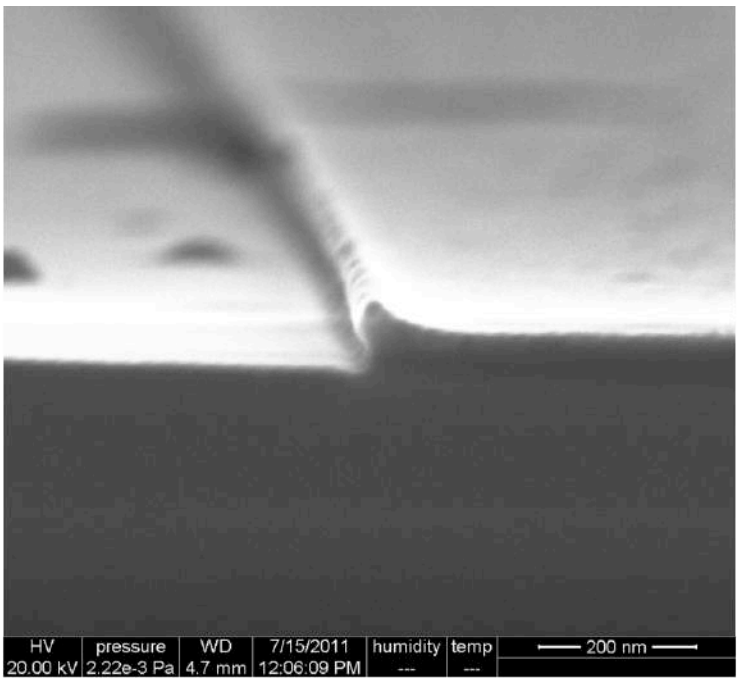

Figure 3-11: undercut profile in a double 495K and 950K PMMA A2 bi-layer resist process.

The developer is chosen depending on the polymer material composing the resist. In the case of PMMA-based resist, the developer used is a solution of Methyl-Isobutyl Ketone (MIBK) and Isopropanol (IPA) in the proportion 1:3, and the stopper to the developing is IPA without MIBK. The developing times used in our processes involving a single layer or a multilayer with PMMA-based resists was 40s in MIBK:IPA (1:3) plus 20s in the stopper, IPA. In the case of LOR resists the developer is ma-D 525, which is the commercial name for a solution of tetramethylammonium hydroxide in water, and the stopper is distillated water. In the processes involving the usage of a LOR 01B underlayer resist in a double layer resist process, the developing of the LOR 01B layer is performed after the top PMMA layer has been developed, so that the LOR 01B layer is in contact with its developer only in the parts where the PMMA has been removed. Therefore, the developing time for the LOR 01B layer is critical to obtain the desired undercut profile. If it is too low, the undercut profile will almost not be present, and if it is too big, the top PMMA layer will fall into the hole left by the dissolved LOR 01B. Our recipe uses a developing time of 7-8s in ma-D 525 followed by 10s in distillated water to stop the developing.

3.5. Deposition

After developing the resist, the next step in the nanofabrication process is the deposition of the material of which the nanostructures will be made, as observed in Figure 3-7, Figure 3-8 and Figure 3-9. Two different deposition techniques have been used to fabricate the nanostructures studied in this thesis: the sputter deposition technique and the electron beam evaporation technique. Both of them will be described in this section.

3.5.1. Sputter deposition technique

The ultra-high vacuum sputter deposition technique is nowadays a well-established technique to deposit high quality metallic thin films. The sputtering

technique is basically an ion-bombarding process aiming to deposit atoms of the bombarded material onto the substrate. The simplest sputtering configuration consists of a diode formed by two electrodes in a chamber filled with a low-pressure gas. The target made of the material to be deposited in the substrate is set in the cathode, and a big DC potential is applied between the electrodes, therefore generating an electric discharge that ionizes the gas present in the chamber, forming in this way the plasma that fills the sputtering chamber. The ions present in the plasma are accelerated towards the cathode, and when they hit the target the ion transfers energy to the target atoms. When multiple scattering events transfer enough energy to a target atom, it abandons the surface of the target and travels towards the substrate where it will get attached. When the plasma ions hit the target, apart from the target erosion different effects also occur, such as secondary ions emission, radiation emission and secondary electrons emission, all of them contributing to increase the ionization of the plasma, and therefore the ion bombarding of the target increases, finally increasing the process efficiency.

The thickness of the material deposited on the substrate is controlled by a quartz crystal balance, which is the thickness monitor of the sputter system. This thickness monitor detects the changes in the frequencies of the normal modes of the quartz crystal layer depending on the amount of mass of the material hitting it. Prior to a well-controlled deposition, a calibration of the deposition rate for a certain material has to be performed. The deposition rate is calculated by depositing a thin layer of the desired material on a quartz crystal for fixed values of the power, current and pressure of the plasma and, after this calibration, the obtained deposition rate is used to deposit in a controlled way layers of this material (always with fixed power, current and pressure). There are two sputtering deposition modes: non-reactive and reactive sputtering processes, depending on the gas from which the plasma is created. In the non-reactive sputtering processes the gas forming the plasma is usually Argon, with which high yields are obtained. In the reactive sputter deposition the sputtering process takes place in the presence of a reactive gas, usually Oxygen.

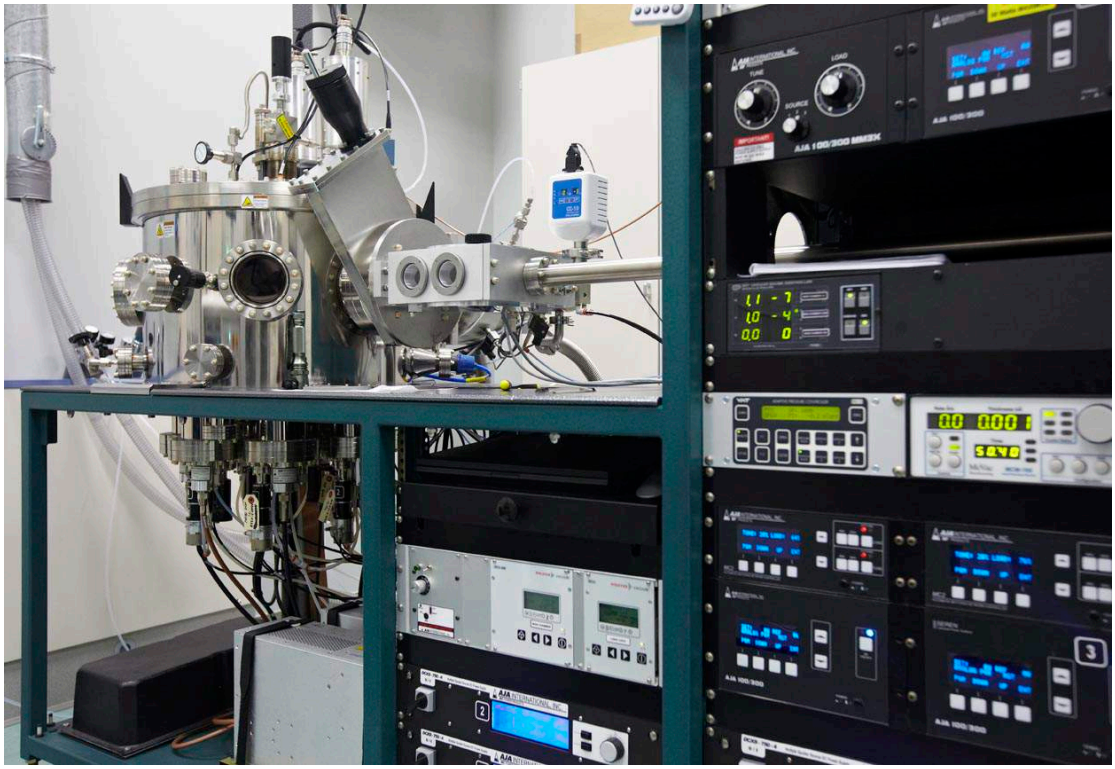

Figure 3-12: 7-gun AJA Sputtering System present at the nanomag lab in CIC nanoGUNE.

The sputter tool used to nanofabricate some of the structures studied in this thesis, which can be observed in Figure 3-12, is a 7-gun AJA Sputtering System, which allows for the deposition of up to seven different materials (5 of the guns are DC guns, and 2 of them are RF guns, for reactive sputtering) on the same substrate without breaking the vacuum conditions in the chamber. It also allows the user to perform co-sputter of different materials at the same time, which is a requirement to deposit metallic alloys.

3.5.2. Electron-beam evaporation technique

This technique is based on the heat produced by bombarding a high-energy electron beam over the material to be deposited on the substrate. The electron beam is generated by thermionic emission of electrons produced from an incandescent tungsten filament, and the emitted electrons are accelerated towards the crucible containing the material to be deposited with a high voltage on the order of 10 kV. A magnetic field is used to curve, direct and focalize the electron beam trajectory, allowing controlling the position where the electron

beam is hitting the target and the size of the region being hit by the electrons. Due to the possibility of focalizing the electron beam onto a very small region of the material that is evaporated it is possible to obtain a localized heating point with a high evaporation power density, which permits a good control over the deposition rate, ranging from low (0.1 Å/s) to high values (1 nm/s) and, even more important, allows the evaporation of metals with high fusion temperature (e.g. W, Ta, etc.). The system is operated under high vacuum conditions, to avoid contamination of the metallic film that is being deposited, and also to increase the mean free path of the particles travelling towards the substrate (i.e. under a vacuum atmosphere of 10^{-4} Pa a small particle below the nm size has a mean free path of around 60 m.). When the vacuum is low or poor, the presence of oxygen particles on the chamber oxidizes the metal that is being deposited, and the metal surface appears to be non-uniform. The system is water-cooled to avoid overheating of the system.

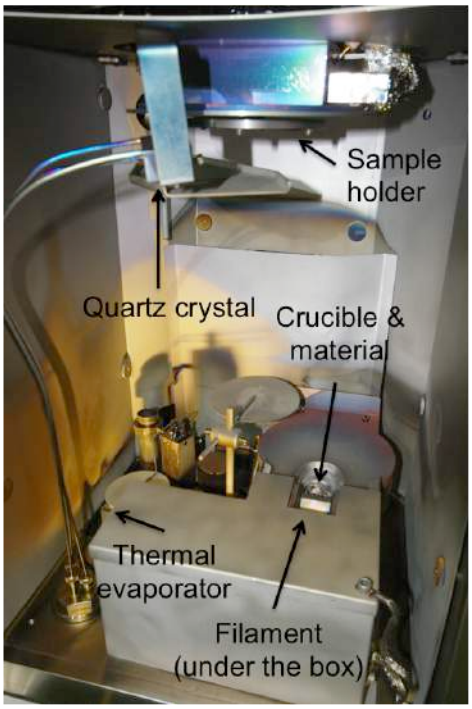

Figure 3-13: Oerlikon Univex 350 electron-beam and thermal evaporation system present at the clanroom in CIC nanoGUNE.

The electron-beam evaporation system used to nanofabricate many of the structures scope of study in this thesis is an Oerlikon Univex 350 electron-beam and thermal evaporation system, shown in Figure 3-13, which is located in the

cleanroom facilities of CIC nanoGUNE. It is equipped with eight pockets, allowing deposition multilayers from eight different materials without breaking the vacuum conditions.

There are many differences between the two deposition techniques used to fabricate the nanostructures for this thesis. One of them has to do with the energy of the atoms/ions hitting the substrate/resist of the nanopatterned surface after the developing step: in the case of a sputter deposition this energy is higher than in the case of an electron-beam evaporation deposition. This is an advantage to the sputter deposition in the sense that the adhesion to the substrate is stronger, but also a risk when using a multilayer resist system because the top layer forming the undercut profile might be destroyed. Therefore, when using multilayer resist profiles using sputter deposition is risky for the undercut profile. Another difference between the two deposition techniques is the directionality of the deposition; whereas in the case of the sputtering the deposition is isotropic or with a very little preference on the directionality of the deposition, with the electron-beam evaporation the evaporated atoms follow straight paths, being the deposition completely directional. And finally, another important difference between the two deposition methods described in this chapter is strictly related to the final composition of sputtered or deposited alloys. In the case of the sputter deposition the stoichiometry of the alloy is conserved, as all the components of the alloy are sputtered with the same rate, whereas in the case of the electron-beam evaporation deposition this does not necessarily happen, due to the differences on the components' evaporation rates.

3.6. Lift-off

The lift-off is the last step of the electron-beam lithography nanofabrication process. In this step the remaining resist on top of the substrate (with a layer of the deposited material on the previous step on top) is removed, by chemical etching of the polymeric materials submerged on different solvents. Depending

on the strength of the adhesion of the polymeric resist to the substrate, different chemical solvents are used in the lift-off process. In the case where the bottom (or unique) layer is a PMMA-based resist a combination of acetone, methylene-chloride:acetone (8:1) and isopropanol (IPA) solvents is used for lifting-off the resist, whereas with a PGMI-based resist (LOR) as a bottom layer the lift-off is heat-assisted and the chemical m-rem 660 (N-methyl pyrrodyne based) is mainly used, helped by acetone and IPA. Ultrasonic bathes of different durations also help to detach the remaining resist stuck to the nanostructures that have been written.

More in detail, the lift-off procedure followed in the case of a PMMA-based bottom resist process is: two hours in CH_2Cl_2:Acetone (8:1), followed by a 10 seconds ultrasonic bath in the same solvent, and another 10 seconds ultrasonic bath in isopropanol. This process is the final result of different combinations of solvents and ultrasonic bathes used for lift-off. The first protocol used consisted of a simple submersion of the sample on acetone for two hours, but there was a huge amount of resist attached to the nanostructures. Therefore, ultrasonic baths of different amount of times were performed, combined with IPA rinses and ultrasonic bathes, until the lift-off was optimized with the recipe presented before.

A different lift-off procedure is followed when the bottom layer is PMGI-based (LOR resist). In this case, the sample is submerged in mr-rem 660, which is a solvent based on N-methyl-2-pyrrodyne, for one hour at 100^0C, followed by an ultrasonic bath in this solvent for 5 seconds, another ultrasonic bath in acetone for 5 seconds and a last ultrasonic bath in isopropanol for 5 seconds. The results of the whole nanofabrication process following the different recipes (different resists, exposure parameters, lift-off procedures, etc.) will be discussed hereafter.

3.7. Nanofabrication results: discussion

In the last section of this nanofabrication chapter the different recipes and the results obtained with them will be discussed. Three different recipes, each of them involving different resists, have been optimized in order to improve the performance of the nanofabrication process and the characteristics of the resulting nanostructures. The first recipe used a single layer resist of 950K PMMA A2, as sketched in Figure 3-7 and discussed in section 3.2.3, that was spin-coated at 2000rpm for a minute followed by a post-bake at 195^{O}C for another minute. The writing parameters used are the following: the working distance was 10mm, the aperture 10μm and the write field size usually 10μm, but a smaller write field size (10, 20μm) was used for dense patterns of small nanostructures with small gaps in between them. Two different accelerating voltages were used, 10 and 20kV, for which the area dose changed; in the case of 10kV accelerating voltage, the area dose used was 115μAs/cm^2, whereas in the case of 20kV accelerating voltage the area dose was 225μAs/cm^2. The area dose value was optimized performing an area dose test writing, as explained in the last paragraph of section 3.3. The electron beam current was determined by the accelerating voltage and the aperture size, the step size used was 2nm, limited by the hardware, and the dwell time was automatically calculated using Eq.(3-10).

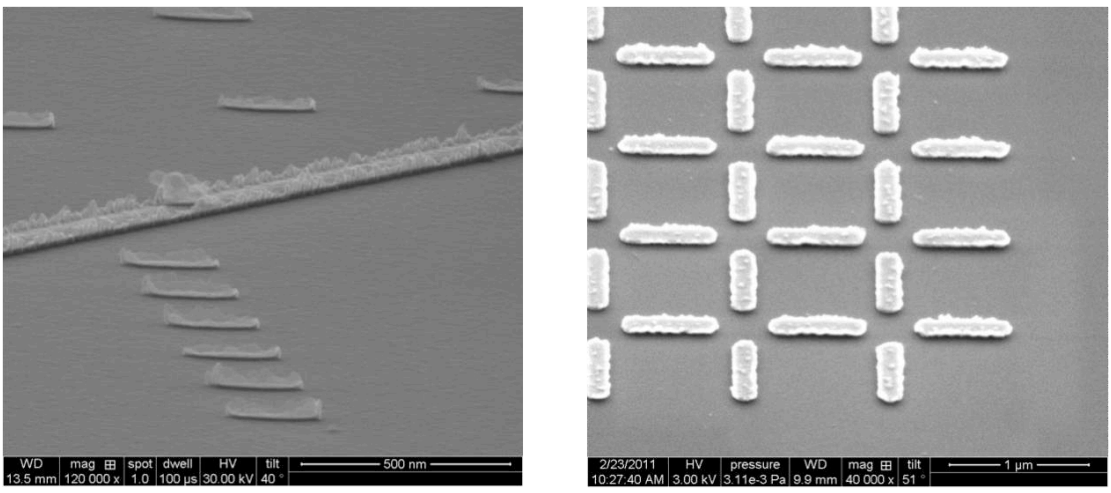

Figure 3-14: Nanostructures written with a single layer 950K PMMA A2 resist.

The nanostructures written with this recipe, irrespective of the accelerating voltage used, showed the same problem: the edges of the nanostructures are very sharp, due to the fact that the material deposited is in direct contact with the walls of the resist and gets attached to them, as can be observed in Figure 3-14 in two different nanostructures fabricated following this single-layer resist recipe. For this reason, double-layer resist recipes forming an undercut profile after exposure and developing of the resist were implemented.

The first double-layer recipe used a bottom layer of 495K PMMA A2 resist and a top layer of 950K PMMA A2, both spin-coated at 4000rpm for one minute, baking the resist at 195^{O}C for one minute after spin-coating each layer. The process is sketched in Figure 3-8, and the writing parameters used are the same than the used in the single-layer resist recipe, but this time a third accelerating voltage, of 3kV, was also used. The area dose used for this voltage was 35μAs/cm^2, being this value optimized again performing an area dose test writing, and the corresponding dwell time adjusted according to Eq.(3-10).

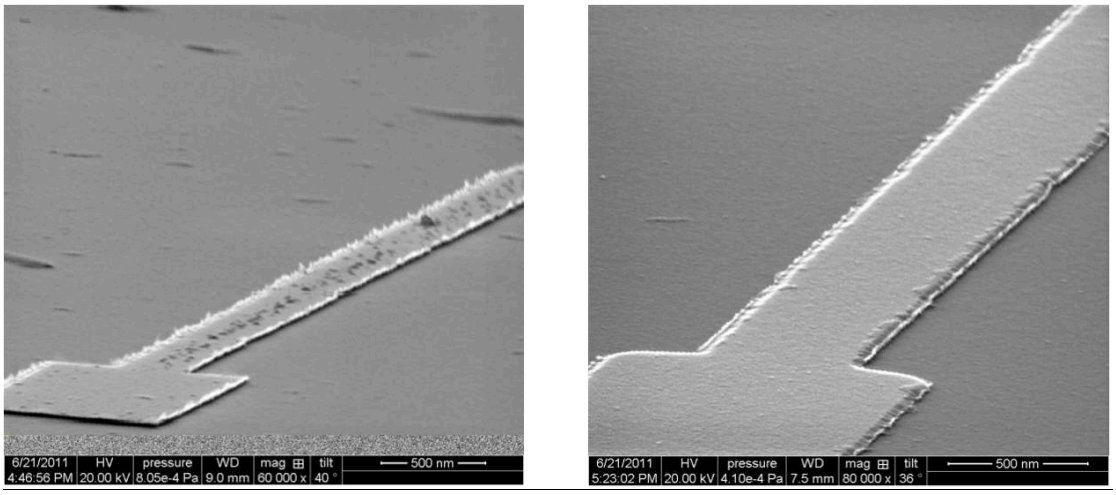

Figure 3-15: Nanostructures written on the same substrate with a double PMMA layer resist recipe; the accelerating voltage used in the left was 10kV, whereas the one used in the right was 3kV.

This double-layer PMMA-based resists recipe yields better output on the edges of the lithographed nanostructures, as observed in Figure 3-15. Nevertheless, the shape of the edges depends strongly on the accelerating voltage used in the recipe; when an accelerating voltage of 10kV is used, the edges are still sharp,

whereas when the accelerating voltage is 3kV no sharp edges are observed, with a clear evidence of the undercut profile in the resist (there is a slope in the edge of the material towards the substrate, as observed on the right image on Figure 3-15). This is due to how the secondary electrons' scattering events affect the two resist layers; in the case of 10kV there are more scattering events in the top resist layer than in the case of 3kV, and this affects the undercut profile. In the case of 10kV the undercut profile is less pronounced because the top layer has been more exposed than in the case of 3kV, and after developing the hole in the top layer is bigger in the case of 10kV. Therefore, the material is still attached to the resist walls in this case, whereas the undercut profile is bigger with a 3kV accelerating voltage and the deposited material does not touch the resist walls. Nevertheless, there is a big drawback when reducing the accelerating voltage (and the area dose and related parameters, as already explained above) to 3kV: the exposure time increases, and writing dense patterns of small nanostructures with this recipe takes a long time (i.e. more than 5 hours for a 100x100μm square made of 300x100nm nanoislands with gaps of 50nm between them).

In order to overcome this problem a third recipe was optimizing, another double-layer resist procedure with a bottom layer of LOR01B resist below a 950K PMMA A2 resist layer. Again, both resist layers are spin-coated at a speed of 4000rpm for one minute, followed by a post-bake of the resist at 225^{0}C for 15 minutes in the case of the LOR01B resist layer, and at 195 ^{0}C for one minute in the case of the 950K PMMA A2 resist. The accelerating voltage used with this recipe is 20kV, with an area dose of 225μAs/cm^{2}. Using these parameters the writing time is strongly reduced compared to the case of using an accelerating voltage of 3kV.

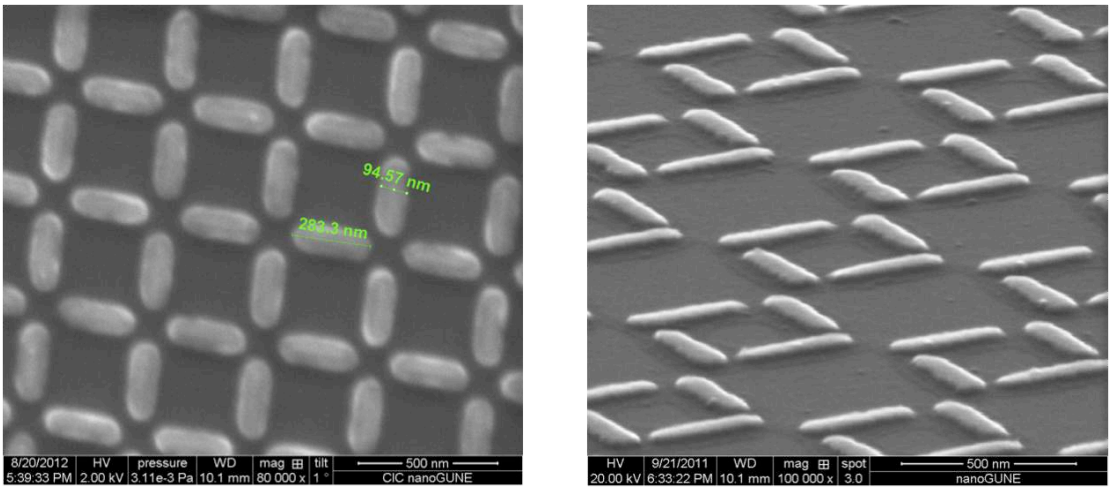

Figure 3-16: nanostructures written with a double layer LOR01B-950K PMMA A2 resist recipe and an accelerating voltage of 20kV.

There is an important difference between the two double-layer resist recipes studied here: with this recipe the undercut profile is controlled in the developing process, as each resist layer is developed by a different chemical (because they are based in different polymers), and in the previous case the undercut profile is controlled in the exposure process, as both resist layers are developed with the same chemical. This control on the undercut profile is the key advantage of this second double-layer resist recipe: whereas the resolution of the writing process is still determined by the top PMMA layer, the bottom LOR layer serves as a control layer to determine the undercut profile shape; the accelerating voltage (and the rest of the parameters to be adjusted when it changes) determine the resolution of the process and the undercut profile is determined by the developing time of the bottom LOR layer. Examples of nanostructures fabricated with this double-layer recipe with LOR and PMMA resists can be observed in Figure 3-16.

The main conclusions that are drawn from this discussion of the results obtained with the three nanofabrication recipes studied in this thesis can be summarized as follows:

- A single PMMA-based resist layer electron beam lithography process results in nanostructures with sharp edges.

- A double-layer resist electron beam lithography process can help to avoid rough edges, due to the undercut profile formed after the developing step.
- The accelerating voltage is a key parameter in a double-layer resist process: a double-layer with PMMA-based resists works nice with 3KV accelerating voltage, but the exposure time increases with respect to higher accelerating voltages.
- A double-layer resist process with a bottom PMGI-based resist and a top PMMA-based resist permits a perfect control of the undercut profile in the developing stage, and an accelerating voltage of 20kV produces dense patterns of small nanostructures with high-resolution without increasing the exposure time.

3.8. References

[1] P. Cummings, *ORNL Review* **38,** 3 (2005)

[2] J. Meng, J. Duan, H. Kong, L. Li, C. Wang, S. Xie, S. Chen, N. Gu, H. Xu and X. D. Yang, *Small* **4(9)**, 1364-70 (2008)

[3] Z. Yin, H. G. Nguyen, S. Chowdhury, P. Bentley, M. A. Bruckman, A. Miermont, J. C. Gildersleeve, Q. Wang and X. Huang, *Bioconjugate Chem.* **23 (8)**, 1694-1703 (2012)

[4] D.L. Tolliver, "Handbook of contamination control", Noyes publications, ISBN 0815511515 (1988)

[5] W Liang, MP Shores, M Bockrath, JR Long and H Park, *Nature* **417**, 725-729 (2002)

[6] A. A. Tseng, K. Chen, C. D. Chen, and K. J. Ma, *Ieee Transactions on Electronics Packaging Manufacturing* **26**, 141-149 (2003)

[7] G. Möllenstedt and R. Speidel, proceedings of 3rd Symposium on Electron Beam Technology, pp 340-357, (1961).

[8] F. Robin, "Electron-Beam Lithography Applications at ETH Zurich", Raith application note, Raith GmbH (2006).

[9] Technical description of the Raith 150TWO instrument, Raith, Germany

[10] L.J. Martinez, I. Prieto, B. Alen, P.A. Postigo, *J. Vac. Sci. Technol. B* **27**, 1801 (2009)

[11] D.J. Grant, "Electron Beam Lithography: From Past to Present", University of Waterloo (2003)

[12] M. Isaacson and A. Murray, *J. Vac. Sci. Tec*. **19 (4)**, 1117-1120 (1981)

[13] D. R. S. Cumming et al., *Appl. Phys. Lett*. **68**, 322-324 (1996)

[14] S. Yasin et al., *Appl. Phys. Lett.* **78**, 2760-2762 (2001)

[15] M. Schnell, P. Alonso-Gonzalez, L. Arzubiaga, F. Casanova, L. E. Hueso, A. Chuvilin and R. Hillenbrand, *Nat. Phot*. **5**, 283-287 (2011)

[16] P. Alonso-Gonzalez *et al.*, *Nano Lett*. **11(9)**, 3922-3926 (2011)

[17] P. Vavassori *et al*., *Phys. Rev. B* **80**, 125132 (2009)

[18] F. Rohlrich and B.C. Carlson, *Phys. Rev.* **93**, 38-44 (1954)

[19] R.A. Bonham and T.G. Strand, *J. Chem. Phys*. **39**, 2200-2204 (1963)

[20] N. Samoto and R. Shimizu, *J. Appl. Phys*. **54**, 3855-3859 (1983)

[21] D. F. Kyser and N. S. Viswanathan, *J. Vac. Sci. Technol*. **12(6)**, 1305-1308 (1975)

[22] W. Moreau and C. H. Ting, "High sensitivity positive electron resisit," *US Patent* 3934057, (1976)

4. Experimental characterization techniques

4.1. Structural Characterization

4.1.1. Atomic Force Microscopy

Atomic force microscopy is one of the imaging techniques enclosed in the group of the so-called scanning probe microscopy (SPM) techniques, which are based on utilizing a physical probe to scan the surface of the sample to be imaged. The beginnings of atomic force microscopy date from 1986, when G. Binning and coworkers at Stanford University invented this tool [1], using it to obtain the lattice image of the surface of graphite one year later [2]. This technique has quickly been developed up to nowadays, when it has become a powerful surface analysis technique for micro and nanoscaled materials. The atomic force microscope (AFM) was invented five years after the invention of the scanning tunneling microscope (STM) by Binning and Rohrer [3], overcoming the main inconvenient of the STM technique: it was only capable of studying metallic or semiconducting materials that are able to establish a tunneling current between a metallic tip and the material to be imaged. This limitation does not exist in the atomic force microscopy technique, as the forces in which AFM is based are the already naturally existing interacting forces between atoms and molecules, which can be either long-range or short-range forces as well as attractive or repulsive. These forces exist in every single material and, therefore, the AFM technique is applicable in any kind of material.

The AFM works by measuring the deflection of an elongated cantilever where a small conic probe is located at one of the edges of a flexible cantilever, whereas the other edge is put in contact with a piezoelectric material (Figure 4-1). A laser spot incides on the back part of the probe in the edge of the cantilever and its reflection position is detected by a photodetector; the position of the reflection

of the laser in the photodetector will change according to the lateral and vertical movements occurring in the cantilever, which are due to the forces generated on the probe by its interaction with the sample.

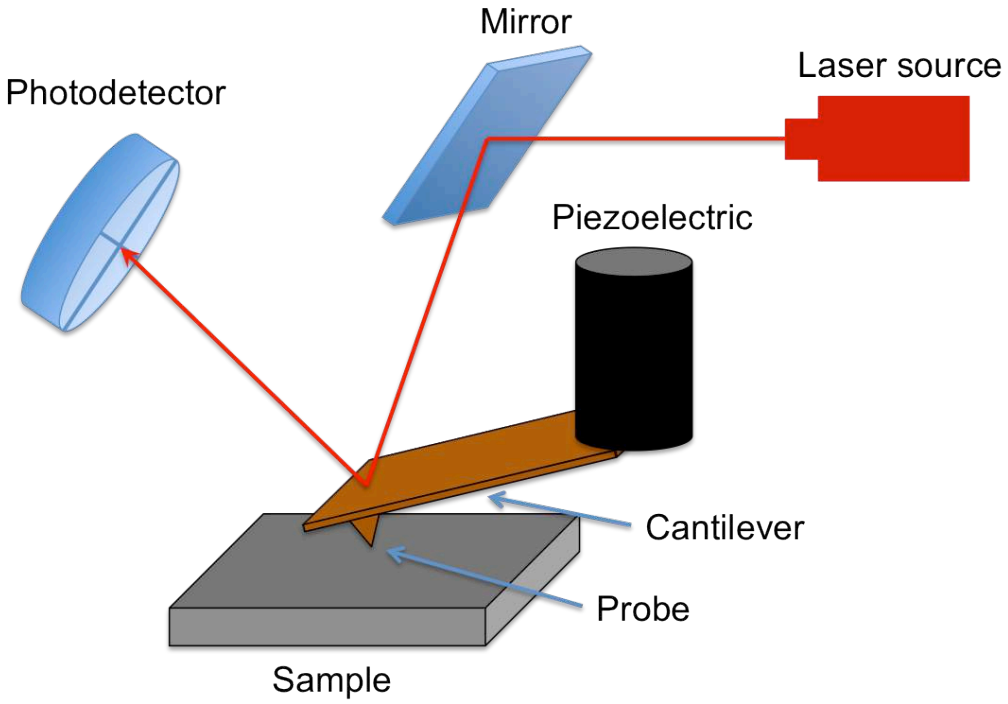

Figure 4-1: Components of an Atomic Force Microscope

Across the history of the atomic force microscopy different functionalities have been discovered for the technique. Already in 1986, after the invention of the AFM, the microscope was found to be also working as a frictional force microscope [4], capable of obtaining images with lattice periodicity. Two years later, in 1988, scientists resolved the methyl groups of the DL-leucine molecules in aminoacid crystals [5], and in 1990, already measuring in ultra high vacuum with an AFM tool the lattice image of NaCl (001) was measured [6]. It was the first time that the AFM reached atomic resolution under ultra high vacuum conditions. In 1991 this atomic resolution was used for the first time to study electrochemical reactions in liquids [7], and two years later, in 1993, using an optical beam deflection method in the AFM, scientists found that the technique served as a two-dimensional frictional force microscope [8]. All these achievements were obtained using a simple contact AFM measurement (the AFM measurement methods will be discussed later in this section), and already by

1993 many applications were already demonstrated for the AFM technique. Nevertheless, Pethica and Oliver demonstrated that this contact AFM measurement method was not able to observe atom vacancies or related atomic defects [9], and in 1993 atomic resolution that showed STM-like reliability in a calcite sample in aqueous environment was obtained [10]. In 1995 non-contact AFM measurements of atomic vacancies in InP (110) were successfully made by two different groups [11, 12]. The first international workshop on noncontact AFM was held at Osaka University in 1998, and many interesting results arose from the workshop: 3D mapping of atomic forces in Si (111) [13], atomic resolution in metal surfaces of Cu (111) [14] and Ag (111) [15] and in adsorbed acetate ions on a TiO_2 (110) surface [16], among many other contributions. This workshop was the starting point for a rapid and continuing growth of the non-contact AFM field, which nowadays has achieved the following capabilities:

- True atomic resolution
- 3D atomic force spectroscopy
- Measurements on insulating samples
- Control of atomic forces
- Measurement of mechanical response
- Mechanical manipulation of individual atoms
- Mechanical atom by atom assembly

The interaction forces acting on the probe come from different sources depending on the distance between the tip and the sample, as it is the case of electrostatic and Van der Walls forces. All these forces can be modeled into a Lennard-Jones potential:

$$V(z) = -V_0 \left[\left(\frac{z_0}{z} \right)^{12} - \left(\frac{z_0}{z} \right)^{6} \right] \qquad (4\text{-}1)$$

where z is the effective interatomic distance between the probe and the surface of the sample and V_0 is the value of the potential at the equilibrium distance z_0. The first term in the equation dominates at short-range distances and it is

repulsive due to the electrostatic potential, whereas the second term is attractive and dominates at long-range distances, and the Van der Walls forces are mainly responsible for this attraction in that distance regime. Given the shape of this potential, the net force acting on the probe will be attractive when the distance between the tip and the sample is relatively big and repulsive for small distances. Depending on the dynamics of the cantilever and on the distance between the probe and the cantilever (i.e. the type of interaction dominating), there are two main groups of AFM operation modes: static and dynamic modes.

4.1.1.1. Static operation mode: contact AFM

In this operation mode the probe is in permanent contact with the surface of the sample and the interaction forces between the two give rise to a vertical deflection of the cantilever. This deflection is attractive or repulsive depending on whether if the AFM is working on the attractive or repulsive mode, respectively, and the amount of deflection produced on the cantilever is proportional to both the interaction strength and the cantilever spring constant [17]. In this static contact AFM mode the interaction force between the probe and the surface is kept constant, and while scanning the probe over the surface of the sample the topology of the surface will provoke variations on the deflection of the cantilever. This deflection of the cantilever is the feedback signal in the contact mode, and the vertical variations of the reflection of the laser from the cantilever on the photodetector gives the topography of the surface of the sample.

The curvature radius of the probe (10-50nm) is usually much bigger than the topology of many of the surfaces to be imaged with the AFM; this means that the interaction zone between the probe and the sample is big, which decreases the resolution and does not allow obtaining true atomic resolution [18]. Another disadvantage of this mode is that it can damage the sample that is being imaged; in order to avoid this, as the deflection of the cantilever has to be bigger than the deformations produced in the probe and the sample, there are some restrictions

on the value of the spring constant of the cantilevers, which are in the range of 0.01 to 5 N/m.

4.1.1.2. Dynamic AFM modes

The dynamic modes came into play in AFM microscopy to circumvent the problems and drawbacks generated in the static contact mode. To operate in this mode the cantilever is set to vibrate to a certain frequency, usually in the range of 10-500 KHz, by coupling the edge of the cantilever opposite to the probe to a piezoelectric material that is electrically excited and makes the cantilever vibrate at its resonant frequency. When the probe is close to the surface the interaction between the probe and the surface change the oscillation characteristics of the cantilever by changing its amplitude, phase and resonant frequency. The shifts of any of these quantities can be taken as feedback signals to form the AFM image, giving different information of different properties of the sample. Usually the resolution obtained with dynamic modes is higher than what is obtained with the static mode, due to the fact that the noise when measuring the cantilever deflection in dynamic modes varies inversely with respect to the frequency [19].
There are two different operation modes within the dynamic mode: the so-called *tapping* mode (also called intermittent or AC mode), where the feedback signal is the oscillation amplitude of the cantilever, and the *non-contact* mode (also called frequency modulation mode), where the feedback signal is the oscillation frequency of the cantilever.

4.1.1.2.1. Tapping mode

In the tapping mode the cantilever is set to vibrate to a certain frequency close to its resonant frequency with big amplitude, on the order of 100-200nm. This amplitude is higher than the distance between the probe and the sample when the cantilever is not vibrating, so that the probe-sample contact happens only at the lowest point of the amplitude of the cantilever. The main advantage of this mode is that the lateral forces are subtracted, therefore increasing resolution,

and the vertical forces are also minimized with respect to the contact mode, so that the sample is not damaged. Another advantage of this mode is that, as it is not invasive, it is possible to study small molecules slightly adhered to substrates, which is impossible to measure in the contact mode. Finally, using big amplitudes helps to avoid adherence of the probe to the sample.

The oscillation amplitude of the cantilever decreases when the probe interacts with the sample, and this change of the amplitude is used as the feedback signal in this mode, as already stated before. When the probe is interaction-free (far from the sample) the amplitude oscillation is set to a certain value that in the presence of interactions will change. When the probe is close to the surface of the sample if there is a 'mountain' in the topography the sample-probe distance decreases and the interaction strength is increased, decreasing therefore the oscillation amplitude, whereas if there is a 'valley' in the topography the sample-probe distance increases and the interaction strength decreases, making the oscillation amplitude to increase. Apart from the changes in the amplitude the phase of the signal also changes, which is sensitive to different properties of the sample that is being measured (such as the variation on the chemical composition of the sample, adhesion or other surface properties that do not appear with a single topography measurement), and the feedback of the phase signal is used in different operation modes in the AFM such as the Electrostatic Force Microscopy (EFM) or Magnetic Force Microscopy (MFM), which will be discussed later in this chapter.

4.1.1.2.2. Non-contact AFM mode

With this dynamic AFM mode it is possible to reach atomic resolution in a consistent way [20], and is based on the fact that the distance between the surface and the probe is big enough so that the forces acting on the probe are only attractive. The feedback signal in this mode is the frequency shift on the cantilever oscillation produced by the probe-sample interaction required to maintain a constant oscillation amplitude during the whole measurement. The

oscillation amplitudes usually employed in the non-contact dynamic AFM mode are in the range from one to 40nm [21], smaller than the usual values employed in the tapping mode.

The AFM tool used in this thesis is an Agilent® 5500 Atomic Force Microscope, which can be observed in Figure 4-2.

Figure 4-2: Agilent 5500 AFM present at CIC nanoGUNE.

4.1.2. X-Ray Reflectivity: thin film thickness analysis

The thickness of the thin films deposited to fabricate the nanostructures subject of study in this thesis has been analyzed by means of x-rays reflectivity (XRR) measurements, which is a non-destructive and non-contact technique capable of measuring thicknesses in thin films up to around 200nm with a resolution of one angstrom [22,23]. This technique, besides being widely used for thin film thickness analysis, also gives information about the density and roughness of the measured thin films.

The x-ray reflectivity technique is based on recording the intensity of a monochromatic x-ray beam with a certain wavelength λ that irradiates a thin film at a grazing (very low) angle ω by a detector located at an angle 2θ from the incident x-rays direction, as observed in Figure 4-3.

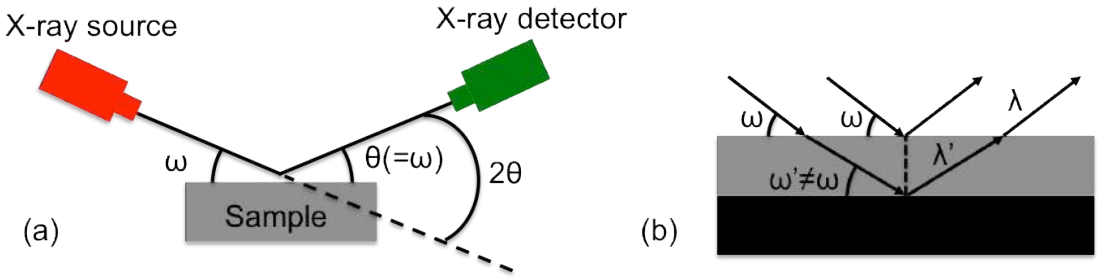

Figure 4-3: scheme of the θ -2θ X-Ray reflectivity operation method (a), and scheme of the reflections in the different interlayers of the X-rays in an X-ray diffraction measurement (b).

The mode of operation of is called θ -2θ given by the incident and diffraction angles' values (see Figure 4-3), and the reflection at the surface and interface occurs due to the difference in electron densities in the different layers, giving rise to a difference in the refractive indexes of the different layers. There is a critical angle θ_c below which total reflection of the x-rays occur, which is determined by the electron density of the material (and, therefore, by its refractive index), and above that critical angle the interference between reflected x-rays from different interfaces (air-film and film-substrate) give information about the thickness and roughness of the film. Given that the refractive index in the x-ray region is smaller than one and is given by $\bar{n} = 1 - \delta + i\beta$, where δ is the dispersion and β the absorption, considering an absorption-free film the critical angle is determined by this equation (from the Snell's law):

$$1 - \delta = cos\theta_C \qquad (4\text{-}2)$$

When the incident angle is greater than the critical angle there is reflection at both interfaces and the interference between the reflected rays from the two interfaces can be either constructive or destructive, depending on the film thickness d, according to the Bragg law:

$$m\lambda' = m\left(\frac{\lambda}{n}\right) = 2d \cdot \sin(\omega') \qquad (4\text{-}3)$$

where m is the interference order. Sweeping the incident angle θ between 0° and 5° it is possible to measure the intensity patterns formed by the constructive and destructive interferences of x-rays reflected from both interfaces, and the film thickness, which is the difference in distance between the two reflection planes, is determined using Eq.(4-3).

The system present in nanoGUNE with which the thin film thickness analysis has been performed is a *Panalytical X-Ray Diffraction* system hardware, which comes with the software *Panalytical Xpert Reflectivity* that fits the experimental data obtained with the hardware. This system can be observed in Figure 4-4.

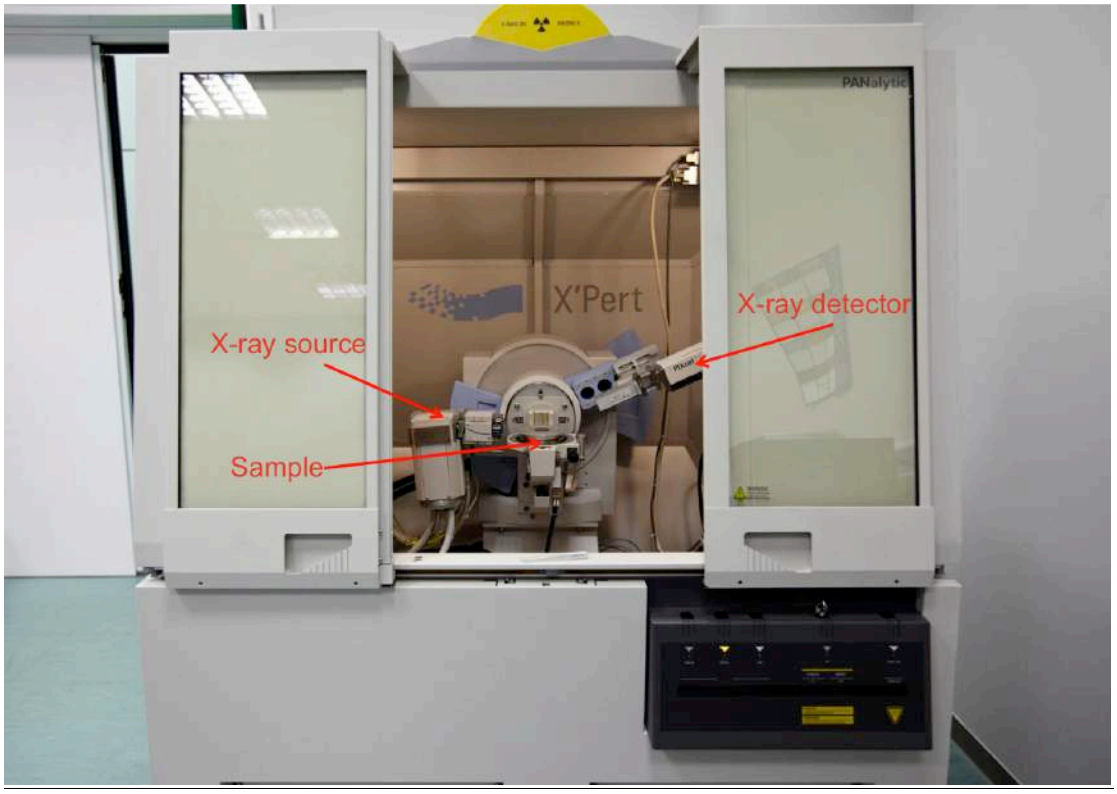

Figure 4-4: Panalytical X-Rays Diffraction system at nanoGUNE.

4.2. Magnetic Characterization

4.2.1. Magnetic Force Microscopy

The origin of the magnetic force microscopy (MFM) technique comes from 1987, when Y. Martin and H. K. Wickramasinghe mounted a magnetically coated probe on an atomic force microscope [24] and successfully imaged magnetic domains in a magnetic sample with a resolution of 100nm. This magnetic imaging technique is a variant of the AFM technique and is capable of mapping the domains of a magnetic sample in real space. The working principle of the MFM is the same than that of the AFM; i.e., a force between the probe and the sample surface provokes a deflection of the cantilever that is measured by monitoring the movements of the reflection of a laser from the edge of the cantilever on a pthotodiode, but in this case the force acting between the probe and the sample is a magnetic force. The major requirement to perform magnetic force microscopy imaging is utilizing a magnetically coated probe on a magnetic surface, as the magnetostatic interaction between the probe and the sample is usually fairly strong and independent of surface contamination, making the technique easy to perform and versatile under various environmental conditions.

The magnetic coupling between the probe and the surface of the magnetic sample depends on the stray field generated by the sample and the internal ferromagnetic structure of the probe. The shape of the magnetic probes used in magnetic force microscopy measurements is sharper than other non-magnetic probes used for standard AFM, so that the ferromagnetic probe naturally exhibits a big magnetic shape anisotropy that forces the magnetization of the probe to be aligned to the symmetry axis of the probe. Nonetheless, far from the probe apex the magnetization of the part of the probe that is closer to the cantilever is determined by the detailed magnetic properties of the material represented by the exchange, anisotropy and magnetostriction energies. In order to explore the magnetic interactions between the probe and the sample it is

reasonable to model the magnetization vector field in the probe apex by a homogeneously magnetized prolate spheroid, which interacts with the stray field generated by the magnetic sample and whose magnetization and dimensions are completely rigid independently of any external stray field produced by the sample [25].

Within this model many of the experimental results obtained with the magnetic force microscopy technique can be reproduced with a strong agreement. The stray field generated by a magnetic sample is given by:

$$\vec{H}_S(\vec{r}) = -\nabla\phi_S(\vec{r}) \qquad (4\text{-}4)$$

where $\phi_S(\vec{r})$ is the magnetostatic potential created by a ferromagnetic sample:

$$\phi_S(\vec{r}) = \frac{1}{4\pi}\left(\int_S \frac{\vec{M}_S(\vec{r})\cdot d^2\vec{s}'}{|\vec{r}-\vec{r}'|} - \int_V \frac{\nabla\cdot\vec{M}_S(\vec{r})}{|\vec{r}-\vec{r}'|} d^3\vec{r}'\right) \qquad (4\text{-}5)$$

being $\vec{M}_S(\vec{r})$the magnetization vector of the sample, $d^2\vec{s}'$ a unit vector normal to the sample surface, the first integral covering the surface magnetic charges created by the magnetization component perpendicular to the sample surface, and the second one covering the volume magnetic charges resulting from the divergence of the magnetization vector. The force acting on the magnetic probe from the interaction between the probe and the stray field created by the sample is given by:

$$\vec{F}(\vec{r}) = -\nabla\psi(\vec{r}) \qquad (4\text{-}6)$$

where $\psi(\vec{r})$ is the magnetostatic free energy of the magnetic probe under the action of the stray field $\vec{H}_S(\vec{r})$, and is given by this equation:

$$\psi(\vec{r}) = \mu_0\left(\int_S d^2\vec{s}' \cdot \vec{M}_P(\vec{r}')\phi_S(\vec{r}') + \int_V d^3\vec{r}'\, \nabla_{\vec{r}'} \cdot \left[\phi_S(\vec{r}')\vec{M}_P(\vec{r}')\right]\right) \qquad (4\text{-}7)$$

where $\vec{M}_P(\vec{r}')$ is the magnetization vector of the probe. Therefore, the force that is sensed by the magnetic probe is the negative gradient of the expression shown in Eq.(4-5), where the first integral gives account for the interaction of the stray field with free surface charges and the second integral has to do with the magnetic probe's dipolar moment and possible volume divergences (which according to the model [25] would be reduced to the dipolar response of the probe, as the probe is divergence free).

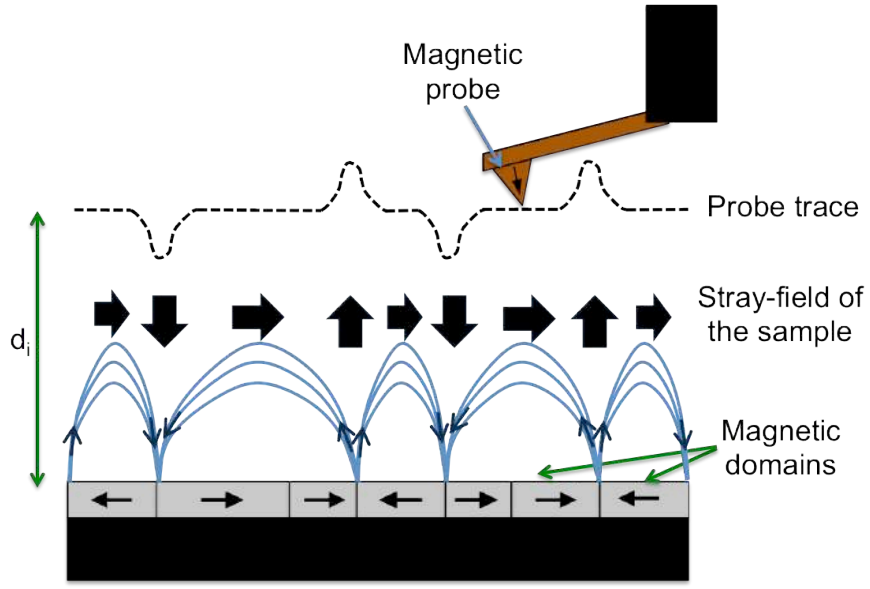

Figure 4-5: schematic analysis of the working principle of a Magnetic Force Microscope.

This model to interpret the magnetic contrast formation in magnetic force microscopy imaging can be further simplified in may cases with successful results, just by treating the magnetic probe as a point-like magnetic probe of quasi-zero size located at a certain distance from the magnetic surface of the sample. This is the so-called point-probe approximation [26], where the force acting on the probe is given by:

$$\vec{F}(r) = \mu_0(q + \vec{m}(r) \cdot \nabla)\vec{H} \qquad (4\text{-}8)$$

where q and $\vec{m}(r)$ are the monopolar and dipolar monents of the infinitesimal magnetic probe, and $\nabla \times \vec{H} = 0$ is assumed. Nevertheless, the instrument detects the vertical force component that bends the cantilever, which is given by:

$$F_z(\vec{r}) = \vec{k} \cdot \vec{F} = \mu_0 \sum_{i=1}^{3} n_i \left(qH_i + \sum_{j=1}^{3} m_j \frac{\partial H_j}{\partial x_i} \right) \qquad (4\text{-}9)$$

where $\vec{k}$ is the unit vector in the z component (perpendicular to the sample surface). With this equation the MFM contrast can be obtained when it is operated in the static mode. For dynamic modes, where the MFM instruments are usually operated, the probe oscillates with certain amplitude that is smaller than the probe-sample distance, and the component that is detected by the instrument is given by:

$$F_z(\vec{r}) = \left(\vec{k} \cdot \nabla\right) \cdot \left(\vec{k} \cdot \vec{F}(\vec{r})\right) \qquad (4\text{-}10)$$

where $\vec{F}(\vec{r})$ is given by Eq.(4-6). When developing this Eq.(4-8) one finds dynamic pseudopotentials $\phi_i^p = \frac{\partial q}{\partial x_i}$ and pseudocharges $q_{ji}^p = \frac{\partial m_i}{\partial x_i}$ due to the fact that the magnetic response of a real probe of finite size depends on its instantaneous position with respect to the sample surface.

The magnetic force measurements (schematized in Figure 4-5) performed in our system at nanoGUNE have been done following a double trace-retrace scanning at the same linescan, consisting of performing first a scan to obtain a picture of the topography of the surface and then, after lifting the probe to a certain interleave height (d_i in Figure 4-5), perform a second scan in order to provoke deflections on the cantilever due to the magnetic interaction described in the previous paragraphs. This method is illustrated in Figure 4-6.

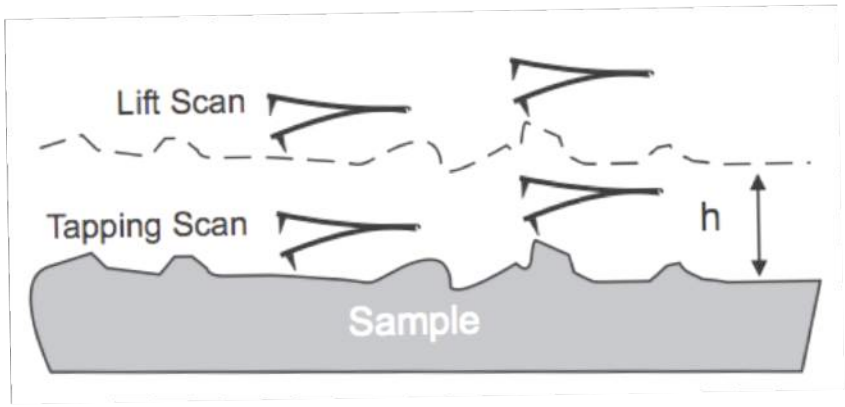

Figure 4-6: Double trace-retrace MFM working method.

4.2.2. MOKE magnetometry

By the beginning of the 19th century many physicists were studying the relation between light and the forces already known by that time, and the preliminary conclusions of these works were that, intuitively, the interaction of light with electric fields was more evident than with magnetic fields. Already in 1845 Michael Faraday discovered the first magneto-optic effect, the so-called 'Faraday effect', which states that a magnetic field applied to a transparent magnetic material through which polarized light passes rotates the polarization plane of the light [27]. His next objective was to study what happened with a non-transparent magnetic surface where the light was reflected, but his studies did not draw any important conclusion due to imperfections of the material that he was studying [28]. The first scientist that gave a microscopic explanation of this magneto-optic effect was Lord Kelvin in 1856 [29], and in 1873 Maxwell presented an explanation from a macroscopic point of view [30], proposing that a linearly polarized light can be expressed as the superposition of two circularly polarized lights, effect known as the circular birefringence. In 1877 John Kerr discovered an equivalent effect to the Faraday effect, but with light being reflected from a magnetic surface [31, 32]: this is the so-called Magneto-Optic Kerr Effect (MOKE), issue of study in this section of the thesis.

There are two different approaches to explain the origin of the magneto-optic Kerr effect: the macroscopic and the microscopic descriptions. From a

macroscopic point of view this effect can be understood as follows: the incident light wave causes the electrons present in the magnetic material to oscillate in a plane parallel to the plane of polarization of the electrons. If there is no magnetization in the sample, and if the incoming light is linearly 's' or 'p' polarized, or circularly polarized, the reflected light will have the same polarization as the incoming one. But if the sample has a net magnetization the internal magnetic field acts on the electrons that are being displaced by the electric field of the light; the Lorentz force introduces an additional small oscillating component to the motion of the electrons that is perpendicular to the plane individuated by the magnetization and the electric field vectors, and superimposing both contributions, with their relative phase, to the vibrating motion of the electrons present in the magnetic material results in a slightly elliptical polarization state of the reflected light.

From a microscopic point of view the magneto-optic Kerr effect occurs due to the spin-orbit coupling between the electric field of the light and the wavefunction of the spin of the electrons in the magnetic material [33]. This coupling provokes a change on the polarization of the reflected light that depends on the magnetization of the magnetic material.

In order to analyze the phenomenology of the magneto-optic Kerr effect from a macroscopic point of view Fresnel's theory of reflection is usually employed. The Fresnel reflection matrix R relates the incoming and reflected light waves through this equation:

$$\begin{pmatrix} E_p^r \\ E_s^r \end{pmatrix} = R \cdot \begin{pmatrix} E_p^i \\ E_s^i \end{pmatrix} \tag{4-11}$$

$$R = \begin{pmatrix} r_{pp} & r_{ps} \\ r_{sp} & r_{ss} \end{pmatrix} \tag{4-12}$$

In these equations the indexes *i* and *r* mean incoming and reflected waves, respectively, and the indexes *p* and *s* define the electric field components parallel

and perpendicular to the plane of reflection. The coefficients of the Fresnel matrix are calculated via the dielectric tensor (ε), which is given by:

$$\varepsilon = -\varepsilon_0 \begin{pmatrix} 1 & -iQ_V m_3 & iQ_V m_2 \\ iQ_V m_3 & 1 & -iQ_V m_1 \\ -iQ_V m_2 & iQ_V m_1 & 1 \end{pmatrix} \quad (4\text{-}13)$$

where ε_0 is the vacuum permittivity, m_i are the components of the magnetization vector of the sample and Q_V are the Voigt material constant characteristic of each optically active material, which are photon-energy (or wavelength) dependent [34]. To calculate the components of the Fresnel reflection matrix boundary conditions for the electric and magnetic fields are imposed: continuity on the tangential components of the electric and magnetic fields to the surface of the magnetic material is required. With these conditions, and solving Maxwell equations for the dielectric tensor expressed in Eq.(4-13) the elements of the Fresnel reflectivity matrix r_{ij} , which are the ratio of the incident *j* polarized component of the incoming light and the reflected *i* polarized component, are expressed as [35]:

$$r_{ss} = \frac{n_0 cos\theta_i - n_1 cos\theta_r}{n_0 cos\theta_i + n_1 cos\theta_r} \quad (4\text{-}14)$$

$$r_{sp} = \frac{i n_0 n_1 cos\theta_i (m_z cos\theta_r + m_y sin\theta_r) Q_V}{(n_1 cos\theta_i + n_0 cos\theta_r)(n_0 cos\theta_i + n_1 cos\theta_r) cos\theta_r} \quad (4\text{-}15)$$

$$r_{ps} = \frac{i n_0 n_1 cos\theta_i (m_z cos\theta_r - m_y sin\theta_r) Q_V}{(n_1 cos\theta_i + n_0 cos\theta_r)(n_0 cos\theta_i + n_1 cos\theta_r) cos\theta_r} \quad (4\text{-}16)$$

$$r_{pp} = \frac{(n_1 cos\theta_i - n_0 cos\theta_r)}{n_1 cos\theta_i + n_0 cos\theta_r} - \frac{i 2 n_0 n_1 cos\theta_i sin\theta_r m_x Q_V}{(n_1 cos\theta_i + n_0 cos\theta_r)(n_0 cos\theta_i + n_1 cos\theta_r) cos\theta_r} \quad (4\text{-}17)$$

where n_0 and n_1 are the refractive indexes of the nonmagnetic and the magnetic media, respectively (in our case n_0=1, as the MOKE measurements are performed in air), and the angles of incidence and reflection are sketched in Figure 4-7.

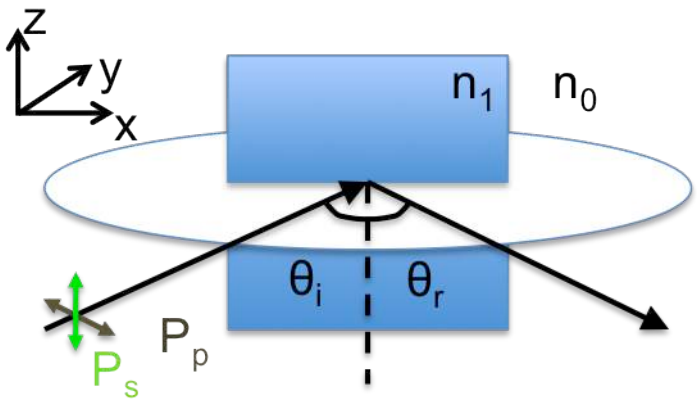

Figure 4-7: MOKE geometry

As observed from Eqs.(4-14) to (4-17) the dependence of the elements of the Fresnel reflectivity matrix r_{ij} with the magnetization components gives some clues about how different incoming polarization configurations would be affected by the magneto-optic Kerr effect; r_{ss} does not have any dependence on any component of the magnetization, r_{pp} is only dependent on one of the components of the magnetization (parallel to the incidence plane) and both r_{sp} and r_{ps} depend on two components of the magnetization. This dependence of the elements of the Fresnel reflection matrix are the base of the different geometries in which the MOKE magnetometry technique is based, which will be detailed hereafter. To finish with the analysis of the effect of the magnetization of a sample on the light reflected from a magnetic sample, the quantitative analysis of the change in the polarization of the light is exposed, which is denoted with the analysis of two parameters: the Kerr rotation and the Kerr ellipticity. The Kerr rotation, θ_K, is the rotation of the major axis of the polarization ellipse of the light with respect to the polarization of the incident light, and the Kerr ellipticity, ε_K, is the ratio between minor and major axes of the ellipse, and their expressions [35] can be derived from the elements of the Fresnel reflectivity matrix:

$$\theta_K^p + i\varepsilon_K^p = \frac{r_{sp}}{r_{pp}} \tag{4-18}$$

$$\theta_K^s + i\varepsilon_K^s = \frac{r_{ps}}{r_{ss}} \tag{4-19}$$

Depending on the geometric relations between the magnetization orientation of the sample and the incident plane of the light different MOKE magnetometry configurations are established: Longitudinal, Transverse and Polar MOKE configurations. The longitudinal and transverse Kerr effect configurations are employed when the anisotropy of the sample is in plane, whereas the polar Kerr effect configuration is used to study magnetic samples with out of plane anisotropy magnetization.

4.2.2.1. Longitudinal Kerr effect

In the longitudinal Kerr effect geometry the magnetization lies in the plane of the sample and parallel to the incident plane, as observed in Figure 4-8.

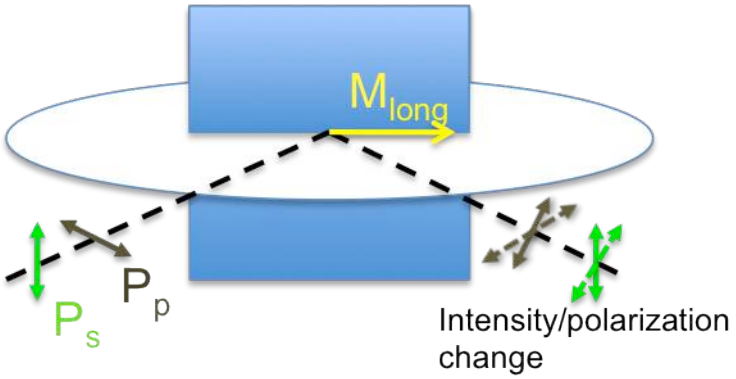

Figure 4-8: Longitudinal Kerr effect configuration

If one thinks of the electric field of the incident polarized light as a field exciting the electrons, so that they oscillate parallel to the incident polarization, this gives rise to a normal component of the light in the reflected beam, whereas another component of the light arises due to the Lorentz force. These two components are generally not in phase and a superposition of the two of them is responsible for the magnetization-dependent (through the Lorentz force) rotation of the polarization. Therefore, generally both *s* and *p* polarized lights will become elliptically polarized (Kerr ellipticity) with its major axes rotated (Kerr rotation). The Longitudinal Kerr effect becomes smaller as the incident angle of the light approaches the normal to the sample plane, in the case of incoming *p* polarized

light due to a vanishing Lorentz force, and in the case of incoming *s* polarized light it points along the same direction.

4.2.2.2. Transverse Kerr effect

In the transverse Kerr effect geometry the magnetization is also in the plane of the sample but, contrary to the longitudinal geometry, it is perpendicular to the incident plane, as can be observed in Figure 4-9.

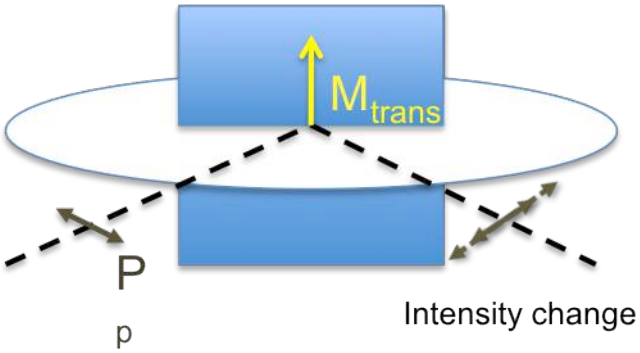

Figure 4-9: Transverse Kerr effect configuration

In this case the two components (the normal one coming from the excitation of the electrons by the incoming electric field and the one from the Lorentz force) are in the same plane (the incident plane) in the case of incoming *p* polarized light, giving rise to a change in the amplitude of the incoming light but without Kerr rotation, and in the case of incoming *s* polarized light there is no effect since there is no Lorentz force acting on it. In conclusion, with this configuration the only affected component of the incoming light is the *p* polarized one, and there is only a change in its amplitude upon reflection from the magnetic sample.

4.2.2.3. Polar Kerr effect

In the polar Kerr effect geometry the magnetization is perpendicular to the sample plane and parallel to the incident plane, as observed in Figure 4-10.

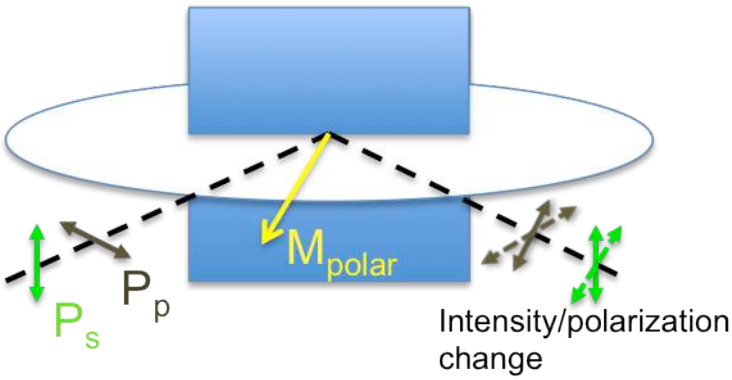

Figure 4-10: Polar Kerr effect configuration

In the polar Kerr effect configuration the behavior of the *s* and *p* polarized lights is similar to the one described for the longitudinal Kerr effect configuration in terms of the superposition of the two components of the light (normal and Lorentz), but in this case, as the magnetization is out of the sample plane and therefore a Lorentz force always exists at normal incidence, the polar Kerr effect does not vanish when the incidence angle gets closer to the normal to the surface.

4.2.3. Diffracted Magneto Optic Kerr Effect

When the magnetic sample from which the light is reflected is not a continuous film but a patterned magnetic media, apart from the reflected beam diffracted beams also arise from the sample, provided that the distance between the structures forming the pattern is comparable with the wavelength of the incoming light. Analyzing the information of the diffracted beams from the sample is the base of the so-called diffracted-MOKE technique [36]. As previously discussed the polar and longitudinal MOKE configurations involve changes in the polarization state of the reflected light and at least two Fresnel reflectivity coefficients are involved, whereas in the case of the transverse MOKE configuration the polarization is maintained and there is only a change on the intensity of the reflected light, being only dependent on one Fresnel reflectivity coefficient, r_{pp} and, for this reason, the analysis of data is simplified when using

the transverse MOKE configuration for the diffracted-MOKE technique. The relevant Fresnel reflectivity coefficient can be split in two parts:

$$r_{pp} = r_{pp}^{nm} + r_{pp}^{m} \tag{4-20}$$

where r_{pp}^{nm} is the non-magnetic part of the reflectivity coefficient and r_{pp}^{m} is the magnetic part. The diffracted electric field of a diffracted light from a non-magnetic patterned surface is generally written as:

$$E_n = E_0 r_{pp}^{nm} f_n^{nm} \tag{4-21}$$

where the subscript n denotes the order of the diffracted beam, E_0 is the electric field of the incident beam and f_n^{nm} is the non-magnetic scattering form factor defined by:

$$f_n^{nm} = \int exp\left(-in\vec{G}\cdot\vec{r}\right)d^2s \tag{4-22}$$

where the integration is performed over one unit cell of the array and $\vec{G}$ is the reciprocal lattice vector of the unit cell. Considering now a magnetic surface the above equations for the electric field of the diffracted beam and the form factor are modified:

$$E_n = E_0 r_{pp} f_n = E_0\left(r_{pp}^{nm} f_n^{nm} + r_{pp}^{m} f_n^{m}\right) \tag{4-23}$$

$$f_n = f_n^{nm} + f_n^{m} = \int exp\left(-in\vec{G}\cdot\vec{r}\right)d^2s + \int m_{\perp}(\vec{r})exp\left(-in\vec{G}\cdot\vec{r}\right)d^2s \tag{4-24}$$

In Eq.(4-24) $m_{\perp}(\vec{r})$ is the magnetization perpendicular to the scattering plane. The intensity of the diffracted beam is given by:

$$I_n = E_n \cdot E_n^* = I_0 + \Delta I_n \tag{4-25}$$

where I_0 is the intensity of the n-th order diffracted beam from a magnetic sample without taking into account the effects of the magnetization and $\Delta I_n\left(m_\perp(\vec{r})\right)$ is the change of the intensity of the diffracted beam due to the magnetization of the sample, which can be expressed as:

$$\Delta I_n = \int m_\perp(\vec{r}) exp\left(-in\vec{G}\cdot\vec{r}\right) d^2s \qquad (4\text{-}26)$$

This integral shown in Eq.(4-26) can be applied to study the changes in intensity of any diffracted beam from a patterned magnetic sample, including the reflected beam (making n=0), in the transverse MOKE configuration. Particularly, when n=0, the equation above gives:

$$\Delta I_0 = \int m_\perp(\vec{r})\, d^2s =< m_\perp > \qquad (4\text{-}27)$$

which is the average magnetization of the sample. Combining the analysis of the reflected beam, where the average magnetization of the sample is obtained, and various n-th order diffracted beams, where the spatial distribution of the magnetization (through the exponential term of the integral) is obtained, a complete understanding of the magnetization behavior is retrieved with this powerful technique. Therefore, one of the main conclusions that can be easily derived from this analysis of the diffracted-MOKE technique is that the intensity in the diffracted spots carries information on the spatial distribution of the magnetization in a patterned magnetic sample. An example of diffracted-MOKE hysteresis loops and their interpretation can be found in [37], where the analysis of the magnetization reversal in an array of square rings made of Permalloy is analyzed, measuring diffracted-MOKE hysteresis loops from high-order diffracted beams, that help to understand the magnetic configurations at each stage of the magnetization reversal process.

4.2.4. MOKE microscopy

Based on the already described magneto optic Kerr effect this microscopy technique is capable of optically resolving different magnetic domains in a magnetic sample. MOKE microscopy can be implemented in a conventional optical microscope to which optical elements can be attached, as well as a CCD camera capable of recording changes of intensity of the reflected light from the sample pixel by pixel. Using this microscope in conjunction with an image processor, Kerr microscopy can extract domain contrast from the surface of any ferromagnetic material without any specific surface treatment, and even allowing thin (up to 5-10nm) coatings on top of the ferromagnetic material to prevent it from oxidation. The scheme of a Kerr microscope can be observed in Figure 4-11, where all the necessary components are included: a light source that can be either a white light halogen lamp or a LED(s) lamp, an aperture slit, a polarizer, mirror(s) and lens(es) to focus the incoming and/or reflected light (depending on the physical geometry of each piece of equipment), an analyzer, a compensator and a recording CCD camera.

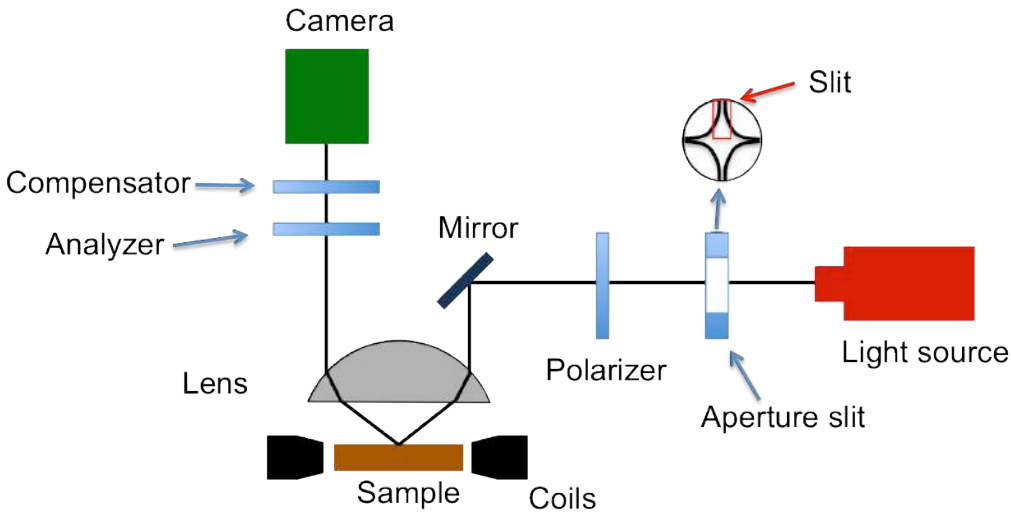

Figure 4-11: components of a conventional Kerr microscope.

The magnetic sample is illuminated with light polarized parallel to the incidence plane, and upon reflection from the magnetic sample, as previously stated when discussing the longitudinal Kerr effect configuration earlier in this chapter, two

components of the electric field on the reflected light are superimposed: one perpendicular to the direction of the propagation of the reflected light (due to the oscillation of the electrons) and another one from the Lorentz force. The interference of the two components results in a change on the polarization state of the light due to the magneto optic Kerr effect, which induces a light rotation by a small angle that, by using an analyzer set at an angle bigger than the rotation angle induced by the Kerr effect on the polarization of the light, leads to the domain contrast. The compensator converts elliptically polarized light into linearly polarized light, which is directly recorded by the CCD camera. One of the main characteristics of this technique is that it is possible to record hysteresis loops of selected regions of the image seen in the microscope with the so-called "region of interest" (ROI) tool, allowing to record local hysteresis loops of nanostructures down to the resolution limit imposed by the Rayleigh criterion for visible light, which is around 300nm [38]. Thanks to the ROI tool it has been possible to record hysteresis loops of single Cobalt wires 20nm thick and below 100nm wide [39, 40]

Another interesting characteristic of this magnetic characterization technique is that the magnification of the microscope is easily modified just by changing the objective, allowing imaging from the centimeter to the sub-micron regime.

Figure 4-12: Evico Kerr Microscope present at the nanomagnetism lab at CIC nanoGUNE.

The Kerr microscopy technique can be used for a wide variety of different magnetic measurements, allowing applying magnetic fields of arbitrary strength and directions, and also heating and cooling of the sample in an optical heating stage or a cryostat to observe thermal phase transitions or other thermal effects.

The Kerr microscope with which the nanostructures studied in this thesis have been analyzed is is an Evico Magnetics Kerr-Microscope system, which can be observed in Figure 4-12. It is a semi-automatic, contact-less measuring system using the magneto optic Kerr effect in a wide-field, optical microscope for full mapping of spot sizes up to 5mm diameter and down to the resolution limit of optical microscopy, already mentioned before. Magnetic in-plane fields of arbitrary directions can be applied during observation so that domain nucleation and magnetization processes are observed while hysteresis loops of the selected places of the sample are measured.

4.2.5. Vibrating Sample Magnetometry (VSM)

A Vibrating Sample Magnetometer (VSM) is an instrument capable of measuring magnetic properties that was invented in 1959 by Simon Forner at the MIT [41]. The VSM tool is based on Faraday's induction law, which specifies that a change in the magnetic flux induces an electric voltage. In a VSM the magnetic sample is moving in the proximity of two pick-up coils that sense the stray field generated by the sample. The sample is mounted in a sample rod (see Figure 4-13) that vibrates with a given frequency and amplitude, and is usually placed in a constant magnetic field so that all the magnetic domains are aligned. This oscillating movement of the sample originates a change in the magnetic flux (from the magnetic stray field of the sample) that is sensed by the pick-up coils where an electric voltage is induced. The constant magnetic field used to magnetize the sample does not create any voltage, as the magnetic flux created by it is zero. The voltage induced by the magnetic flux created by the sample is proportional to the magnetization of the sample and, therefore, with a proper

calibration of the VSM instrument the magnetization of a ferromagnetic sample can be measured.

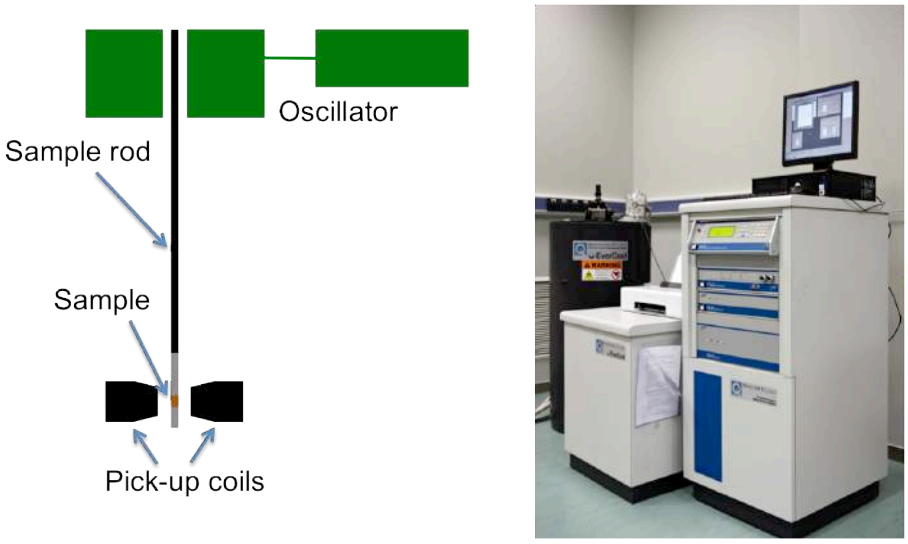

Figure 4-13: Scheme of a VSM magnetometer (left) and the PPMS instrument present at CIC nanoGUNE (right).

The VSM tool has been used in this thesis to investigate the Curie temperature of magnetic samples. For this, a thermocouple is integrated in the sample rod, and is in direct contact with the sample to be measured. The magnetic flux created by the magnetization decreases with the temperature until the sample reaches its Curie temperature, above which no magnetic flux is created. By measuring the voltage induced in the coils by the magnetic flux while increasing the temperature it is possible to draw a Magnetization Vs Temperature curve of the sample, which gives information about the total magnetization of the sample at room temperature and the Curie temperature.

The VSM-oven (to heat the sample) used for this study is part of a Physical Properties Measurement System (PPMS) equipment, which is a Quantum Design PPMS tool with the VSM-oven option integrated in it. With a PPMS it is possible to measure many physical properties of a sample, such as DC resistivity, AC susceptibility, I-V curves, critical currents in superconductors, heat capacities, thermal transport and many others. About the specifications of the tool related to the measurements of the Curie temperature, with the thermocouple of the VSM-oven it is possible to go up to 1000 K in temperature while the sample is

oscillating under a magnetic field as big as up to 1.5 T. The sensitivity of the VSM is below 10^{-5} emu, the temperature precision is 0.5 K and the accuracy of the data acquisition is $1x10^{-5}$ emu.

4.3. References

[1] G. Binnig, US Patent 4724138 (1986)

[2] G. Binnig, C.F. Quate, Ch. Gerber, *Phys. Rev. Lett.* **56**, 930 (1986)

[3] G. Binnig, H. Rohrer, Ch. Gerber and E. Weibel, *Phys. Rev. Lett*. **49,** 57 (1982)

[4] C.M. Mate, G.M. McClellend, R. Erlandsson and S. Chiang, *Phys. Rev. Lett*. **59**, 1942 (1987)

[5] O Marti *et al.*, *Journal of Microscopy* **152**, 803 (1988)

[6] G. Meyer and N.M. Amer, *Appl. Phys. Lett* **56** 2100 (1990)

[7] S. Manne, P.K. Hansma, J. Massie, V.B. Elings and A.A. Gerwirth, *Science* **251**, 183 (1991)

[8] S. Fujisawa *et al*., *Nanotechnology* **4**, 138 (1993)

[9] J.B. Pethica and W.C. Oliver, *Phys. Scri.* T **19**, 61 (1987)

[10] F. Ohnesorge and G. Binnig, *Scienc*e **260**, 1451 (1993)

[11] H. Ueyama, M. Ohta, Y. Sugawara and S. Morita, *Jap. J. Appl. Phys*. **34**, L1086 (1995)

[12] Y. Sugawara, M. Ohta H. Ueyama and S. Morita, *Science* **270**, 1646 (1995)

[13] T. Minobe *et al*., *Appl. Surf. Sci*. **140**, 298 (1999)

[14] Ch. Loppacher *et al*., *Appl. Surf. Sci*. **140**, 287 (1999)

[15] S. Orisaka, T. Minobe, T. Uchihashi, Y. Sugawara and S. Morita, *Appl. Surf. Sci*. **140**, 243 (1999)

[16] K. Fukui, H. Onishi and Y. Iwasawa, *Appl. Surf. Sci*. **140**, 259 (1999)

[17] B. Cappella and G. Dietler, *Surf. Sci. Rep*. **34**, 1-104 (1999)

[18] H. Hölscher, U.D. Schwarz, O. Zwörner and R. Wiesendanger, *Phys. Rev. B* **57**, 2477-2481 (1998)

[19] F.J. Giessibl, *Mater. Today* **May 2005**, 32-41 (2005)

[20] F.J. Giessibl, *Science* **267**, 68-71 (1995)

[21] Giessibl, *Rev. Mod. Phys*. **75**, 949-983 (2003)

[22] A. Gibaud and S. Hazra, *Current Sience* **78 (12)**, 1467-1477 (2000)

[23] J. Als-Nielsen, *Elements of Modern X-Ray Physics,* Ed.New York (2001)

[24] Y. Martin and H.K. Wickramasinghe*, Appl. Phys. Lett*. **50**, 1455 (1987)

[25] U. Hartmann, Adv. Electr. *Electron Phys*. **87:49**, 200 (1994)

[26] U. Hartmann, *Phys. Lett. A* **137**, 475 (1989)

[27] M. Faraday, *Trans. Roy. Soc*. **5**, 592 (1846)

[28] Z. Qiu and S. Bader, *Journ.Mag.Mag.Mat.* **200**,664-678 (1999)

[29] Z. Qiu and S. Bader, *Rev. Sci. Instr*. **71 (3)**, 910-913 (2000)

[30] C. Maxwell, J. *A transite on Electricity Magnetism* **2**, 21 (1873)

[31] J. Kerr, *J. Philos. Mag*, **3**, 339 (1877)

[32] J. Kerr *J. Philos. Mag*, **5**,161 (1878)

[33] Z. Qiu and S. Bader, *MRS bulletin* **20**, 34 (1995)

[34] M Fronk, B. Bräuer, J. Kortus, O. G. Schmidt, D. R. T. Zahn and G. Salvan, *Phys. Rev. B* **79**, 235305 (2009)

[35] C.-Y. You and S.-C. Shin, *J. Appl. Phys*. **84**, 541 (1998)

[36] M. Grimsditch and P. Vavassori*, J. Phys. Cond. Matter* **16** R275 (2004)

[37] P. Vavassori, M. Grimsditch, V. Novosad, V. Metlushko and B. Ilic, *Phys. Rev. B* **67**, 134429 (2003)

[38] R. Schäfer, *Investigation of domains and dynamics of domain walls by the magneto-optical Kerr effect.* In Handbook of Magnetism and Advanced Magnetic Materials, ed. By H. Kronmüller and S. Parkin, Willey (2007)

[39] E. Nikulina, O. Idigoras, P. Vavassori, A. Chuvilin and A. Berger, *Appl. Phys. Lett.* **100**, 142401 (2012)

[40] E. Nikulina, O. Idigoras, J. M. Porro, P. Vavassori, A. Chuvilin and A. Berger, *Appl. Phys. Lett*. **103**, 123112 (2013)

[41] S. Foner, *Rev. Sci. Instrum*. **30 (7)**, 548-557 (1959)

5. Micromagnetic simulations

5.1. Micromagnetism and magnetization dynamics

In the micromagnetic approximation, the total energy of a ferromagnetic system is uniquely defined by its magnetization state. It is known that a magnetic system always tends to reach a minimum-energy state. This equilibrium state is represented by the minimum of the free energy. Given the free energy as:

$$F = U - T \cdot S \tag{5-1}$$

and differentiating Eq.(5-1), we have:

$$dF = dU - T \cdot dS - S \cdot dT \tag{5-2}$$

There are few assuptions in micromagnetism: to avoid thermally activated transitions the temperature is set to be zero, and entropy changes are neglected. With these statements, the second and third terms of the right-hand side of Eq.(5-2) give no contribution to the variation of the free energy. Therefore any variation of the free energy can be considered as the variation of the internal energy of the system. Hence, by minimizing the energy of the system by variational calculus the equilibrium states of a given micromagnetic system are found. Taking this into account, it is possible to determine static magnetization structures representing an equilibrium configuration by minimizing the energy of the system, known that energy considerations do not yield anything about the time evolution of the system. Starting from an initial equilibrium state, for a given external magnetic field the magnetization undergoes a complex dynamic process before finding another equilibrium state consequent to a field change. These processes occur on a timescale of pico and nanoseconds, and the fundamental equation to describe these magnetization dynamic processes is the Landau-Lifshitz-Gilbert (LLG) equation. Firstly, magnetic concepts as the

magnetization precession and effective field terms will be discussed, and then the definition of the LLG equation itself will be performed.

5.1.1. Magnetization precession and effective field terms

A magnetic moment $\vec{\mu}$ experiences a torque $\vec{T}$ in a magnetic field $\vec{H}$ given by:

$$\vec{T} = \vec{\mu} \times \vec{H} \tag{5-3}$$

$$\vec{T} = d\vec{L}/dt \tag{5-4}$$

As the torque is the change of angular momentum per unit time (Eq.(5-4)), and given that $\vec{L}$ is connected to $\vec{\mu}$ by the gyromagnetic ratio $\gamma_0 = -g|e|\mu_0/2m_e$ (μ_0 is the vacuum permeability, g is the Landé factor and m_e is the electron mass), it can be written:

$$d\vec{\mu}/dt = \gamma_0 \cdot \vec{\mu} \times \vec{H} \tag{5-5}$$

In Figure 5-1 the precession motion of $\vec{M}$ is represented.

$$d\vec{M}/dt = -\gamma_0 \cdot \vec{M} \times \vec{H} \tag{5-6}$$

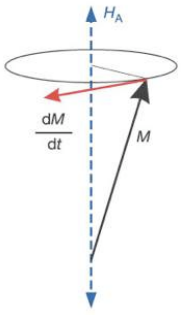

Figure 5-1: precessional motion of the magnetization in an external magnetic field.

The dynamic effect of a field $\vec{H}$ on the magnetization $\vec{M}$ is described by Eq.(5-6). Nevertheless, in a ferromagnet an external applied field is not the only source of a torque on the magnetization; the interactions occurring inside the ferromagnet such as those associated to exchange, magnetostatic and magnetocrystalline anisotropy energies also give rise to the application of torques on the magnetization. In order to compile all these internal effects, an effective field $\vec{H}_{eff}$ is defined as follows:

$$\mu_o \vec{H}_{eff} = -\frac{1}{M_s}\frac{\partial e}{\partial \vec{m}} \tag{5-7}$$

where e is the micromagnetic energy density and $\vec{m} = \vec{M}/M_s$. A more common form of the effective field, including all effects from external and internal sources of torque can be written as follows:

$$\vec{H}_{eff} = \frac{2A}{\mu_0 M_s}\Delta\vec{m} + \vec{H}_{ext} + \vec{H}_{stray} - \frac{1}{\mu_0 M_s}\frac{\delta e_K}{\delta \vec{m}} \tag{5-8}$$

This equation contains all the possible sources to the effective magnetic field acting on an elementary moment $d\vec{m}$ in a ferromagnet studied from the micromagnetics point of view. A more detailed derivation of Eq.(5-8) can be found in [1] and [2].

When looking for an expression for the precessional motion of the local magnetization around the local effective field, it can be obtained just by replacing the external field $\vec{H}_{ext}$ by the effective field $\vec{H}_{eff}$ in Eq.(5-6), noting that only the component of $\vec{H}_{eff}$ perpendicular to the magnetization will have an effect on the magnetization dynamics.

5.1.1.1. The Landau-Lifshitz equation

One could think that Eq.(5-6) represents a complete description of the magnetization dynamics. Nevertheless, if that were the case, a dynamic process once initiated would last forever because this equation does not contain any dissipation term. Given that the magnetization in a ferromagnet ends up being aligned with a strong enough externally applied magnetic field on a timescale of pico or nanoseconds (depending on the intensity of the magnetic field) there has to be some damping or friction in the magnetization dynamic process. Landau and Lifshitz introduced a phenomenological dissipation term describing those effects to the precessional motion. There are some constraints that must be considered in order to work out the dissipation term to be added to the equation of the precessional motion:

- The magnetization must be aligned with the effective field in the long time limit. In this limit, it must be satisfied that $d\vec{M}/dt = 0$.

- The magnitude of the magnetization must be preserved. This requirement comes from Eq.(5-6), from which $M_s = \left|\vec{M}\right|$, and is a basic requirement in the micromagnetics framework.

Taking into account that the damping term has to fulfill these two conditions, Landau and Lifshitz wrote the following one:

$$\frac{d\vec{M}}{dt} = -\frac{\eta}{M_s}\vec{M} \times (\vec{M} \times \vec{H}_{eff}) \qquad (5\text{-}9)$$

In this equation, η stands for the phenomenological damping coefficient introduced by Landau and Lifshitz. The Landau-Lifshitz equation for the magnetization dynamics is written as:

$$\frac{d\vec{M}}{dt} = \gamma_L(\vec{M} \times \vec{H}_{eff}) - \frac{\eta}{M_s}\vec{M} \times (\vec{M} \times \vec{H}_{eff}) \qquad (5\text{-}10)$$

5.1.1.2. The Gilbert equation

Gilbert derived a damping term for the magnetization dynamics in a different way than the one described in the previous section fulfilling the two conditions imposed for the dissipation term. This equation was derived later than the one of Landau and Lifshitz, but attracted much more attention than that one. The main aspect of the Gilbert equation is that the change of magnetization with the time appears in both sides of the equation in an implicit way:

$$\frac{d\vec{M}}{dt} = -\gamma(\vec{M} \times \vec{H}_{eff}) + \frac{\alpha}{M_s}\vec{M} \times (\vec{M} \times \frac{d\vec{M}}{dt}) \qquad (5\text{-}11)$$

In this case, α is the damping constant introduced by Gilbert, different than the one introduced by Landau and Lifshitz in Eq.(5-10) and is, in fact, the only dimensionless value used to describe the damping in the recent literature [3], whereas the Landau-Lifshitz damping constant is found in old literature [4].

From the physics point of view, the differences between the two damping constants lie in the nature of the damping. In the Landau-Lifshitz approach only the relaxation term is damped fulfilling the two previously explained constrains, whereas the Gilbert equation describes a situation of viscous damping; being the condition required for the damping term to fulfill the following: the damping is increased with an increasing 'magnetic velocity' $\left|d\vec{M}/dt\right|$.

5.1.1.3. The Landau-Lifshitz-Gilbert equation

The Landau-Lifshitz and Gilbert equations can be converted into each other. It is possible to rewrite Gilbert equation into the one of Landau and Lifshitz, revealing their equivalency from the mathematical point of view. When the

Gilbert equation is rewritten into an explicit form, it assumes precisely the form of the Landau-Lifshitz equation, and the equation is known as the Landau-Lifshitz-Gilbert (LLG) equation:

$$\frac{d\vec{M}}{dt} = -\frac{\gamma}{1+\alpha^2}(\vec{M}\times\vec{H}_{eff}) - \frac{\alpha\gamma}{M_s(1+\alpha^2)}\left[\vec{M}\times(\vec{M}\times\vec{H}_{eff})\right] \qquad (5\text{-}12)$$

The connection between Landau-Lifshitz and Gilbert equations is given by two expressions relating the damping coefficients and factors of the precession terms:

$$\gamma_L = \frac{\gamma_G}{1+\alpha^2} \qquad (5\text{-}13)$$

$$\eta = \frac{\alpha\gamma}{M_S(1+\alpha^2)} \qquad (5\text{-}14)$$

Usually, analytic solutions of LLG equation are only obtained when the magnetic structure of the sample is assumed to be homogeneous throughout the reversal process in what is called the macrospin approximation [5]. This approximation is valid only for very special cases, like particles up to 10nm size [6]. In inhomogeneous and 3-dimensional magnetic structures the LLG equation is integrated in time by applying numerical methods to obtain possible solutions.

5.2. Object Oriented MicroMagnetic Framework (OOMMF) program

All the simulations of the magnetization behavior in the samples under experimental investigation in this thesis have been performed by making use of a micromagnetism simulation code, which has been developed by the Mathematical and Computational Sciences Division (MCSD) of the Information Technology Laboratory at the National Institute of Standards and Technology (ITL/NIST), in close cooperation with the Micromagnetic Modelling Activity Group (μMAG).

This code, named Object Oriented MicroMagnetic Framework, widely known by its acronym OOMMF, is a powerful tool to simulate magnetization dynamics processes in micromagnetic systems and to find equilibrium configurations of the magnetization. It solves the LLG equation by relaxing three-dimensional spins on a bi- or tri-dimensional mesh of cubic cells. The most complicated problem is the computation of the self-magnetostatic field, which has a very complicated space distribution inside any confined structure with a shape different from an ellipsoid of rotation (being in this case uniform). The micromagnetics solver finds the equilibrium configuration at each field step given an initial magnetization distribution and a sequence of field steps. The desired shape of the magnetic material to be simulated is provided through a .bmp image.

The basic inputs of the program are:

- Material parameters:
    - Saturation magnetization (A/m)
    - Exchange stiffness (J/m)
    - Magnetocrystalline anisotropy constant (J/m^3)
    - Damping coefficient (0 – 1)
    - Anisotropy type (uniaxial, cubic)
    - First and second anisotropy axis (for cubic only)
- Geometry of the sample to be studied and discretization
    - Width, height and thickness
    - Unit cell size (for the calculations)
    - Image import (.bmp) with the desired shape
- Initial magnetization: uniform, single-domain, multidomain, vortex, and arbitrary.

- Field ranges for the simulation: it allows multiple field-step simulations, with different field-step sizes.

- Convergence $\left|\vec{M}\times\vec{H}\right|$ value: this is the torque value to use as stopping criteria. When $\left|\vec{M}\times\vec{H}\right|$ is smaller than this value for all cells in the simulation it is assumed that an equilibrium state has been reached for the current applied field.

The outputs of the program are:

- Vectorial maps of the magnetization and of the total and demagnetizing magnetic fields.

- Relevant parameters provided at each field step:

    - Calculation parameters: number of iterations, field updates, simulation time (ns) and time step (ns).
    - Magnitudes of the total magnetic field and of each of its components (mT).
    - Normalized total magnetization and normalized components of the magnetization.
    - Energy densities: total, exchange, anisotropy, demag and Zeeman energy densities are computed.
    - Maximum angle between the magnetization orientation of any pair of neighboring spins.

- 2D plots of the desired magnetization components and/or magnetic field components.

This micromagnetic simulations code is widely used by the scientific community, and simulations of the behavior of the magnetization in magnetic structures obeying the laws of micromagnetism are present in many papers [7, 8].

5.3. References

[1] W.F. Brown, Jr., Magnetostatic Principles in Ferromagnetism (Oxford Science publications, Clarendon Press, Oxford 1996)

[2] W.F. Brown, Jr., Micromagnetics (Interscience Publishers, John Wiley & Sons, New York, London, 1963)

[3] Z. Frait and H. MacFaden, *Phys. Rev*. **139**, A1173–A1181 (1965)

[4] R. Yilgin *et al.*, *IEEE Trans. Magn.* **41**(10), 2799 – 2801 (2005)

[5] R. Kikuchi, *J.Appl.Phys.* **27**, 1352 (1956)

[6] W. Wernsdorfer *et al.*, *Phys.Rev.Lett*. **78**, 1791 (1997)

[7] B. Van Waeyenberge *et al.*, *Nature* **444**, 461-464 (2006).

[8] A. Wachowiak *et al., Science* **298**, 577-580 (2002).

6. Asymmetric magnetic dipolar interactions

6.1. Introduction

6.1.1. Dipolar interactions in magnetic devices

The phenomenon of hysteresis is complex, nonlinear, nonequilibrium and nonlocal. In small nanoparticles it reflects the existence of anisotropy-related metastable energy minima separated by field-dependent energy barriers. The energy needed to overcome these barriers depends on the intrinsic anisotropy of the magnetic material, the volume and the shape (which contributes to the shape magnetic anisotropy) of the magnetic nanostructure.

The hysteresis loop shape of a magnetic nanoparticle is determined by the properties of the magnetic material: intrinsic anisotropy, exchange, magnetization saturation, size and shape. Besides these, when a sample is composed by interacting ferromagnetic nanoelements also the interactions between the elements in the array affect the hysteresis loop shape. The reversal path followed by the magnetic sample is not only defined by the applied exernal field and the thermal fluctuations; as an example, dipolar interactions between neighboring nanoelements of an array of ferromagnetic nanoislands also affect the magnetization reversal path.

There are fundamental hysteresis related physical issues that have become the focus of extensive studies over the past two decades by studying quasi one dimensional structures such as nanowires, nanorods and nanotubes, which have a wide variety of potential applications such as sensors [1], computing elements [2], photovoltaic [3], magnetic memories [4] and spintronics technology [5]. The understanding and precise control of the magnetization behavior of nano-sized magnets remains a key issue in fundamental physics and various technological applications. Thanks to the advancements of nanofabrication technologies,

nanomagnets are now providing an excellent experimental laboratory for testing fundamental theorems in magnetostatics and micromagnetics. When a nanomagnet is immersed in an externally applied field, spatially uniform over the length scale of the nanomagnet, a wide variety of field-induced behaviors are observed, both experimentally and using micromagnetic simulations. These behaviors include reversal via vortex nucleation and annihilation [6], domain wall nucleation and motion [7], and coherent rotation [8], and this variety reflects the complexity of the hysteresis phenomena anticipated above. The enormous knowledge accumulated so far demonstrates that the sequence of stable and meta-stable states through which a nanomagnet evolves during the field induced remagnetization process, depends on and can be controlled by size, shape (including defects), material parameters and field history.

The common situation that occurs in experiments involving nanomagnets is that their magnetization evolves under the action of a uniform (in the sense discussed above) applied field. In this case a nanomagnet can only explore a limited region of the energy landscape that its geometry and material properties determine, even if there are other possible reversal paths with metastable (stable magnetization states in non-zero field) and stable (zero field) magnetization states that cannot be explored under the solely action of a uniform externally applied field. This is not so relevant when nanomagnets are used in conventional applications such as hard disk drives [9] and magnetic random access memories [4], where the nanomagnets are required to possess controlled magnetic properties to ensure that each element can be set into a stable single domain with uniform magnetization along two opposite directions; this is the so-called Ising-like behavior. This bistable magnetization behavior is ensured when the nanoislands are not interacting through their dipolar fields; therefore for the above mentioned applications of nanomagnets the challenge is generally to avoid magnetic dipolar interactions between the individual elements in patterned arrays.

Nevertheless recent works showed that it is possible to take advantage of the dipolar interactions occurring between neighboring nanomagnets subjected to

each other's dipolar fields, and to exploit them for providing interconnectivity in networks of closely-spaced, dipole-coupled, single-domain nanomagnets. One example consists of networks of dipole-coupled nanomagnets designed to perform signal processing tasks, as well as digital computation in nanomagnets logic devices [10, 11]. Nanomagnet logic devices might have promising applications in the future, including intelligent magnetic field sensors, processing-in-memory-type architectures, or even a complex signal-processing unit, based entirely on magnetic field coupling. From a more fundamental physics point of view, interacting single domain Ising-like objects can be arranged to create model systems to study fundamental aspects of competing interactions [12] as is the case of the so-called artificial spin-ice structures, based on specific arrangements of Ising-like single domain nanomagnets that are designed to produce frustration. In such systems, the study of the accommodation of frustration through local correlations between magnetic moments has been carried out as a function of the interaction strength and the specific geometric arrangement. This application of ferromagnetic nanoislands, the study of the accommodation of magnetic frustration in arrays of Ising-like bistable nanomagnets, will be focus of study in the next chapter of this thesis.

In all these applications of interacting nanomagnets the shape related magnetic self-energy, also called shape anisotropy, forces the magnetic moments of elongated islands (nanomagnets) to align along their long axis, thus making the magnetic behavior of each island Ising-like, viz. bistable. Furthermore it is also assumed that the true magnetostatic interaction does not substantially alter the Ising-like behavior of each island, which can be considered equivalent to a point dipole. This is a very crude approximation that neglects a crucial aspect of the physics involved: the dipolar near-field coupling between adjacent islands is not uniform over the whole island and it might not be spatially symmetric.

In this study, it is shown that the non uniform distribution of the dipolar interaction field can induce formation of non-uniform magnetic configurations during system remagnetization even in magnetic nanoislands that are only stable in the single domain state when isolated, thus leading to a breakdown of the

basic assumption of Ising-like behavior [13]. Furthermore, it is also demonstrated that this breakdown is an example of a more general physical concept determining the physics of systems with magnetic dipolar interactions that involves the spin dynamic properties of each nanomagnet well above the onset of magnetization reversal. This analysis, on a broader view, allows the study of the effects of non-uniform magnetic fields on the magnetization reversal process of ferromagnetic nanoislands, opening magnetization reversal pathways that were not possible to explore under the action of a uniform magnetic field.

6.1.2. Magnetization states energy landscapes

As already mentioned, nowadays elongated ferromagnetic nanoislands are the base of many important components of promising devices with different applications. For the majority of these applications it is a requirement that the nanomagnets composing the device, both in the case they are interacting through their dipolar fields as well as in the case where they do not interact, stay in the single domain state: all their spins must lie (almost) parallel to the long axis of the nanoelement. Nevertheless this magnetization state is not the only one that can be observed stable at remanence; depending on the dimensions of the nanoislands and on the field history applied to the nanoislands a magnetic vortex state (or more complicated magnetization patterns: non uniform magnetization states in general) can also be observed, in principle, under certain conditions that will be discussed later on this chapter.

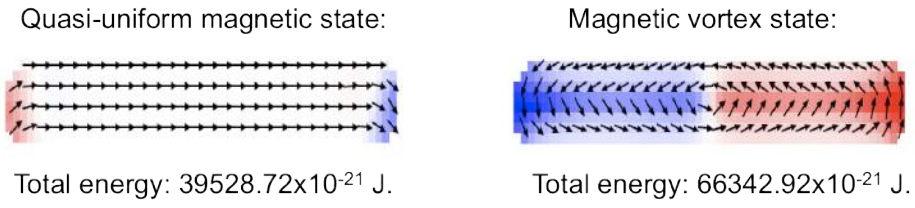

Figure 6-1: Quasi-uniform versus vortex state energies in a 700x160x25nm Permalloy nanoisland.

In Figure 6-1 a single-domain uniform magnetization state and a vortex state are sketched. Depending on the sizes and aspect ratios of the nanomagnets one of

these magnetic states will be more favorable than the other; this is what will be discussed now. The vortex state configuration consists of a curling of magnetic spins where a magnetization singularity is present at the center of the vortex. The magnetization is lying in the plane of the particle everywhere but in a small region around the vortex singularity, where the magnetization is twisted out of plane. The vortex state has very small net magnetic moment. On the contrary, the single domain configuration has a quasi-uniform magnetization state with an average magnetization that is in the range of 0.97-0.99M_S, as all the spins are almost parallel to the long axes of the nanoislands. The nanomagnets studied here are made of Permalloy, which is a Nickel (81%) Iron (19%) alloy that has a magnetization saturation value of $M=865x10^3$ A/m, exchange stiffness constant $A=13x10^{-12}$ J/m^3 and negligible magnetic anisotropy. Due to the fact that this magnetic material has extremely low intrinsic magnetic anisotropy, the only magnetic energy terms competing in minimizing the total energy of the nanomagnet are the exchange energy and the demagnetization energy (in the absence of any external field).

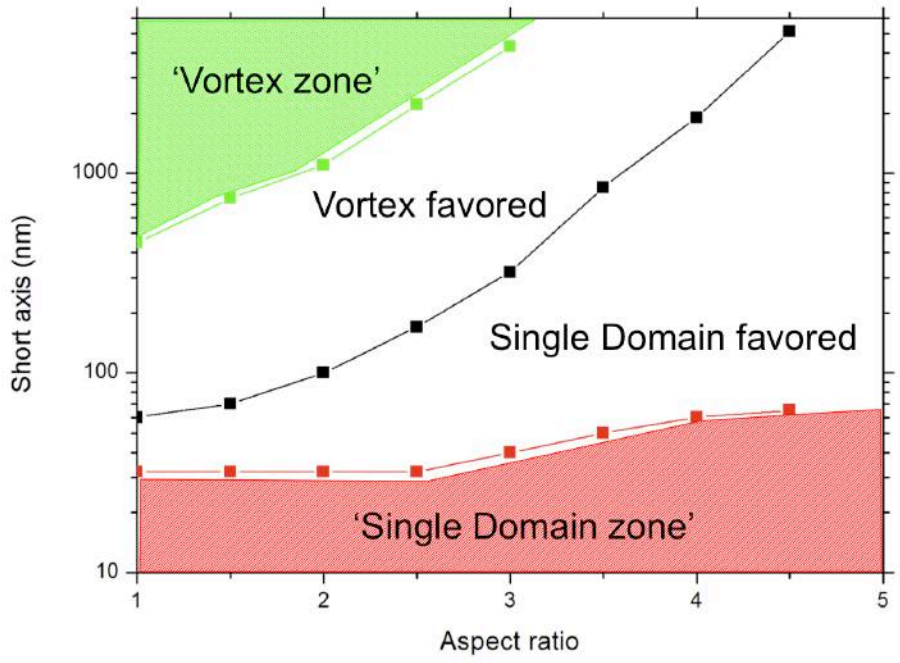

Figure 6-2: Short axis (nm, logarithmic scale) versus aspect ratio plot showing the energetically stable regions for single-domain and vortex states in 25nm thick Py nanoislands. In the green region only vortex states can be found, whereas in the red region only quasi-uniform magnetization states can be found. In the white region both vortex and quasi-uniform magnetization states can be found, being the vortex less energetic above the black curve, whereas the quasi-uniform is less energetic below the black curve.

Based on micromagnetic simulations performed by means of the OOMMF micromagnetics simulation program [14], and using the magnetic parameters expressed above for Permalloy, with a unit cell of 5nm (smaller than the exchange length for Permalloy, that is 5.3nm) a diagram showing the single domain versus vortex magnetic states' energy stability regions has been obtained and can be observed in Figure 6-2. In this diagram the thickness of the analysed nanoislands is 25nm, and the lateral dimensions change ranging from aspect ratios $1 \leq {}^{L_Y}/_{L_X} \leq 4.5$. In that plot three different regions (according to the background color) are distinguished: the green region, marked by the green curve, in which the single-domain state is not found at remanence, the red region marked by the red curve, where the magnetic vortex state cannot be found (only single-domain state is found in that region), and the white region, where both single-state and vortex magnetization states are stable at remanence. The meaning of the black curve in the plot is that in the white region below the curve the quasi-uniform single domain magnetization state has lower total energy than the vortex magnetization state, whereas above the curve the vortex magnetization state is the less energetic one. Nevertheless, for lateral sizes in which a single domain magnetic state is the less energetic one a magnetic vortex state can be found stable in the nanomagnet (and viceversa; i.e. a single domain state can be stable in for lateral sizes in which the less energetic magnetic state is a vortex) depending on the intensity and uniformity of the applied field history of the nanomagnet [15].

Under the action of a uniform magnetic field, the behavior of the magnetization on the nanoislands is summarized in Figure 6-3. In that figure, superimposed to the energy stability regions for the magnetization states in the nanoislands given by Figure 6-2, two different regions are observed separated by a dashed line: above that line (green region), non-uniform magnetization states can be found at remanence after the action of a uniform external field; nevertheless, below the dashed line (red region) it is not possible to find a non-uniform magnetization state in the nanoislands under the action of a uniform external field.

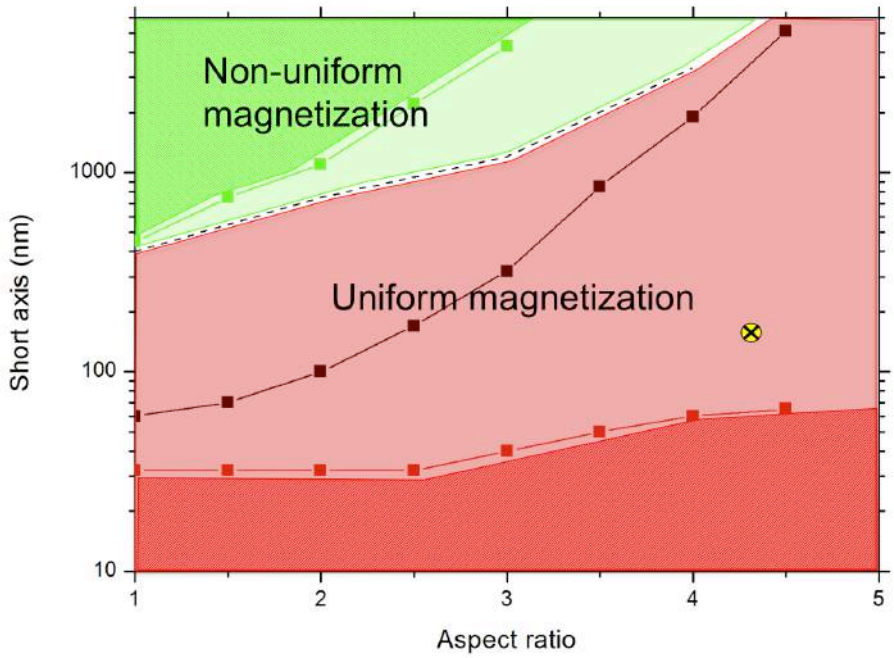

Figure 6-3: Magnetization states in nanomagnets under the action of a uniform magnetic field. The green region above the dashed line denotes sizes for which a non-uniform magnetic state can be found at remanence after the application of a uniform external field, whereas the red region below the dashed line denotes sizes for which a non-uniform magnetic state is prohibited under the action of a uniform external field. The yellow dot denotes the size of nanoislands for which a non-uniform magnetic state has been induced under the action of asymmetric field sources.

In this work it will be shown that the action of a non-uniform magnetic field provided by means of dipolar interactions between nanomagnets, which is otherwise impossible to achieve in the nanometer scale, can lead to a substantial modification of the magnetization reversal path. The yellow dot with a cross inside in the Figure 6-3 shows a size of nanomagnets in which a vortex state has been induced and found stable at remanence, as will be discussed later. The reversal takes place via the nucleation of magnetic vortex states in nanoislands with aspect ratios higher than 4, which can be trapped stable and consistently at remanence [13], in a process that will be explained in the next section.

6.2. Description of the experiment

In this experiment the magnetization reversal process of interacting elongated ferromagnetic nanoislands is investigated by means of magneto-optical Kerr

effect magnetometry, analyzing the reflected and diffracted beams from the sample, magnetic force microscopy (MFM) images and micromagnetic simulations. The nanoislands are arranged in chiral square units forming a checkerboard array, as observed in Figure 6-4. The purpose of the geometry of the sample is to provide sources of asymmetric field distributed over the nanoislands forming the array, so that each nanoisland composing the square unit (4 nanoislands), and therefore every nanoisland in the array, is subjected to an asymmetric and non-uniform dipolar field given by its two nearest neighboring nanoislands. Different nanoisland sizes have been investigated, ranging from 525 nm long and 120 nm wide to 1400 nm long and 160 nm wide, having aspect ratios from 4.375 to 8.75, and thicknesses of 25 and 40 nm. The nanomagnets are made of Permalloy, and the arrays of nanomagnets have been fabricated by means of patterning using electron-beam lithography and lift-off processes combined with electron beam evaporation for the deposition of the metal, as described in Chapter 3 of this thesis.

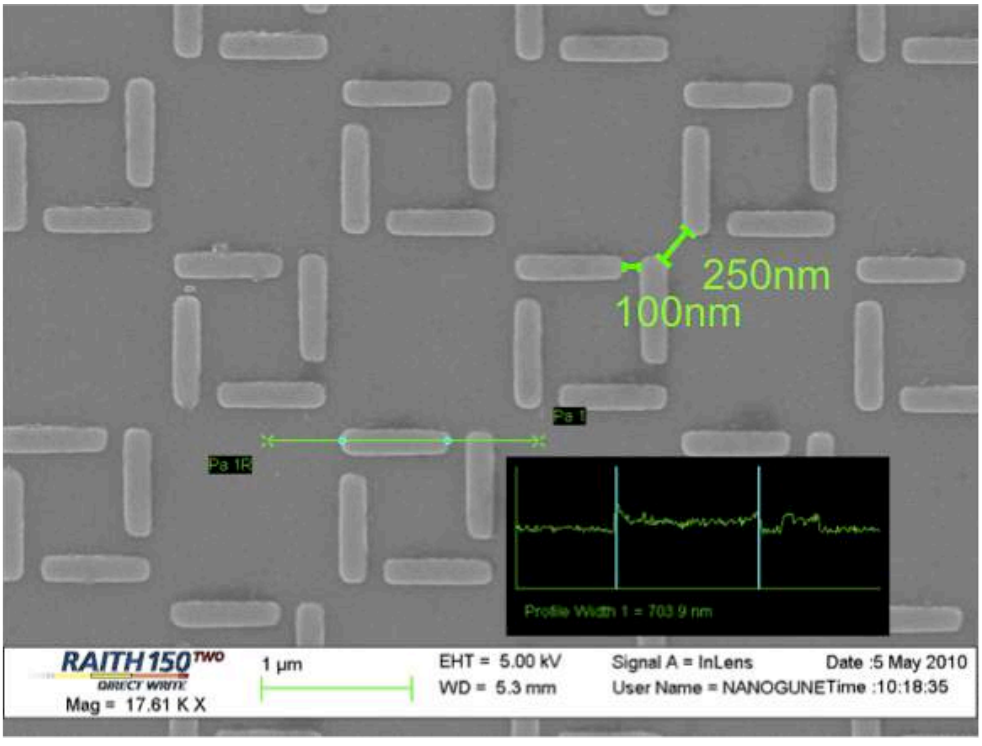

Figure 6-4: First sample studied of interacting ferromagnetic nanoislands with sizes 700x160x25nm.

6.2.1. Angular dependence on the magnetization reversal

The first sample analyzed is formed by nanoislands with the following dimensions: 700nm long, 160nm wide and 25nm thick, and gaps between neighboring nanoislands of 100nm. The square unit (formed by four nanoislands) corner to corner separation is 250nm, so that dipolar interactions between nanomagnets belonging to different square units are clearly weaker and do not affect the magnetization reversal process of each individual square unit. As already stated previously, the magnetization reversal process has been analyzed by means of MOKE magnetometry, measuring the changes on the intensity and polarization of the reflected and diffracted beams upon reflection from the sample. Hysteresis loops from the reflected beam in the conventional longitudinal [16] configuration have been measured, together with loops from different diffracted beams in the transverse configuration [17] while applying the external magnetic field from positive to negative saturation at different angles from the edge orientation of a nanoelement.

Diffracted-MOKE hysteresis loops have been obtained from several diffraction orders, but only the second order loops are discussed since they were the most sensitive to the details of the magnetization reversal. By examining the hysteresis loops obtained at different angles it is easily deducible that two completely different magnetization reversal paths are followed by the magnetization of the nanoislands whose easy axis is (almost) perpendicular to the external field, depending on the orientation of the applied field: if the external field is applied at an angle above 2.5^0 from the edge of the square unit the reversal path differs from what is observed when the field is applied below that angle. These reversal paths have been named ‘misaligned’ and ‘aligned’ cases, respectively, and the representative hysteresis loops recorded from the reflected and second-order diffracted beams can be observed in Figure 6-5.

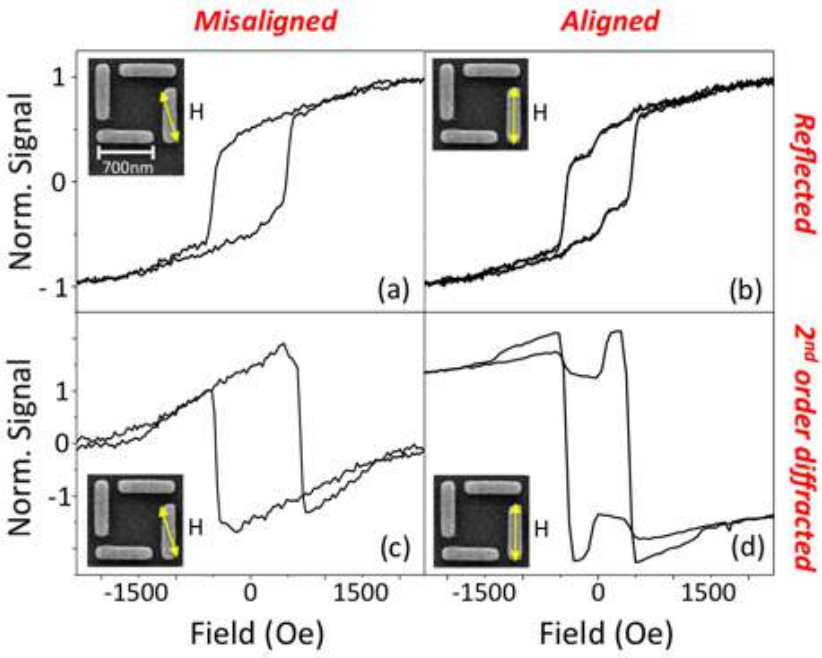

Figure 6-5: Measured hysteresis loops from the reflected (a, b) and second order diffracted (c, d) beams in the misaligned and aligned cases, with insets showing a SEM image of the unit square and the direction of the applied field.

By directly comparing the hysteresis loops from the reflected beam in the misaligned and aligned cases (Figure 6-5 (a) and (b)) it is already possible to infer that a different reversal process is occurring in each cases. The differences in the loops become dramatic when comparing loops recorded from the second-order diffracted beams (Figure 6-5 (c) and (d)), reason why the discussion of the reversal path will be mainly focused on the D-MOKE loops.

The two magnetization reversal pathways have been modeled by means of micromagnetic simulations, which have been performed utilizing the Object Oriented Micro Magnetic framework (OOMMF) platform provided by NIST [14], with the material parameters used for the simulations being those contained in the OOMMF program for Permalloy. In order to keep the computational time reasonable a unit cell size of 10nm has been used, which is bigger than the exchange length of Permalloy for the material parameters used in the simulations. The use of this rather large unit cell does not affect the results of the simulations, verified by calculating a few selected configurations of the reversal process with a cell size of 5nm, below the exchange length value. Using the micromagnetic simulations code it is possible to compute the magnetization

states $m(x, y, H)$, and the MOKE loop from any diffracted beam (including n=0, which is the reflected beam) can be obtained by calculating the magnetic form factor, as explained in Chapter.4 when discussing the diffracted-MOKE technique. The calculated hysteresis loops obtained in this way for the misaligned and aligned cases, both from the reflected and second-order diffracted beams, can be observed in Figure 6-6.

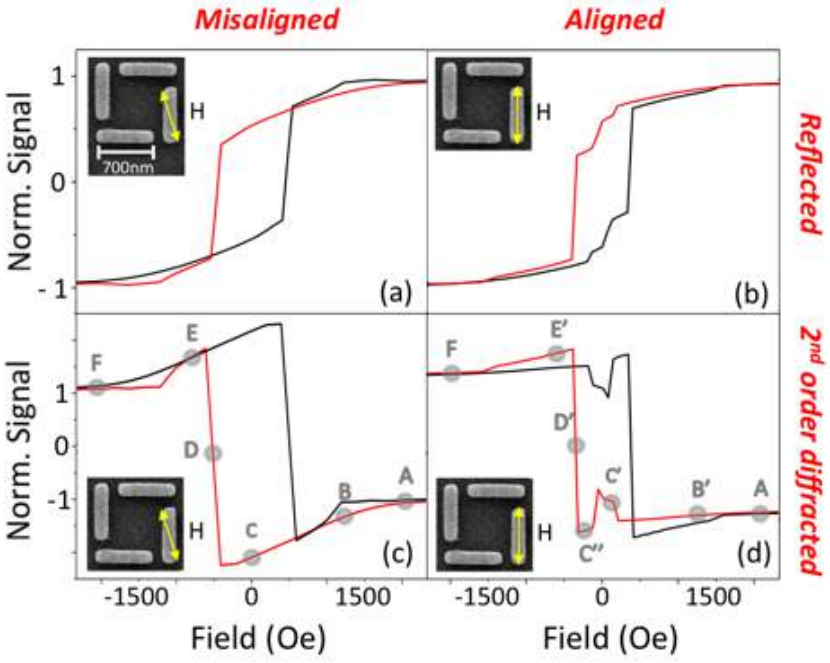

Figure 6-6: Calculated hysteresis loops from the reflected (a, b) and second order diffracted (c, d) beams in the misaligned and aligned cases. The positions marked in the diffracted hysteresis loops correspond to the magnetization states shown in Figure 6-7.

The agreement between the experimental and calculated loops is remarkable, as all the features of the experimental loops are reproduced in great detail by the calculated ones as observed by directly comparing Figure 6-5 and Figure 6-6; nevertheless the field values at which the various features appear are slightly different in the simulations, but this is not surprising considering that the simulations are performed using particles having a perfect shape and without thermal excitations. Having established the reliability of the micromagnetic simulations by its excellent correspondence to the experimental observations, it is licit to use the computed magnetization configurations to analyze the magnetization reversal of each nanomagnet in detail.

The relevant micromagnetic configurations computed for the two cases, aligned and misaligned, are shown in Figure 6-7. As observed, starting from positive saturation (H=2.3kOe) where the magnetic configuration is substantially the same for both cases, the magnetization reversal follows two completely different routes after reducing the field, as observed by comparison of magnetic configurations B and B' at H=1.3kOe, which are the first differentiated magnetization states for each magnetization reversal pathway, and that will evolve to configurations E and E', respectively. In the misaligned case a seed 'S' state is formed in the horizontal nanomagnets (B), and while reducing the external field towards zero applied field the 'S' state rotates until all the nanomagnets are in the single domain state (configuration C). The magnetization reversal process continues towards negative saturation field values passing through configurations D, E and F. In this magnetization reversal process all the nanomagnets in the square unit remain in a nearly uniform, single domain state during the magnetization reversal process, hereby giving rise to a sequence of configurations for the entire square unit cell that resembles the so-called 'onion state' (configuration C), 'horse-shoe state' (configuration D) and 'reversed onion state (configuration E) observed in closed square ring structures [17].

The formation of the horse-shoe state is due to the fact that the nanomagnets are not perfectly identical, so that the two vertical islands switch at a slightly different field value. This fact, which happens in the real sample due to the intrinsic nanofabrication defects, has to be implemented manually in the micromagnetic simulations. To do so, one of the nanoislands whose easy axis is (almost) parallel to the applied field is 15nm wider than the other one in the cell unit, so that their switching fields will be different and the magnetization states D and D' are found.

These findings demonstrate that dipolar interactions are not relevant enough to cause a deviation from the anticipated single domain rotation process in this case and the reversal is governed by the shape anisotropy of the individual nanomagnets.

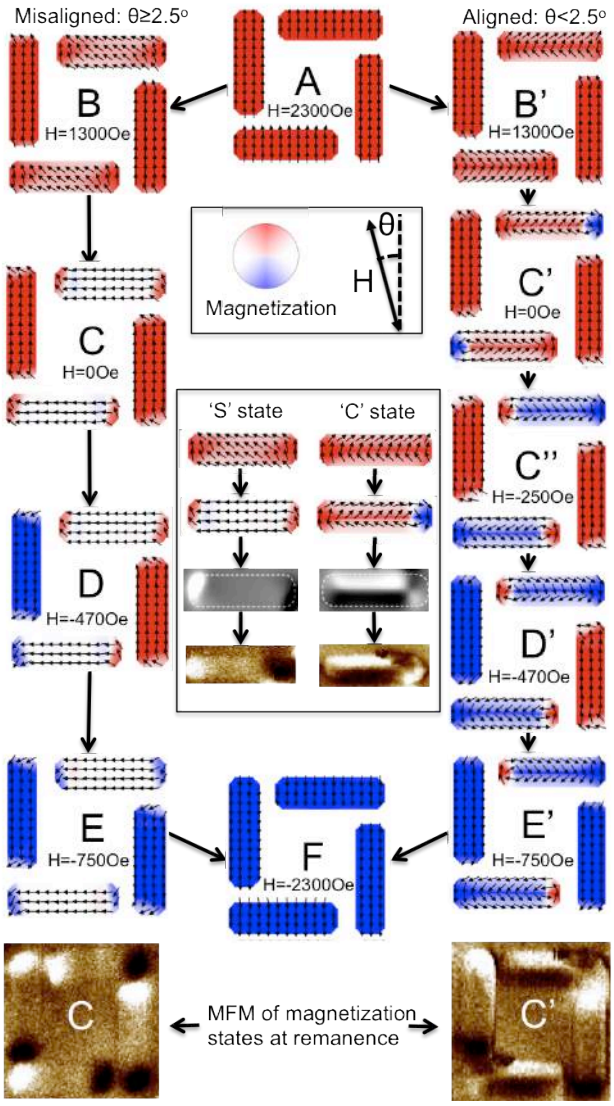

Figure 6-7: Micromagnetic simulations of the magnetization states in the reversal process for the misaligned and aligned cases. Inset 1: sketches indicating the external field direction and the magnetization directions. Inset 2: differences in magnetization on the bars perpendicular to the applied field (seed 'S' and 'C' states), with calculated (grey scale) and measured (color) MFM images of the remanent states showing single domain (misaligned) and vortex (aligned) magnetic states. Lower inset: MFM images obtained at remanence for the misaligned (C) and aligned (C') cases.

The magnetization reversal process of the horizontal (perpendicular to the external field) nanoislands is completely different from this one in the aligned case, where the different loop shapes with respect to the misaligned case reveals that dipolar interactions are able to overcome the effect of the shape anisotropy and induce a seed 'C' state (configuration B') into each of the the individual nanomagnets whose long axis is almost perpendicular to the external applied field (horizontal nanomagnets in Figure 6-7) rather than a 'S' state as the external field is reduced from positive saturation. The 'C' state subsequently

nucleates a single vortex magnetic state in each of the horizontal elements as the external field is reduced towards zero field (configuration C'). Interestingly, in the remanent configuration the two vortices are distorted with their cores displaced from the central position of each nanomagnet in order to reduce the magnetostatic energy due to the stray field produced by the vertical nanomagnets. As the external field is decreased towards negative saturation values the vortex cores are displaced horizontally towards the opposite end of each horizontal nanomagnet (configuration C''). The vortex cores displacements produce the notable peaks in the hysteresis loops recorded and calculated from the second-order diffracted beam.

These vortex cores displacements are reversible processes, as verified by relaxing the external field to zero from the value corresponding to the peak positions in the loops and observing that the diffracted-MOKE signal retraces itself.

By decreasing further the external field the two vertical nanomagnets reverse their magnetization one at a time (configurations D' and E') as in the aligned case. At a negative field of H=-1.4kOe the vortices in the horizontal nanomagnets eventually annihilate. It is noticeable that the vortices in the horizontal nanomagnets have opposite chirality, which is predetermined by the chirality of the square unit structure and the direction of the applied field. This is due to the fact that each vertical (almost parallel to the external field) nanoisland creates a dipolar field that acts differently in the horizontal bars (where the vortex are created): looking at the unit squares in Figure 6-7 the left vertical bar's dipolar field acts stronger in the bottom horizontal nanoisland, whereas it acts weaker in the top horizontal nanoisland, contrary to what happens with the right vertical bar's dipolar fields. This forces the vortex to be created at opposite edges in each horizontal nanoisland of the square unit, and the chirality is in this way preserved throughout the whole magnetization reversal process.

Confirmation of the reversal processes described above was obtained using magnetic force microscopy studies of the remanent states in both the misaligned

and aligned cases, as observed in the lower inset of Figure 6-7. This MFM imaging process was performed guided by the diffracted-MOKE loops following the approach used in [18], which allows to quench to zero-field desired intermediate metastable states in the nanomagnets by suitably choosing the field history, leaving the magnetic states ready to image through MFM. The MFM lower inset in Figure 6-7 clearly exhibit the magnetization patterns of states C and C'. Furthermore, in Figure 6-8 a MFM image of the remanent state after the vertical bars have reversed their magnetization (relaxing the magnetic state by removing the external field) is shown, where the horizontal bars present a centered magnetic vortex state, which is not pinned to the edges of the bars as in C' due to the lack of existence of the pinning dipolar field coming from the neighboring vertical nanoisland, as they have already reversed their magnetization.

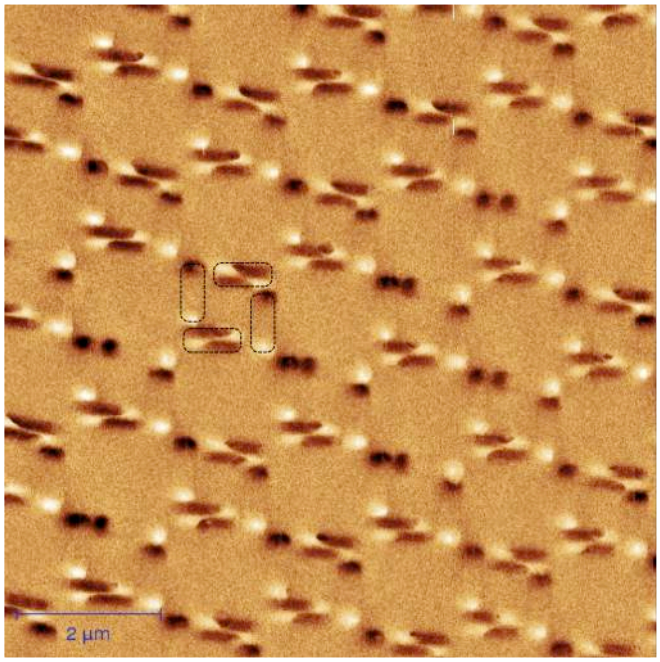

Figure 6-8: MFM image of the remanent magnetization state in the aligned case after the vertical bars have reversed their magnetization, showing a centered vortex state in the horizontal bars.

It is worth noting that the dramatic difference in the diffracted-MOKE hysteresis loops between the aligned and misaligned cases is due to a different magnetization reversal path in the horizontal nanomagnets, even if their contribution to the total vertical magnetic moment in each unit square (formed by four nanoislands) is much smaller than that of the vertical nanomagnets, and

the diffracted-MOKE loops are measured in the transverse MOKE configuration, sensible to the vertical component of the magnetization.

6.2.2. Dipolar stray fields and dynamics of the magnetization reversal

In order to understand why the magnetization reversal is accomplished in two completely different ways depending on the orientation of the external field, the vector map of the magnetic stray field created by the vertical nanomagnets (parallel to the external field) has been computed when the nanomagnets are in their saturated state (viz., at vertical H_{ext}>1000 Oe).

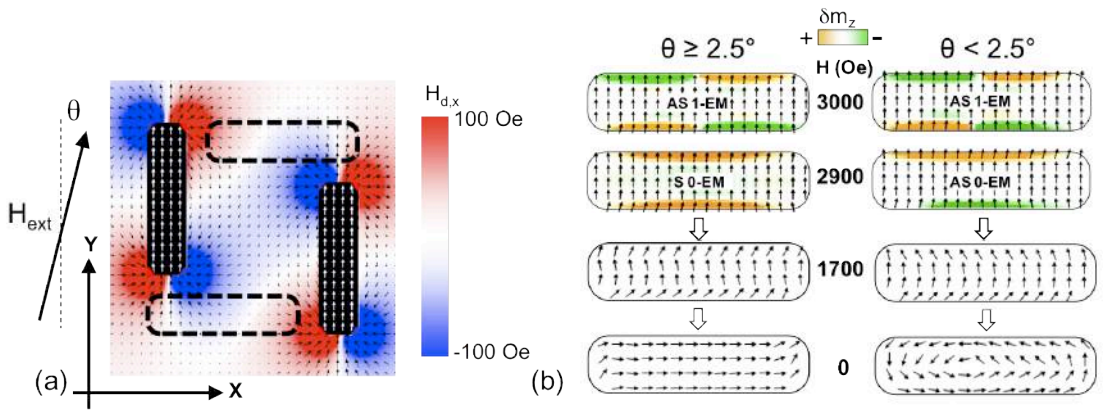

Figure 6-9: (a) Vector and intensity map of the dipolar stray field produced by the uniformly magnetized vertical nanomagnets. (b) Snapshots of the out of plane component of the precessing magnetization δm_z of the lowest frequency spin wave modes in the horizontal nanoisland at the indicated applied external fields (orange and green indicate positive and negative δm_z at a given time).

The resulting vector plot is displayed in Figure 6-9(a), where the contribution of the externally applied field has been removed and the only component of the total field plotted is the weaker dipolar stray field created by the vertical nanomagnets. In this figure the contour plot of the horizontal component of the dipolar stray field, H^d_x, is superimposed to the vector plot in a red-blue color scale for clarity, and it shows that the horizontal nanomagnets (whose long axis is perpendicular to the externally applied field) are subjected to an asymmetric and inhomogeneous dipolar stray field, whose maximum values are on the order of 100 Oe. In particular, H^d_x has opposite sign in the bottom and top halves of the horizontal nanomagnet, and it is precisely this asymmetry of the dipolar stray

field that could explain the formation of the vortex state since it might be enough to produce a canting in opposite directions of the spins at both top-left and bottom-down edges of the upper horizontal nanomagnet (the same happens for the lower horizontal nanomagnet, but let's focus on the upper one for simplicity).

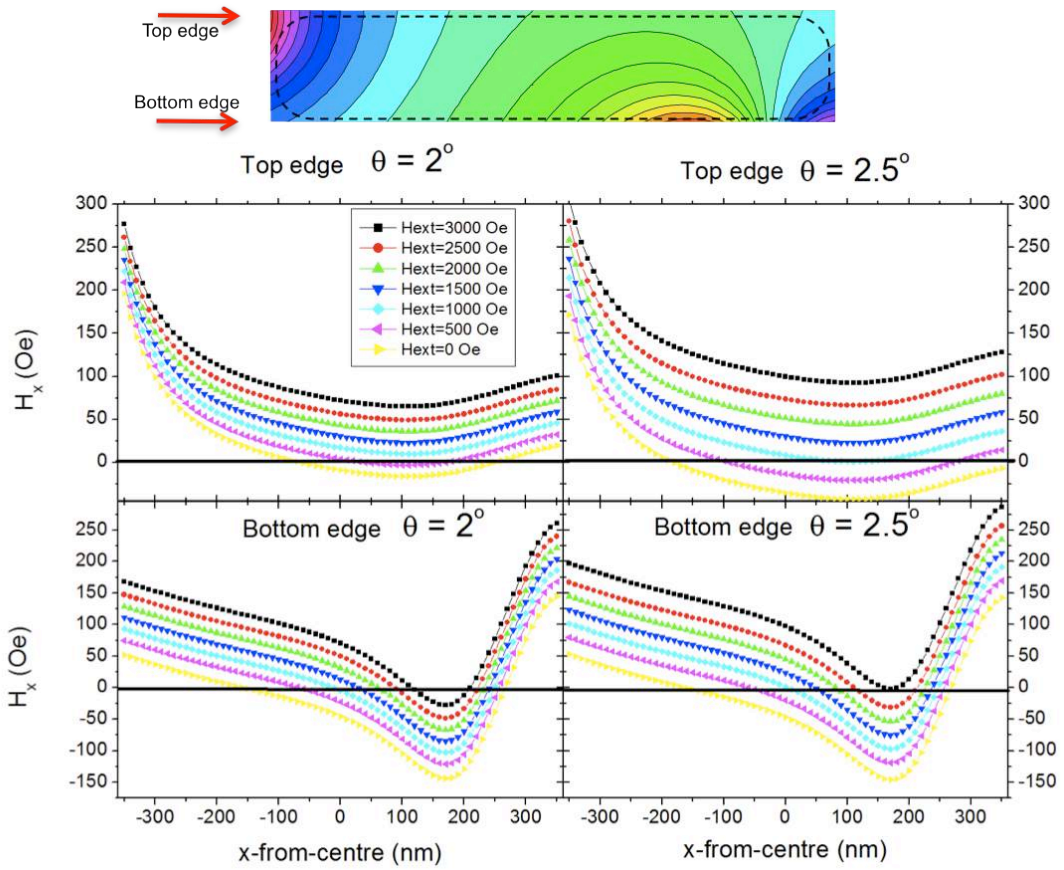

Figure 6-10: spatial distribution of the horizontal component of the total magnetic field acting on the top and bottom edges of the horizontal nanomagnets when the external field is applied at 2º (aligned case) and 2.5 º (misaligned case) for different values of the externally applied field.

The asymmetry of the dipolar fields acting on the horizontal nanoislands does not explain by itself the different behavior for the misaligned and aligned cases, as in both cases the inhomogeneities of these dipolar fields are present. The spatial distribution of the horizontal component of the total field (external+dipolar) acting on the top and bottom edges of the horizontal nanomagnets can be observed in Figure 6-10. Depending on the applied field, the asymmetry on the horizontal component of the total field appears in both the aligned and misaligned case: looking at external fields fields below 3000 Oe, in both cases there is a negative value of the horizontal component of the total field.

The dynamics come into play here, when analyzing which magnetization reversal pathway is chosen, together with the spatial distribution of the total magnetic field acting on the horizontal nanoislands.

For an external field of 1700 Oe it is already noticeable that in the aligned case a 'C' state (seed state leading to a magnetic vortex nucleation upon reduction of the external field) appears whereas in the misaligned case a 'S' state is nucleated, as shown in the bottom of Figure 6-9(b). Interestingly, the general physical picture that emerges after looking at the dynamics of the magnetization process is that the choice between the 'S' and 'C' seed states is made at much higher external fields (3000 Oe) than when visible signs of these states appear (1700 Oe).

Exploring the dynamics of the spins being affected by the total magnetic field (stray field plus externally applied field) is necessary to fully understand the magnetization reversal process in the two cases studied here. From [19] it is well known that the magnetization configurations nucleating in confined systems while sweeping the externally applied magnetic field are emerging from dynamic instabilities driven by softening (viz., vanishing frequency) of a particular spin standing-wave mode. In Figure 6-9(b) the spatial profiles of the lowest frequency spin wave modes in the horizontal nanomagnets are observed as a function of the external field and for angles of the external field below 2.5^0 and over 2.5^0, where the later case results in a reversal through a single-domain magnetic state and the former corresponds to a reversal where an stable magnetic vortex state is formed. The snapshots of the out of plane component of the precessing magnetization δm_Z for the low frequency modes at different values of the externally applied field are analyzed in Figure 6-9(b) as a contour plot superimposed to the vector plot of the in-plane equilibrium magnetization.

In particular, Figure 6-9(b) shows that there is a dynamic phase transition occurring at an external field of 3000 Oe, in both misaligned in aligned cases. This phase transition is caused by softening of the AS1-EM mode (AS stands for antisymmetric, and EM is the label for end-mode, which is a dynamic mode

localized in regions close to the borders of a nanoelement). At a particular field value the system is experiencing an instability situation, where any small perturbation can determine which is the subsequent magnetization dynamic mode. There are two possible dynamic states emerging from softening the AS-1 EM mode: S0-EM or AS0-EM, which are the lower energy symmetric and antisymmetric spin-wave modes, respectively, and are almost degenerate according to [20]. In the presence of a uniform magnetic field the symmetric (S0-EM) mode is favoured. In the aligned case, the dipolar fields created by the vertical nanomagnets might push the horizontal nanoislands towards the antisymmetric (AS0-EM) spin-wave mode, depending on the components of the total field acting on these nanoislands.

Looking back to Figure 6-10, now it is understood that the plot at which one has to look is the black one, in which the total field is 3000 Oe. By looking at the spatial distribution at 3000 Oe, that is the field at which the dynamic mode is going soft, it can be observed that at an angle above 2.5^0 for the external field the horizontal component of the total field is never negative, whereas when the external field is applied below 2.5^0 this component has a negative value at one end of the nanomagnet at the bottom edge (while it remains positive at the other end). This negative value of the horizontal component of the total field is acting on the bottom edge of the nanoisland. The softening of the AS1-EM mode in this situation leads to the AS0-EM mode, which is the dynamic state generating the 'C' state that is observed when further decreasing the total field in the aligned case, as observed in Figure 6-9(b).

The present finding shows that the low field behavior of a nanoisland is decided at high fields far above the individual island's coercive field. It is further demonstrated here that the fundamental assumption of single domain, Ising-like behavior of each nanoelement can breakdown, even when its size is substantially below that for single domain behavior in the isolated element. Furthermore, this mechanism shows that the magnetization reversal pathway can be engineered by properly designing dipolar magnetic field sources.

6.2.3. Different lateral dimensions of the nanomagnets

As previously discussed, the energetically most favorable magnetization state at remanence of a nanomagnet depends on its dimensions; the plot of the single-domain/vortex boundary in Figure 6-2 shows that when the aspect ratio of a nanoisland is increased the single domain state becomes more and more energetically favored with respect to the magnetic vortex state. It has been shown that the magnetization reversal process through which a vortex state is induced and found stable at remanence is observed in nanomagnets with certain dimensions: 700nm long, 160nm wide and 25nm thick. If the width of the nanoislands is kept constant and the length is increased (increasing the aspect ratio of the nanoislands) the total energy of the single domain magnetization state remains almost constant, whereas the energy of a magnetic vortex state increases with the length of the nanomagnet, as obtained from micromagnetic simulations. This trend can be observed in Figure 6-11.

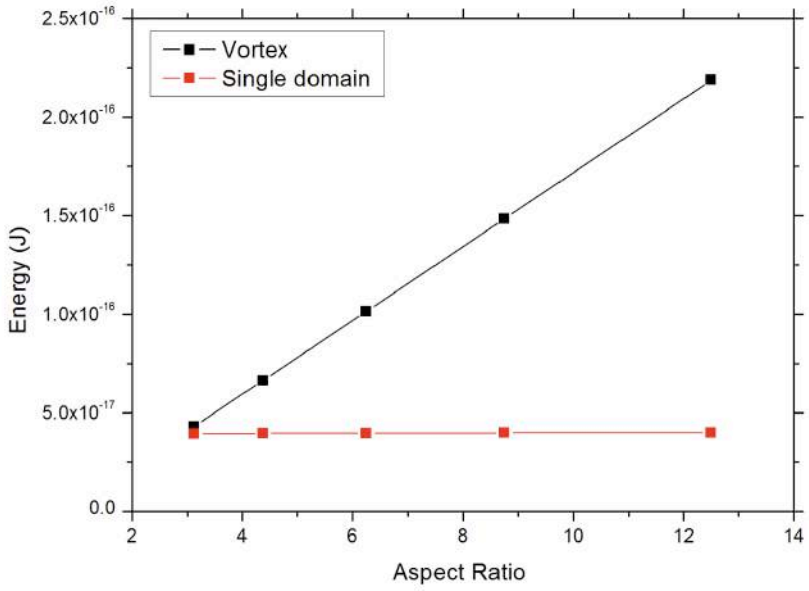

Figure 6-11: total energy of the Single-domain magnetization state (red) and of the magnetic vortex state (black) as a function of the aspect ratio of the nanoisland for a fixed width (160nm) and thickness (25nm) values.

The increase in the cost of inducing a magnetic vortex state in nanoislands with higher aspect ratio can be explained via the competing energy terms to the total energy of the nanoisland. The demagnetizing energy is not substantially

increased when the length of the nanomagnet increases, as the stray field created by the vortex state does not change substantially when it is accommodated over a larger nanoisland; nevertheless the exchange energy increases when the length of the nanomagnet increases because the magnetic vortex state forms a sort of domain wall between two opposite domains (similar to a Landau state, as the vortex core is transformed into this elongated 'domain wall' region when it is relaxed), forcing more neighboring spins to increase the angle between them in that region and, therefore, increasing the total exchange energy of the nanomagnet. In the case of the single domain magnetization state this analysis of the competing energy terms can be also performed in order to explain why the cost of having this magnetization state does not almost change when increasing the aspect ratio. In this case, the demagnetizing energy does not dramatically change, as the stray field created by the nanomagnet is due to the spins close to the two edges of the nanomagnet, whose total amount of magnetic moment does not change; similarly, the exchange energy of the nanomagnet does not increase when increasing the length of the nanomagnet, as all the spins inside the magnetic nanoisland remain (almost) parallel. Therefore, the total energy of the single domain magnetization state remains almost constant when increasing the aspect ratio of the nanomagnet while keeping the width and thickness constant. A conclusion derived from this study indicates that the energy difference between the single domain magnetization state and the magnetic vortex state increases when the aspect ratio is increased (for constant width and thickness), making the magnetic vortex state more and more energetically unfavorable with respect to the single domain.

A similar analysis can be performed for a different case: keeping the aspect ratio constant and varying the length. If the aspect ratio of the initial case studied (length= 700nm, width=160nm, AR=4.375) is kept constant, and for a constant thickness of 25nm, the total energies of the single domain magnetization and the magnetic vortex states, together with the energy differences between them, are plotted in Figure 6-12 as a function of the length of the nanomagnet.

As observed in Figure 6-12, when the aspect ratio is kept constant the energy difference between the magnetic vortex and the single domain magnetization states (green plot) is slightly increased when the length of the nanomagnet is increased. In this case, when analyzing the competing energy terms in each magnetization state the situation changes with respect to what happened when the width was kept constant and increasing the length (Figure 6-11). In the magnetic vortex state the exchange energy increases due to the fact that the amount of total magnetic moments forming the 'domain wall' (elongated vortex core when the vortex state is relaxed, similar to a Landau state) increase, and therefore the number of neighboring misaligned magnetic moments increase, giving rise to a net increase of the total exchange energy of the magnetic vortex state. Nevertheless, the increase of the radius of curvature of the vortex provokes that the angle between adjacent spins decreases, and there is a mild increase of exchange energy due to this effect. The demagnetizing energy remains almost unaltered, as the stray field created by the nanomagnet in the magnetic vortex state is similar when increasing its lateral dimensions. Hereby, the total energy of the magnetic vortex state increases when the lateral dimensions are increased (keeping the aspect ratio constant) because the exchange energy is increased.

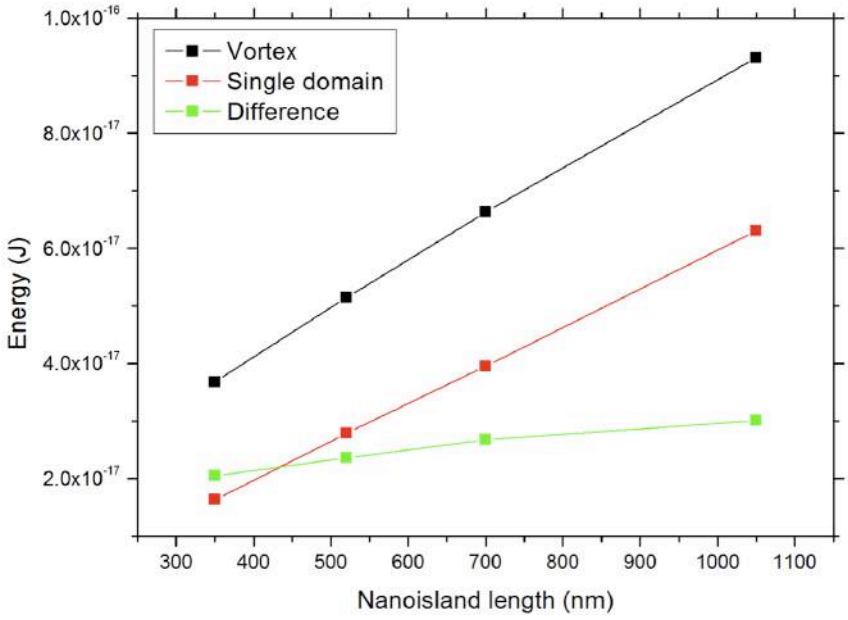

Figure 6-12: total energy of the single domain magnetization state (red) and of the magnetic vortex state (black), and the difference between them (green) as a function of the length of the nanomagnet for a fixed aspect ratio (4.375) and thickness (25nm) values.

In the case of the single domain magnetization state the exchange energy remains almost unaltered, as all the magnetic moments in the nanomagnet are (almost) parallel and adding more magnetic moments do not affect this situation. On the contrary, the demagnetizing energy increases in this case, due to the fact that the total stray field created by the nanomagnets increases when the amount of magnetic material is increased in the edges of the nanomagnet, which happens when the lateral dimensions of the nanomagnet are increased. Therefore, the total energy of the single domain magnetization state also increases when the lateral dimensions of the nanomagnet increase while keeping the aspect ratio constant.

It is important to remark that the origin of the increase of the total energy in the case of the magnetic vortex state is due to the growth of the exchange energy, mitigated by the increase of the vortex radius (which decreases the angle differences between adjacent spins) whereas in the case of the single domain magnetization state this growth comes from the increase of the demagnetizing energy.

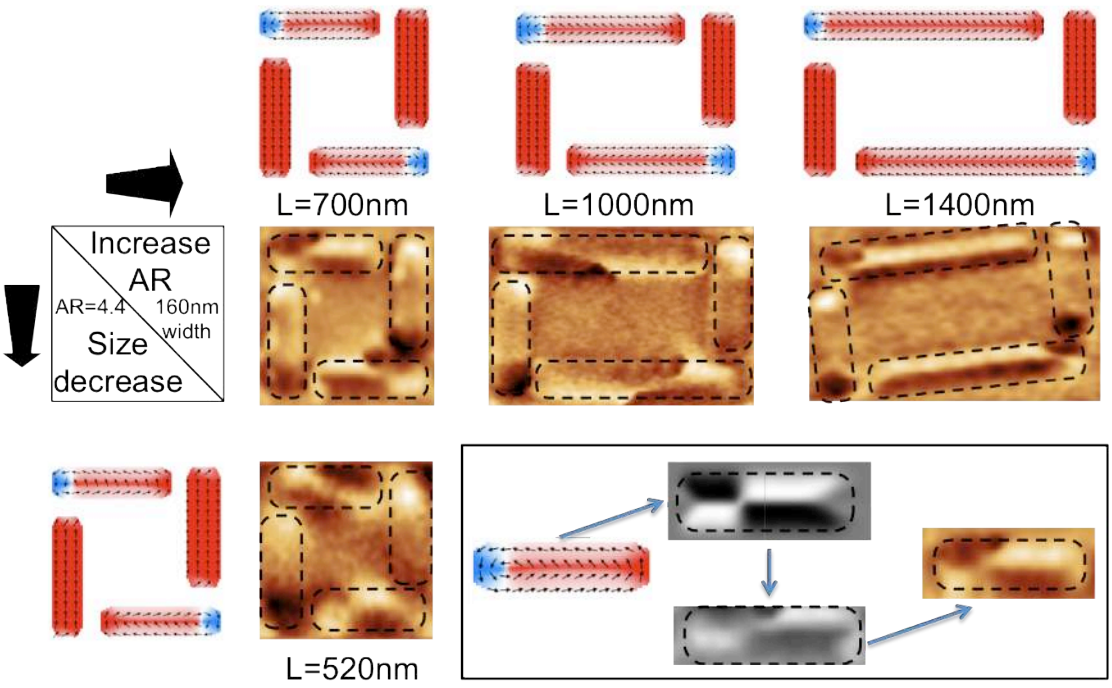

Figure 6-13: micromagnetic simulations and magnetic force microscopy images of four different nanoisland sizes with increasing aspect ratio (horizontal) and keeping constant the aspect ratio while decreasing the lateral size (vertical). The inset shows a micromagnetic simulation of a vortex state from which the MFM image is calculated, compared to the measured MFM image in grey scale and with the same MFM image with the color code used in the viewgraph.

Experimental evidence of this analysis of the behavior of the competing energy terms when the dimensions of the nanomagnets are changed, together with micromagnetic simulations and magnetic force microscopy imaging of the samples, is presented in Figure 6-13. This figure shows that, in spite of the increase of energy differences between the single domain and vortex states, a vortex is nucleated in every case due to the robustness of the process showed in the previous section.

Experimental results and simulations confirm that the reversal process in the aligned case occurs via vortex nucleation, as in the simulations the magnetic vortex state is found stable at remanence for all the nanoislands' sizes studied experimentally: aspect ratios of 4.375 (case studied previously in this chapter), 6.25 (length=1000nm, width=160nm) and 8.75 (length=1400nm, width=160nm), keeping the thickness at 25nm. Also when decreasing the lateral sizes of the initial sample, for nanoislands with dimensions of 525nm long and 120nm wide (same aspect ratio, 4.375, as the initial sample shown in Figure 6-4) a magnetic vortex state is found in the simulations and experimentally in the aligned case.

6.2.4. Nanoisland thickness

In the previous section the role of changing the lateral dimensions of the nanomagnets, keeping their thickness constant, has been analyzed. The next step is to analyze how a change on the thickness of the nanoislands affects the final states at remanence on the magnetization reversal process in the so-called aligned case.

The analysis of the energies of the single domain magnetization and magnetic vortex states can be performed by means of micromagnetic simulations; in this way the effect of varying the thickness on nanomagnets on the energies of the magnetic vortex and the single domain magnetization states can be observed in Figure 6-14. In this plot the energies of the two magnetization states are plotted

as a function of the thickness of the nanoisland, for nanoislands with lateral dimensions of 700nm long and 160nm wide, keeping therefore the aspect ratio fixed to 4.375.

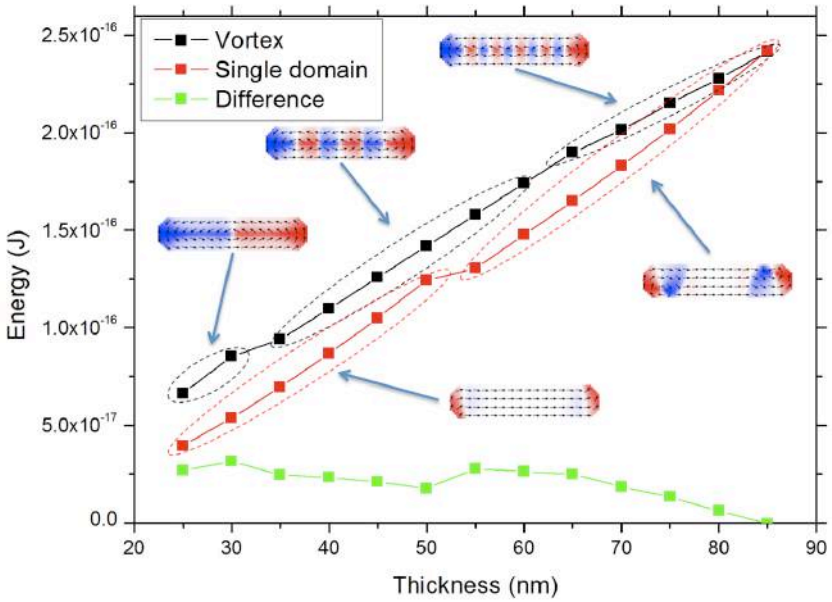

Figure 6-14: total energy of the 'single domain' magnetization state (red) and of the magnetic vortex state (black), and the difference between them (green) as a function of the thickness of the nanomagnet for a fixed length (700nm) and width (160nm) values. The different magnetic configurations found at remanence in each case are shown as insets, as calculated by means of OOMMF.

A quick inspection at Figure 6-14 tells that both the single domain magnetization state and the magnetic vortex state energies increase when the thickness of the nanomagnet increases. In the case of the magnetic vortex state this increase is related to an increase of both the exchange and the demagnetizing energy terms, as more magnetic material generates more stray field (hence the demagnetizing energy increases) and also more neighboring magnetic moments are misaligned with respect to each other (increasing the exchange energy); nevertheless in the single domain magnetization state only the demagnetizing energy term increases (more magnetic moments at the edges of the nanoisland generate more stray field), whereas the exchange energy term remains almost zero (all the magnetic moments of the nanomagnet are almost perfectly aligned).

But this is not the whole story: with a more detailed look into the graphs of Figure 6-14 it can be observed that both the curve for the energy magnetic

vortex state and the one for the energy of the single domain magnetization state have discontinuities in their slopes (and, therefore, also the difference between the energies of the two magnetization states, given by the green curve). These discontinuities appear, in the case of the energy of the magnetic vortex state, for thicknesses of 35nm and 75nm; and in the case of the energy of the single-domain magnetization state for a thickness of 55nm.

The discontinuities in the curve for the energy of the magnetic vortex state are due to the fact that, instead of having a single vortex in the nanomagnet (up to thicknesses of 30nm), three vortices with the same chirality separated by two antivortex cross-tie-like domain walls (see Figure 6-15(a)) appear as the stable state at remanence for the aligned case when the thickness of the nanoislands is between 35 and 70nm, and five vortices preserving chirality separated by four antivortex cross-tie-like domain walls are the stable state for thicknesses above 75nm. This can be understood by looking at the contributing energy terms to the total energy of the nanomagnet while increasing the thickness: the exchange and demagnetizing energy terms. When the thickness increases the total exchange energy also increases, as the number of non-parallel neighboring spins is higher, and this exchange energy increases with the number of vortices inside the nanomagnet at remanence (bigger angle between neighboring spins). On the contrary, the demagnetizing energy decreases when the number of vortices in the nanoisland increases, due to the fact that the stray field produced by the nanomagnet is reduced when the number of vortices increases. Therefore, the interplay between the exchange and demagnetizing energy terms, when balancing the total energy, favors the increase of vortices.

In the case of the discontinuity in the curve for the energy of the single domain magnetization state is that when the thickness is higher than 50nm the remanent state found in an isolated nanoisland (or in a nanoisland in the misaligned case, which is equivalent, as its seed state is an 'S' state) consists of two vortices of opposite chirality, one at a lower end of one edge of the nanoisland and the other at the upper end of the other edge, symmetric to the previous one, while the central part of the nanomagnet remains uniformly magnetized (see inset in

Figure 6-14). This can be understood from the fact that the total demagnetizing energy increases when increasing the thickness when having a uniformly magnetized nanoisland (single domain) with almost no exchange energy, up to a point in which the nucleation of these two vortices with opposite chirality considerably reduces the demagnetizing energy while having the exchange energy increased in the regions where the two vortices are nucleated. The value of the thickness in which having more exchange while the demagnetizing energy is reduced is energetically favorable is above 50nm, when the lateral dimensions of the nanomagnet are 700nm long and 160nm wide.

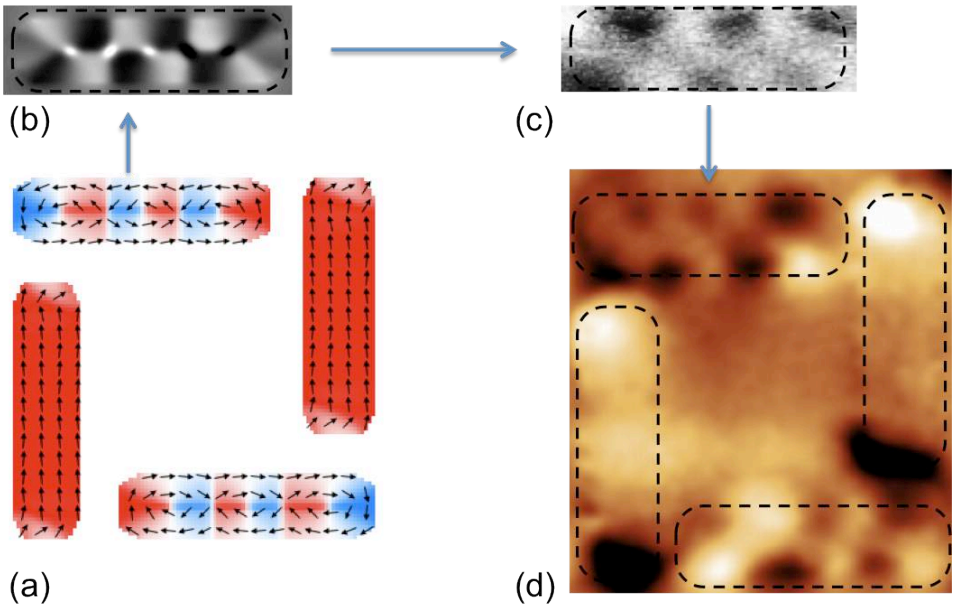

Figure 6-15: Remanent magnetization state in the aligned case for nanoislands 700nm long, 160nm wide and 40nm thick (a), with a computed MFM image of the three-vortices magnetic state (b), the measured MFM image of the three-vortices magnetic state in black and white contrast to compare it with the calculated one (c), and the measured MFM image of the remanent state in the aligned case reproduced in (a) with the micromagnetic simulations (d).

This analysis of the magnetization states in nanomagnets with increased thickness has been experimentally corroborated by analyzing the magnetization reversal process in interacting ferromagnetic nanoislands with 40nm thickness. After performing MOKE magnetometry on the same array shown in Figure 6-4, but with nanoislands with dimensions 700nm long, 160nm wide and 40nm thick, magnetic force microscopy images of the magnetization state of the nanomagnets at remanence in the aligned case (vortex formation) have been taken. Experimental evidence of the formation of a three-vortices magnetic state

in the aligned case has been obtained, by looking at the magnetic force microscopy image shown in Figure 6-15(d), together with the remanent state found in the aligned case when performing micromagnetic simulations in nanomagnets with the same dimensions than the measured ones. (Figure 6-15(a)).

6.3. Conclusions

The magnetization reversal process of interacting ferromagnetic nanoislands of different sizes has been investigated, finding that the role of spatially inhomogeneous and asymmetric magnetostatic dipolar interactions onto this magnetization reversal process of nanomagnets, arranged in square units with chiral structure, together with the dynamic instabilities present during the process is crucial to understand the behavior of the magnetization in the nanomagnets during the reversal. The analysis of the magnetization reversal process has been investigated by means of MOKE magnetometry, analyzing the changes on the intensity on both the reflected and diffracted beams, to obtain the hysteresis loops of the reversal process, together with magnetic force microscopy to image the resulting magnetization states at remanence. Micromagnetic simulations by means of the OOMMF code have also been performed in order to understand and support the experimental data obtained in the magnetization reversal process, obtaining perfect agreement between the experimentally obtained data and the simulations performed.

The magnetization reversal process in the arrays of nanomagnets studied presents two completely different pathways depending on the angle at which the external field is applied. When this external field is applied at an angle bigger than 2° away from the edge orientation of the square units of the array ('misaligned' case) the reversal is dominated by the shape anisotropy of the nanomagnets and the magnetostatic dipolar interactions do not play a relevant role in the reversal process, being accomplished via single domain magnetization states at remanence in all the nanomagnets forming the array. On the contrary,

when the external field is applied at an angle smaller than 2° ('aligned' case) the magnetostatic dipolar interactions, together with the evolution of the dynamics, modify substantially the magnetization reversal pathway: the spatial asymmetry of the dipolar interaction fields causes the formation of vortex states of well-defined chirality in the nanoelements with their long axis (almost) perpendicular to the externally applied field.

The differences on the magnetization reversal paths followed by the nanomagnets have been found to start appearing at applied fields far above the saturation field values of the nanomagnets with magnetization dynamics analysis. The dynamics of the nanomagnets whose easy axis is perpendicular to the applied field show that the resulting spin-wave end-modes change depending on the orientation of the external applied field: in the misaligned case a symmetric end-mode results from the softening of the higher energy dynamic state, whereas in the aligned case an antisymmetric dynamic end-mode appears. These two end-modes lead to the formation of a uniform magnetization and a vortex state, respectively, in the nanoislands.

These well-differentiated magnetization reversal pathways have been found to occur even in nanoislands with lateral dimensions in which the total energy of the vortex state is much higher with respect to the single-domain magnetization state, where magnetic vortex states have been trapped and imaged in the aligned case in nanomagnets with high aspect-ratios (1400nm long and 160 nm width). Finally, the role of changing the thickness of the nanomagnets has also been analyzed, finding that the magnetization reversal process in the aligned case leads to a breakdown of the vortex state into a sequence of vortex-antivortex states at remanence when the thickness of the nanomagnets is increased, and in the case of nanoislands with dimensions 700nm long 160nm wide and 40nm thick a three-vortex state, separated by two antivortex, has been imaged via MFM.

6.4. References

[1] K. J. Kirk, *Contemporary Physics* **41**, 2 (2000)

[2] M. N. Leuenberger and D. Loss, *Nature* **410**, 789-793 (2001)

[3] S. Karthikeyan, A. E. Hill and R. D. Pilkington, *Thin Solid Films* **520(1)**, 266-271 (2011)

[4] B. N. Engel *et al.*, *IEEE Trans. Mag*. **41(1)**, 132-136 (2005)

[5] L. Bogani and W. Wernsdorfer, *Nat. Materials* **7**, 179-186 (2008)

[6] J. Sort, A. Hoffmann, S. H. Chung, K. S. Buchanan, M. Grimsditch, M. D. Baró, B. Dieny and J. Nogués, *Phys. Rev. Lett*. **95**, 067201 (2005)

[7] D. A. Garanin and H. Kachkachi, *Phys. Rev. B* **80**, 014420 (2009)

[8] W. Wernsdorfer et al., *Phys. Rev. Lett*. **78**, 1791–1794 (1997)

[9] R. P. Cowburn, D. K. Kolstov, A. O. Adeyeye and M. E. Welland, *Phys. Rev. Lett*. **83**, 1042-1045 (1999)

[10] G. Csaba, A. Imre, G. H. Bernstein, W. Porod and Vitali Metlushko, *IEEE Trans. Nanotech*. **1(4)**, 209-213 (2002)

[11] A. Imre, G. Csaba, L. Ji, A. Orlov, G. H. Bernstein and W. Porod, *Science* **311**, 205-208 (2006)

[12] R. F. Wang et al., *Nature* **439**, 303 (2006)

[13] J. M. Porro, A. Berger, M. Grimsditch, V. Metlushko, B. Ilic and P. Vavassori, *J. Appl. Phys*. **111**, 07B913 (2012)

[14] OOMMF code made by NIST: http://math.nist.gov/oommf/

[15] N. A. Usov, C. R. Chang and Z. H. Wei, *J. Appl. Phys*. **89**, 11 (2001)

[16] P. Vavassori, *Appl. Phys. Lett*. **77**, 1605 (2000)

[17] M. Grimsditch and P. Vavassori*, J. Phys: Condens. Matter* **16**, R275 (2004)

[18] P. Vavassori, M. Grimsditch, V. Novosad, V. Metlushko and B. Ilic, *Phys. Rev. B* **67**, 134429 (2003)

[19] G. Leaf, H. Kaper, V. Novosad, P. Vavassori, and M. Grimsditch, *Phys. Rev. Lett.* **96**, 017201(2006)

[20] F. Montoncello et al., *Phys. Rev. B* **76**, 024426 (2007)

7. Accessing the ground state in artificial spin-ice systems

7.1. Introduction

7.1.1. Spin Ice: the concept

In water ice the crystalline atomic disposition of the oxygen and hydrogen atoms possesses degrees of freedom that lead to the existence of the so-called residual entropy. This means that even if the water ice crystalline structure is cooled to zero Kelvin temperature the degeneracy of the ground state of the structure makes the entropy of the system to be different from zero. This effect is also named intrinsic randomness, and comes from the fact that the crystalline structure of ice is formed by a central oxygen atom surrounded by four neighboring hydrogen atoms. These hydrogen atoms are disposed in the vertices of a tetrahedron whose geometrical center is occupied by the oxygen, where two of the hydrogen atoms are close to the central oxygen atom whereas the other two are closer to the surrounding oxygen atoms belonging to neighboring tetrahedrons: this is the so-called 'ice rule' of water ice. This configuration has been schematized in Figure 7-1(a). The frustration comes from the position of the hydrogen atoms with respect to each central oxygen: the degeneracy of the ground state is given by the possible degenerated configurations for the two hydrogens closer to the central oxygen. This observation of the existence of degenerated states that lead to the residual entropy present in water ice was first observed in 1935 by L. Pauling [1], who also realized that the degenerated ground-state configurations at zero Kelvin is extensive, growing with the size of the system. This frustration phenomena occurring between the hydrogen and oxygen atoms in water ice has been focus of study more recently [2].

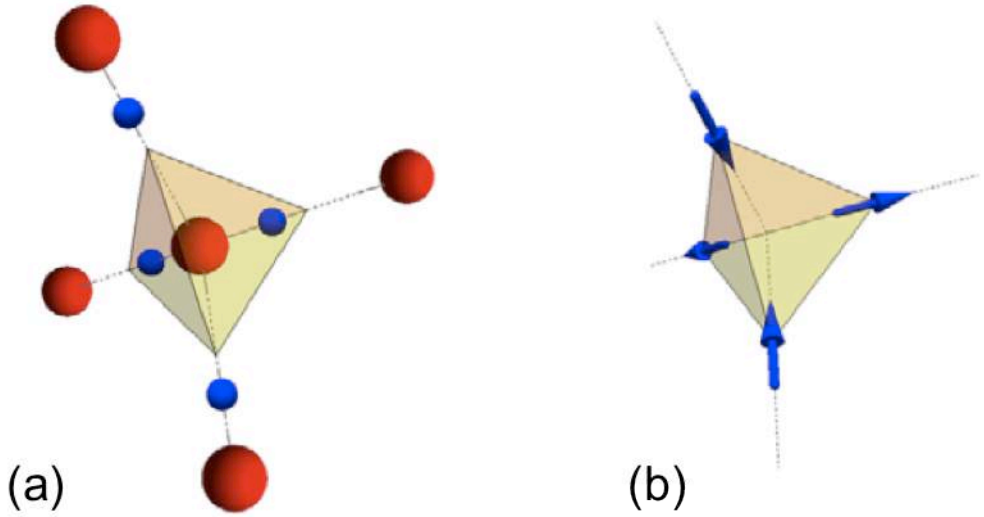

Figure 7-1: structure of water ice, with the four H^+ atoms (blue) in the vertices of a tetrahedron with a centered O^{2-} in its center (red), where two of the H^+ atoms are closer to the central O^{2-}, following the two in/two out ice rule (a), and spin structure of the pyrochlore rare earth 'spin ice' material whose spins follow the two in/two out spin ice rule (b).

The discovery of a similar behavior to that of the water ice in the rare earth pyrochlore $H0_2Ti_2O_7$ [3], with the presence of frustration due to the interactions between the spins on the corners of the pyrochlore tetrahedrons in the ground state of the system, lead to the appearance of the terminology 'spin ice' for the first time. In this case, the magnetic spins play the role of the hydrogen atoms in water ice. The four spins present at the vertex of each tetrahedron in the pyrochlore crystalline structure point towards or away from the centre of the tetrahedron, leading to the equivalent two spins in/two spins out ice rule for the lowest energy state, as schematized in Figure 7-1(b). Similarly to what is observed in water ice at zero Kelvin, an extended arrangement of tetrahedrons in the pyrochlore crystalline structure has a ground state composed of a large number of these two in/two out arrangements, being the ground state extensive as in water ice.

7.1.2. Artificial Spin Ice

Since the discover of the possibility of studying how frustration is accommodated within spin ice materials, model systems mimicking that spin ice materials' behavior have been proposed. It was in 2006 when this idea was

realized by mimicking the behavior of the three-dimensional pyrochlore spin ice material with arrangements of nanomagnets interacting through their dipolar stray fields in a two-dimensional lattice created by means of electron-beam lithography [4]. It is a requirement in artificial spin ice systems that all the interacting nanomagnets composing the array show an Ising-like behavior of their magnetization; i.e. a bistable magnetization behavior in which the only possible magnetic states are the two single domain magnetization states pointing towards opposite directions, mimicking in this way the behavior of a spin. Therefore, each nanomagnet behaves as a macrospin, and the two-dimensional lattice of nanomagnets resembles that of a lattice of interacting spins, as observed in Figure 7-2, where the dipole-dipole interactions between neighboring nanomagnets create two-dimensional analogues of real spin-ice systems. Different geometries for the arrangement of the nanomagnets in artificial spin ice systems have been proposed: triangular [5], square (schematized in Figure 7-2) [4, 6, 7], hexagonal [8, 9], with interconnected [8] and isolated [4, 5, 6, 9] nanoislands.

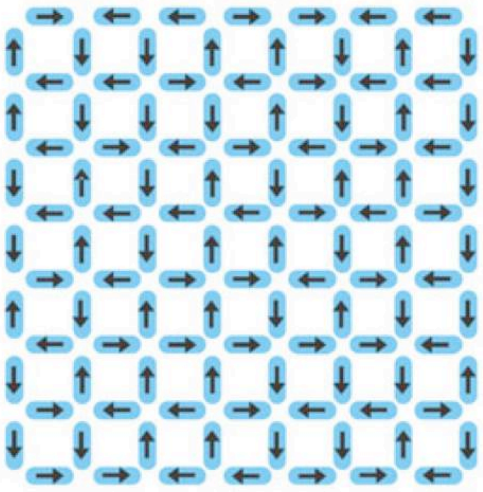

Figure 7-2: array of interacting nanomagnets disposed forming a square artificial spin ice lattice, following the two in/two out ice rule.

In artificial spin ice systems the magnetic moments of the nanomagnets (macrospins) play the role of the hydrogens and the frustration comes from the geometry of the array and the dipolar interactions that occur in each vertex formed by the edges of the nanomagnets. In this way, at a vertex each magnetic

moment of the four nanomagnets will be pointing inwards or outwards, each of them contributing to the net magnetic charge at the vertex center. Considering a pair of magnetic moments, the energetically favorable configuration is the one in which one points inwards and the other outwards, whereas in the unfavorable one both point inwards or outwards.

In this work the geometry used to carry on the experiments is the square artificial spin ice lattice (Figure 7-2), which corresponds to two perpendicular sublattices of lines of interacting nanomagnets so that four edges will converge at each vertex: even in the lowest energy configuration of the magnetization, corresponding to the ice rule, the two magnetic moments pointing both inwards or outwards are frustrated. This ground state is degenerated, with two possible configurations of magnetic moments, leading to the previously mentioned residual entropy at the ground state energy level of the system.

7.2. Description of the experiment

7.2.1. Energy levels of the system: vertex configurations

In an artificial spin ice pattern formed by interacting nanomagnets the total energy of the system is given by the sum of the local energy values present at each vertex where the magnetic moments of the nanomagnets meet. Each of the nanomagnets composing the artificial spin ice pattern can be considered as a macrospin, as the shape anisotropy forces the spins to align in a single domain magnetization state (neglecting configurational anisotropy) and the exchange energy can be neglected. In the case of the square artificial spin ice pattern there are 16 different possible configurations for the macrospins of the nanomagnets to form at each vertex, which can be grouped into four different vertex types each of them with the same magnetostatic energy and net vertex magnetic charge, but different degeneracy. All the possible 16 vertex configurations gathered in groups with the same energy, together with the energy differences

between the four different vertex types with respect to the Type I, are shown in Figure 7-3.

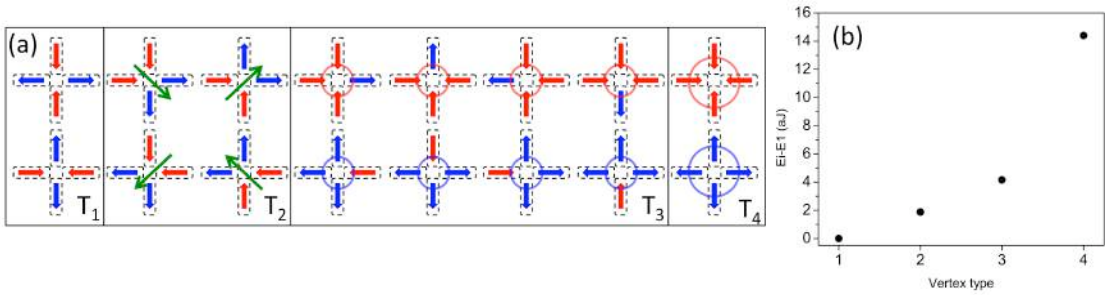

Figure 7-3: the 16 possible magnetic vertex configurations, gathered in groups with the same energy and ordered from the lowest (T1) to the highest (T4) vertex energies. Green arrows indicate the direction towards which the magnetic net moment present at the T2 vertices points, and the red and blue circles in T3 and T4 vertices indicates the net magnetic charge (positive and negative, respectively) present at each vertex (a). Vertex energy differences (E_i-E_1, i=1,2,3,4) for each vertex type at room temperature for nanomagnets with dimensions 300x100x25nm³ made of Permalloy (b).

As can be observed from Figure 7-3, both Type I and Type II vertex fulfill the two in/two out ice rule but, contrary to what occurs in Type I vertex, in Type II vertex two nearest neighbor macrospins point inwards or outwards, leading to the appearance of a net magnetic moment in Type II vertex that increases the net energy in that type of vertex with respect to a Type I vertex. In a Type III magnetic vertex three of the magnetic moments point inwards or outwards and the other one in the contrary direction, having therefore a net positive or negative magnetic charge (q_m=±1); and in a Type IV vertex all the magnetic moments point inwards or outwards, and the vertex has a net magnetic charge (q_m=±2) that is twice the one present in Type III vertex. Based on an equiprobable distribution of configurations of all the vertex in a square artificial spin ice pattern, the percentage of each vertex type should be given by the degeneracy of each given vertex type: 12.5% of the vertex would be Type I vertex, 25% Type II, 50% Type III and, finally, another 12.5% would be Type IV vertex. But as the vertex energy types do not have the same energy, one would expect to have a ground state comprising a checkerboard of alternating Type I vertex. However, the observation of such ground state ordering in artificial spin ice systems would depend on the actual process through which the 'frozen' state (stable magnetic state) is induced. Most of the studies reported so far rely on

direct imaging of the magnetic configurations at room temperature using techniques such as magnetic force microscopy (MFM), X-ray photoemission electron microscopy (XPEEM) and Lorentz transmission electron microscopy (LTEM). Thereby, it is a requirement that the magnetic islands are thermally stable at room temperature to image a magnetization state in order to analyze the total energy of the system formed by the array of interacting nanomagnets.

A possible solution to have thermally stable nanomagnets at room temperature is to choose an aspect ratio and a volume large enough so that the energy barrier, mainly due to shape anisotropy, is much higher than thermal excitations at room temperature. The artificial spin ice pattern will 'melt' at a temperature corresponding to the blocking temperature T_B of the nanomagnets, which is the temperature at which a magnetic material undergoes a transition from the ferromagnetic to the superparamagnetic regime within an observation time frame (measurement time) t_m, and it is given in [10] and in a more general way in [11] as:

$$T_B = \frac{KV}{k_B \ln\left(t_m / t_0\right)} \tag{7-1}$$

where $K = \frac{1}{2}\mu_0 M_S^2 \Delta N$ is the shape anisotropy constant, V is the volume of the nanomagnet, k_B the Boltzmann constant, t_m is the observation time, and t_0 is the attempt time of the order of 10^{-10}s. ΔN is the difference between the demagnetizing factors along the in plane short and long axes of the island, respectively. Above this temperature, the nanomagnets retain their magnetic moments, provided $T_B<T_C$, but thermal energy makes them flipping continuously between the two stable directions dictated by the shape anisotropy. However, for nanomagnets of the size that can be fabricated using state of the art lithography with a sufficient control of the island geometry, thermal 'melting' of the system would require such a high temperature that would damage the

sample, eventually destroying it. For 300x100x25nm^3 islands, as those investigated here, assuming t_m=1s and that the material of the nanomagnets is Permalloy (saturation magnetization at 0K M_s = 865x10^3 A/m) the calculated blocking temperature would be $T_B \approx 10^5$K.

But this is not the real picture, due to the fact that there is a dependence of the magnetization with the temperature $M_s(T)$, so that the nanomagnets will reach their blocking temperature T_B at a much lower temperature, close to the Curie temperature T_C of the constituent material. Nevertheless, it is, however, still high enough to damage permanently a sample made of standard ferromagnetic materials such as Fe, Co or Py (Permalloy), which are the ones that have been used so far in related experiments. A reliable analysis of this situation with nanomagnets of materials and sizes used in previous experiments, considering the $M_s(T)$ dependence of Permalloy (T_C=853K), the calculated blocking temperature is $T_B \approx 847$K for nanoislands 300nm long, 100nm wide and 25nm thick. When trying to anneal the artificial spin ice array with nanoislands with these dimensions made of Permalloy at a temperature above the blocking temperature the sample was completely destroyed. Therefore, attempts to induce ground state ordering have been carried out so far by applying external magnetic fields [12], approach that will be discussed later on in this chapter.

Recent studies conducted in as-grown artificial spin ice samples proved that it is possible to achieve large ground state ordering regions [6] on samples with the previous sizes and material. These observations rely on the fact that when the nanomagnets are being grown, during the initial stage of the deposition of the magnetic material, the thickness and, therefore, the volume of the nanomagnets is small enough so that the shape anisotropy energy E_A, which is the energy barrier that each nanoisland has to overcome in order to flip its magnetic moment, given by:

$$E_A = K \cdot V = \frac{1}{2}\mu_0 M_S^2 \Delta N \cdot V \qquad (7\text{-}2)$$

is comparable to the thermal energy E_{th}:

$$E_{th} = k_B T_D \qquad (7\text{-}3)$$

at the deposition temperature T_D. At the same time, the dipolar interactions between neighboring nanomagnets at each vertex are not negligible, so that their magnetic moments' orientations at each vertex of the array can try to rearrange themselves in the most favorable configuration before the magnetic moments of the nanomagnets become frozen. The thickness of the nanomagnets increases during the growth, producing the increase of the anisotropy energy barrier above the thermal energy excitations, thus 'freezing' the magnetization of the nanomagnets. The results obtained in these measurements show long-range ground-state (formed by Type I vertices) ordering regions in the square artificial spin ice array, separated by narrow boundaries made of Type II and Type III vertices identified as elementary excitations of the system [6] (a MFM image of the as-grown state obtained in [6] will be presented and discussed later on in this chapter, in Figure 7-8).

Even if this method seems to work accurately in order to induce sizable ground state ordering in artificial spin ice patterns, it is a limited methodology since it is a single-shot approach, which prevents any systematic study of the physical processes involving the ground state ordering formation. In addition, if any external perturbation alters the magnetic ordering state, this cannot be recovered. Therefore, devising an alternative method to avoid these limitations opens up a new pathway for the systematic study of the interesting physics of artificial spin ice patterns characterized by long-range ground-state ordering regions. Taking into account what has already been discussed above, it is apparent that heating the sample above the blocking temperature would require the fabrication of very small nanoislands in order to reduce T_B to values much below T_C that can be reached without damaging the sample. As an example, given the magnetization of Permalloy and considering a T_B of 750 K as a reasonable value of temperature that can be reached without causing permanent damages to the sample, a thickness of 1nm, and setting the aspect ratio of the nanoisland to 2, we obtain using the equation given above for T_B that the nanoisland should

have lateral dimensions of 20x10nm^2. The fabrication of such small nanostructures with the required uniformity over large arrays is a tremendous challenge, beyond the reach of current state of the art lithography.

7.2.2. Sample description and material properties

It has already been stated that nanoislands with dimensions of 300x100x25nm^3, which are the usual dimensions employed in artificial spin ice experiments in literature, made of permalloy are destroyed when trying to thermally anneal them over their blocking temperature, which is close to their Curie temperature (T_B=847K, T_C=853K). Therefore, here it is proposed a different pathway to overcome this problem. The dimensions of the nanoislands must be kept in a regime where the lithographic process is controlled at a level to obtain high-quality nanostructures, so that the distributions in size, shape and defects are not an issue for determining their magnetic properties and thermal relaxation. Our novel approach consists in changing the magnetic material composition in order to reduce the Curie, and thus Blocking, temperatures to the extent that they can be reached without destroying the nanostructures.

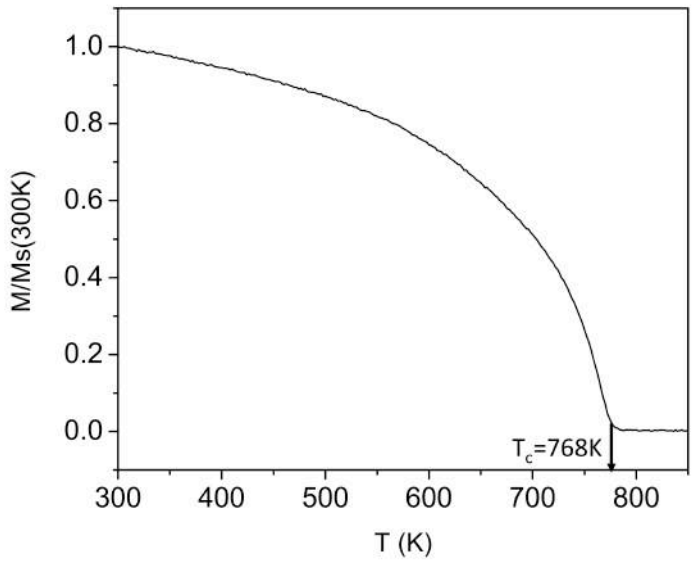

Figure 7-4: M vs T curve of a 25nm thick film of the $Ni_{87}Fe_{13}$ alloy normalized to the room temperature magnetization value, measured with a vibrating sample magnetometer (VSM). The Curie temperature of the alloy is marked in the graph.

The variation of the Curie temperature with the composition in Nickel-Iron alloys is well known [13]. Based on that, different nickel-iron alloys were deposited slightly varying the nickel-iron proportions. After this analysis, the selected alloy used to fabricate the nanostructures forming the artificial spin ice array has proportions of 87% Ni and 13% Fe, as its Curie temperature is T_C=768K, as can be observed from the measured magnetization versus temperature curve plotted in Figure 7-4. The magnetization of the $Ni_{87}Fe_{13}$ alloy at room temperature is 686x10^3A/m, i.e. lower than that of Py, but this is not a relevant issue by itself since the anisotropy energy barrier at room temperature is still 10^4 times bigger than the thermal energy excitations. This alloy was then used to fabricate arrays of nanomagnets 300nm long, 100nm wide and 25nm thick forming an artificial spin ice pattern nanostructure with a lattice parameter of 400nm by means of electron beam lithography. SEM images of portions of the sample are shown in Figure 7-5.

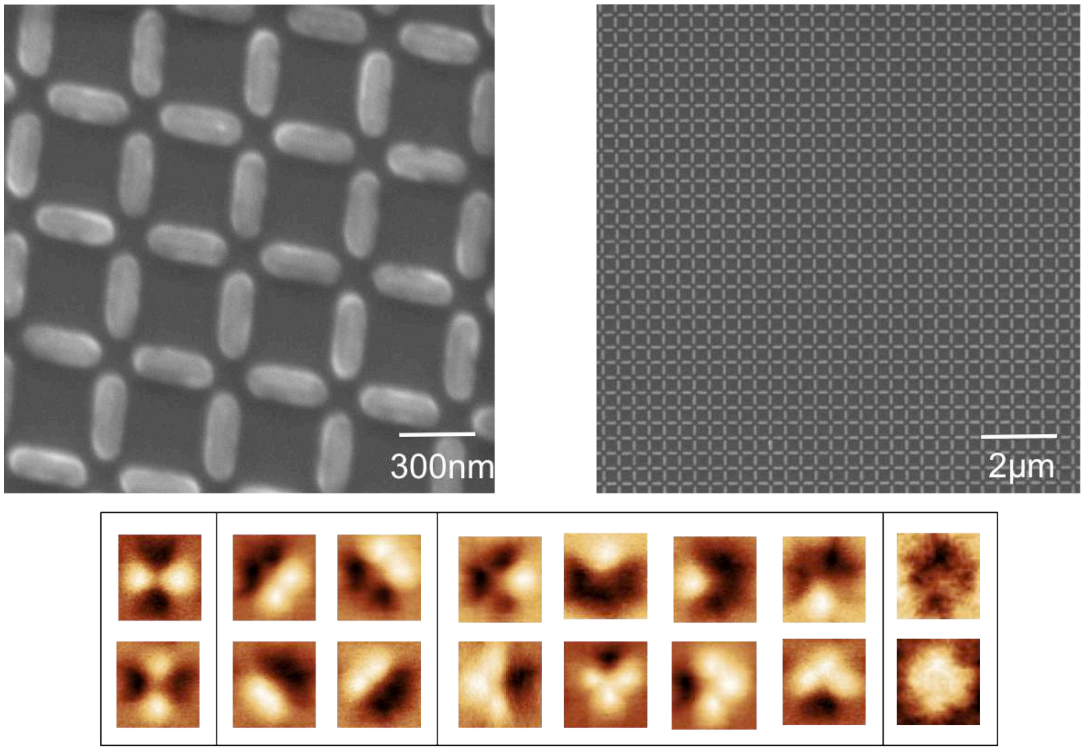

Figure 7-5: SEM images of the nanofabricated artificial spin ice pattern (up) and MFM images of each of the 16 possible vertex configurations imaged during the realization of the experiments (down).

The nanomagnets forming the artificial spin ice array have an Ising-like bistable magnetization behavior, which is a mandatory requirement. The magnetic alloy

was deposited at a rate of 0.8Å/s onto the electron-beam lithography structured sample using an electron-beam evaporator, while the sample was rotated at 15rpm to obtain a homogeneous distribution of the magnetic material. The resulting nanostructure is shown in Figure 7-5, together with magnetic force microscopy images of the 16 possible vertex configurations, as a guide to the eye for the interpretation of the MFM images that will be discussed later. They have been taken from different MFM images performed during the experiments: Type I, II and III vertex appear in every large (15x15μm^2) MFM image, whereas Type IV vertex only appear when imaging as-grown or non-thermal demagnetized states.

7.2.3. Demagnetization protocols

7.2.3.1. AC in-plane rotating magnetic field

One of the main objectives pursued by the scientific community studying artificial spin ice systems is to study behavior analogous to thermally active spins in spin ice systems, in order to determine how far is it possible to achieve a ground state ordering of the magnetization in the arrays, getting the closest possible to the lowest energy configurations. In this sense, one of the possible demagnetization protocols proposed to achieve the lowest possible energy state in artificial spin ice systems is the demagnetization through the application of magnetic fields. In these attempts to demagnetize the arrays of nanomagnets different approaches have been followed, involving rotating the sample about the in-plane or the out-of-plane sample axis in a magnetic field that is applied perpendicular to the rotation axis, and while the sample is rotating the applied magnetic field is reduced from a field value above the saturation one of the nanomagnets down to zero field [12]. In this study the net magnetic moment of the array is diminished to values close to zero, but the total energy retained by the artificial spin ice system remains far from the ground-state, which is formed by Type I vertices, as already discussed previously. Small ground state areas formed by Type I vertices, surrounded by a large amount of Type II and III

vertices that increase the total energy of the system, and even few highly energetic Type IV vertices form the magnetization states observed after applying this demagnetization protocol.

Different demagnetization protocols involving applied magnetic fields have also been proposed. One of them determined that the orientation of the axis about which the sample rotates does not affect the energy of the obtained magnetization state [14]. Others explored that a reduction in the energy of the final state, even producing a zero magnetic moment, is obtained when using smaller steps when reducing the magnetic field towards zero [15], and even using magnetic fields maintained at a constant value [16].

The demagnetizing protocol involving applied fields proposed by Wang *et al.* [12] has been followed in this work. The parameters used to carry on the experiments are similar to the ones proposed there: the sample is rotated at 1000rpm while an in-plane magnetic field starting at a value of 1300 Oe is applied, reducing it to 816 Oe in steps of 32.6 Oe, followed by steps of 16.3 Oe until zero applied field is reached, flipping the external field orientation in each step and with a step duration of 1s. The resulting magnetization states have been imaged by means of magnetic force microscopy, and in Figure 7-6 a MFM image over an area of 15x15μm^2 of one of the remanent magnetization states achieved in the artificial spin ice pattern is shown.

In that figure one can immediately appreciate that the state achieved shows short-range ground state ordering, with small regions of Type I vertex surrounded by many Type II and III vertices, and few high-energy type IV vertices. After performing a statistical analysis of the vertex types population in the magnetization state obtained after applying this demagnetization protocol several times on the same sample, the resulting vertex populations are: 48.1±3.7% are Type I vertices, 41.3±2.7% are Type II, 9.2±0.8% are Type III vertices, and finally 1.4±0.3% are Type IV. This means that even if almost half of the vertices in the artificial spin ice pattern are in the lowest energy state and almost 90% of them follow the two in/two out ice rule (Type I and Type II

vertex), the final magnetization state and the total energy after this demagnetizing protocol is applied is still far away from the magnetization state found in as-grown artificial spin ice structures (which is shown in Figure 7-8, in the next section). These results will be compared with the ones obtained after applying a thermal annealing demagnetization protocol, which is discussed hereafter.

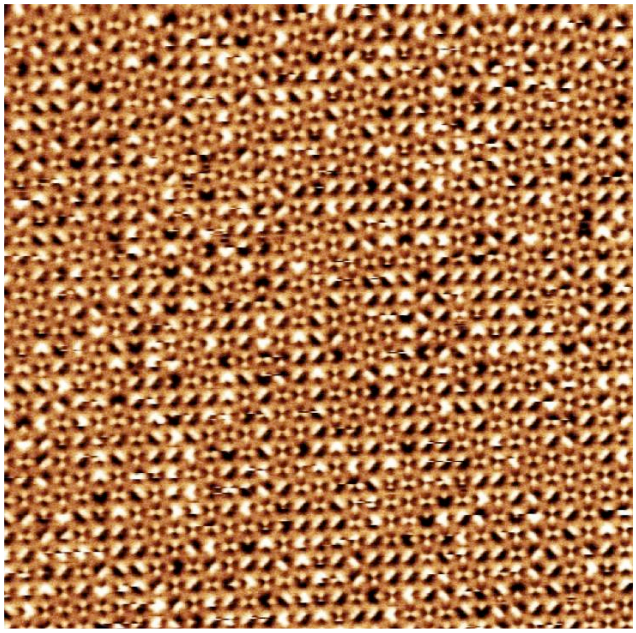

Figure 7-6: 15x15 µm2 image of the square artificial spin ice pattern after applying an in-plane AC magetic field rotating demagnetization protocol, showing short-range ground state regions.

7.2.3.2. Thermal demagnetization

An alternative to the demagnetizing protocols involving external magnetic fields is to anneal the artificial spin ice pattern above its blocking temperature, regime in which the nanomagnets composing the array are superparamagnetic and upon cooling down from above T_B they freeze in the minimum energy state that can be achieved. This procedure has been tried in artificial spin ice samples made of conventional Permalloy ($Ni_{80}Fe_{20}$), but as previously mentioned, the blocking temperature is so high that the sample is destroyed upon heating above it. Hereafter, a different material ($Ni_{87}Fe_{13}$) with a lower blocking temperature

has been used to create the artificial spin ice sample discussed previously in this chapter, so that the annealing process above T_B does not destroy the pattern while the demagnetization process takes place.

From Eq.(7-1), which can be cast in the following form, the blocking temperature of the nanomagnets can be evaluated as follows:

$$ln\left(\frac{1}{t_0}\right)k_B T_B = \frac{1}{2}\mu_0 M_S^2(T_B)\Delta N \cdot V \qquad (7\text{-}4)$$

where the temperature dependence of M_S used in the expression for the shape anisotropy is taken from the experimental data shown in Figure 7-2, and t_m=1 considering that the typical heating and cooling rates used in these experiments are about 1K/s. The other parameters are ΔN=0.146, calculated using the expressions given in [17], and V≈7.5x10^{-22}m^3 is the volume of the nanomagnets. This equation is solved graphically in Figure 7-7, which shows that the intersection between the thermal energy activation term (the first term in Eq.(7-4)) and the shape anisotropy energy (the second term in Eq.(7-4)) occurs at T_B=765K. At this temperature the saturation magnetization has a value of M_S(T=765K)=90.5x10^{3}A/m. This value of the magnetization is used to evaluate the dipolar magnetostatic energies at the blocking temperature of each of the four degenerate groups of vertex types, from Type I to Type IV, that were previously discussed.

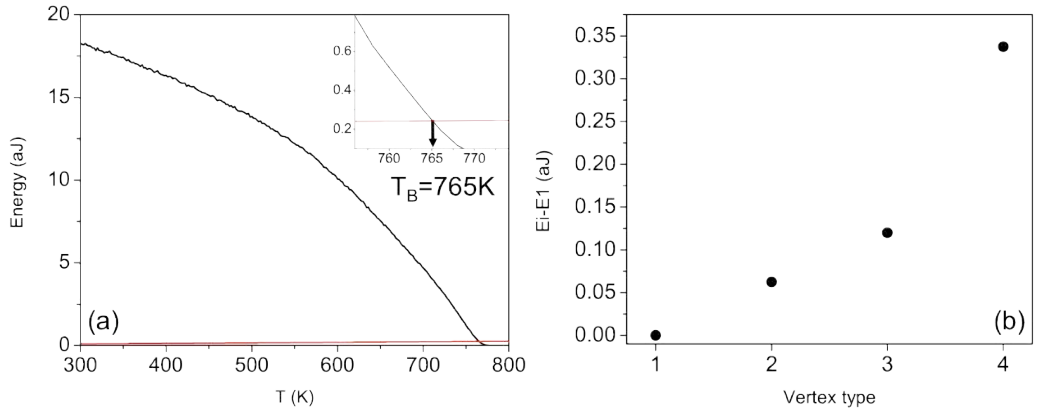

Figure 7-7: shape anisotropy energy (black) and thermal energy k_BT (red) as a function of temperature, with the inset showing the critical temperature zone, with the blocking temperature of the nanomagnets made of $Ni_{87}Fe_{13}$ marked (a). Vertex energy differences (E_i-E_1) as a function of the vertex type at T_B=765K (b).

Each of the vertex energies was calculated by means of the OOMMF micromagnetics simulation plattform [18], for which a simulation unit comprising four nanoislands forming a vertex with the value of M_S specified above with the orientation of the magnetization set according to each vertex type was used, with a cell size of 5nm side, which is lower than the exchange length of permalloy (5.3nm) used as a reference also for our alloy, whose value will not differ much from that one. The four total magnetostatic energies (demagnetizing energy plus magnetostatic dipolar interaction energy) obtained are 0.79, 0.852, 0.91 and 1.127aJ on going from the Type I to the Type IV vertex, and their differences with the Type I vertex have been plotted in Figure 7-7. By bringing the artificial spin ice system above the Curie temperature, the remagnetizing process during the cooling down across the blocking temperature should occur as follows: initially, just below the Curie temperature, the four vertex-type configurations would be equally populated since the value of the magnetization at that temperature is almost zero and, therefore, the dipolar interactions among the nanomagnets are negligible, viz. all 16 vertex-type configuration are degenerate. As the temperature is reduced from T_C approaching the blocking temperature, M_S increases and so do the dipolar interactions, gradually removing the degeneracy of the four vertex configurations. Hence, a progressive depopulation of the high-energy states is expected, as the thermal energy will favor unidirectional jumps overcoming the shape anisotropy barrier in one direction, from one energy state to another with lower energy. The reverse process will become more and more unlikely, as in order to jump from a less energetic vertex state to the next higher energetic one the activation energy is higher than that due to the shape anisotropy barrier (the only one to overcome in the downward channel), because of the additional positive energy difference between the two vertex-type configurations. Eventually, as T_B is being approached, the energy difference between the different vertex types becomes so large that the upward channel freezes before all thermal jumps become impossible (i.e. below T_B). To realize this the energies plotted in Figure 7-7 can be analyzed in detail. At T_B the energy difference between Type II and Type II vertices is around 0.063aJ, which corresponds to 390meV. The energy difference

between Type III and Type I vertices is 750meV, and between Type IV and Type I vertices 2.113meV. These energy differences are compared with a Boltzmann energy term K_BT of only 66meV at the blocking temperature. Based on these assumptions, when cooling down the artificial spin ice sample from above T_C, below T_B a final state with only Type I vertices should be expected to be found frozen in the sample, corresponding to the ground-state of the artificial spin ice system.

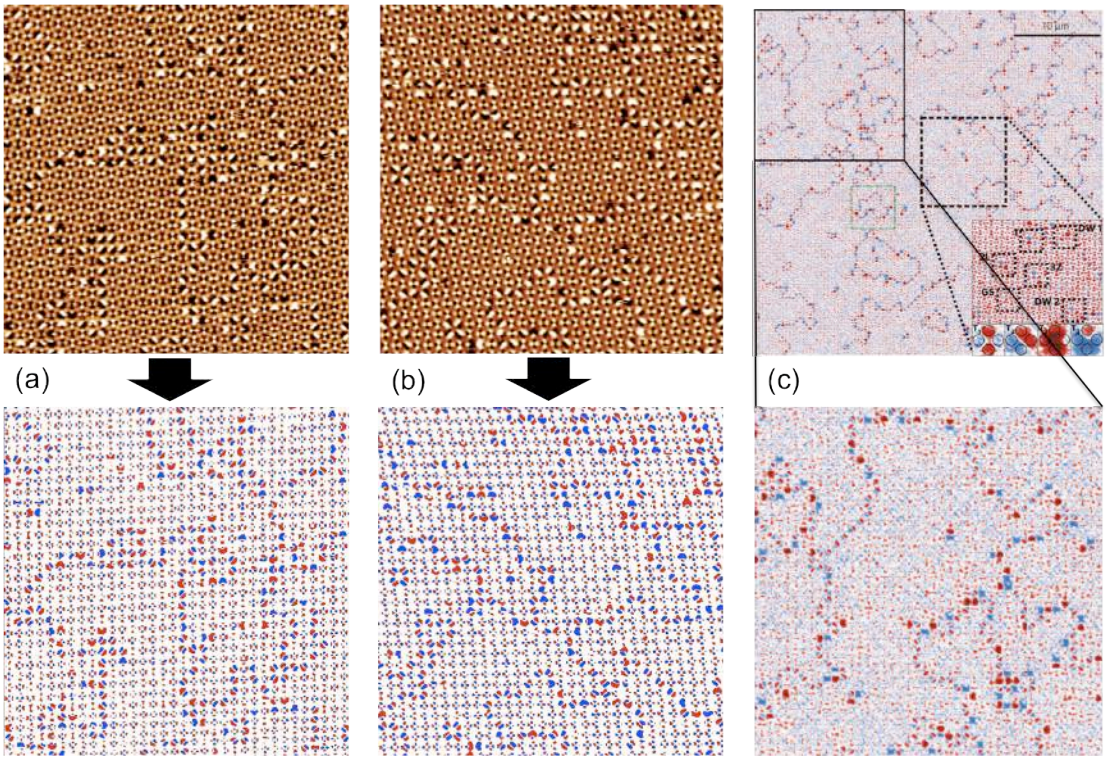

Figure 7-8: 15x15μm² MFM images of two regions of the square artificial spin ice pattern after applying thermal annealing demagnetization protocols heating the pattern above its blocking temperature ((a) and (b)) showing long-range ground-state regions separated by Type II and III vertex chains. The lower panels correspond to the MFM images shown above them with the color code used in [6], to compare them with the as-grown magnetization state obtained in [6], which is observed in (c). A zoomed-in 15x15μm² MFM image region is shown in the lower panel of (c) for a side-to-side comparison with the ones observed in (a) and (b) after applying the thermal annealing demagnetization protocol proposed here.

This thermal demagnetizing protocol was repeatedly performed in the artificial spin ice sample, annealing it to a temperature around 800K, above both the Curie and the blocking temperatures, and cooling it down to room temperature at a cooling rate of 1K/s. The resulting magnetization states after the thermal annealing processes were investigated by means of magnetic force microscopy,

and two 15x15μm^2 MFM images of the frozen-in demagnetized states are shown in Figure 7-8.

Two 15x15 μm^2 Magnetic Force Microscopy images of the frozen in demagnetized states are shown in Figure 7-8. As it can be seen from Figure 7-8(a) and Figure 7-8(b) the room temperature magnetization distribution shows a long-range ground-state ordering of the artificial spin ice magnetic moments, comparable to the ones obtained in the as-grown state and studied by Morgan *et al.* in [6]. To better appreciate the similarity of the resulting configurations, in the lower panels of Figure 7-8(a) and Figure 7-8(b) we display the MFM images in the corresponding upper panels using the same contrast color scheme used in [6] and compare the image with that obtained in that work, which is shown in Figure 7-8(c). The lower panel of Figure 7-8(c) shows a zoomed-in region of the as-grown state observed in [6] over an area with a similar size of that shown in Figure 7-8(a) and Figure 7-8(b), for side-to-side comparison purposes. A visual comparison between Figure 7-8(a) and Figure 7-8(c) shows some differences in the domain boundaries between the ground-state regions. Nevertheless, if we image a different region of the sample, as shown in Figure 7-8(b), these domain boundaries are more similar to those displayed in Figure 7-8(c). Similar variations of the domain boundary structure are also reported by Morgan *et al.* in the supplementary information given in [6], and can be most likely due to a random distribution of the islands' imperfections.

After applying this thermal demagnetizing protocol several times, the resulting magnetization states analyzed via magnetic force microscopy show always similar results. A statistical analysis of the vertex-type populations gives the following results: 74.3±4.2% of the vertices were of Type I, 20.1±2.0% were of Type II, and only 5.6±2.1% of Type III. We did not observe a single vertex in a Type IV configuration, whilst some of them can be found in the as-grown state presented by Morgan *et al.* in [6], which is a remarkable difference between our approach and the one presented in [6]. This means that this thermal annealing demagnetization protocol is an approach to reach the ground-state in artificial spin ice samples that yields even better results than that of observing the as-

grown magnetization state right after the fabrication of the sample, and is by far more reliable than the demagnetization protocols that involve applying external magnetic fields.

7.2.4. 'Domain wall' boundaries formation

Based on the analysis performed above about the remagnetization process occurring during the thermal annealing demagnetization above the blocking temperature, and by looking at the energies of each vertex state at temperatures around T_B, in a perfect sample this annealing process should, in principle, lead to the formation of a final magnetization state formed only by the lowest vertex energy states; i.e., Type I vertices, which is the ground-state of the square artificial spin ice pattern. A possible explanation for the discrepancy between this ground state, formed only by Type I vertices, and what is observed after applying the thermal demagnetization protocol proposed here can be traced to the intrinsic unavoidable defects during the nanofabrication process, which always yields a size and shape distribution on the nanomagnets composing the artificial spin ice array, so that not all the nanomagnets are identical, which means that there will be a distribution of blocking temperatures [19].

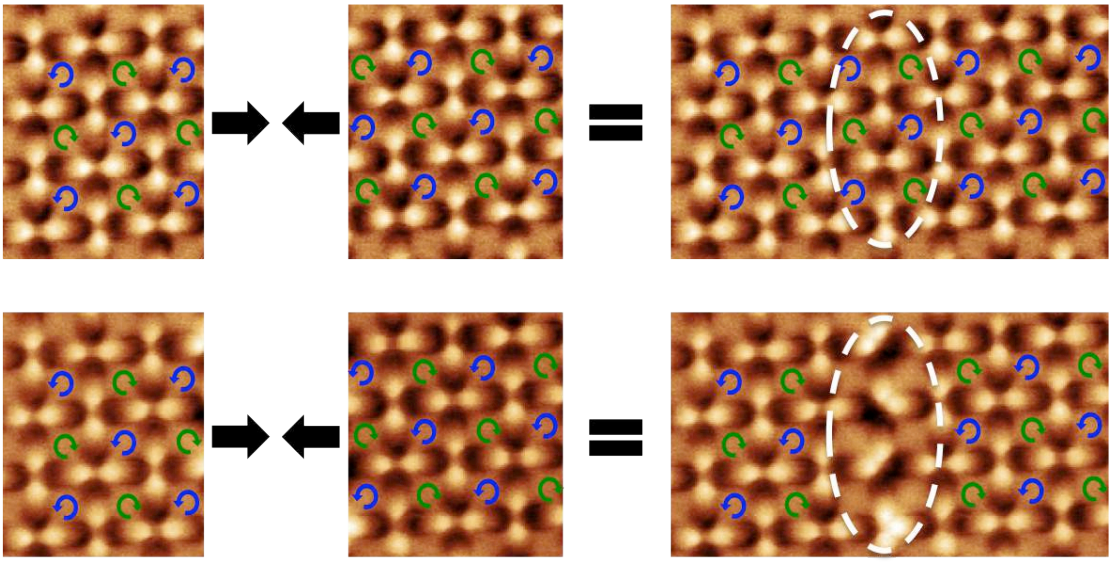

Figure 7-9: formation of large ground state regions after the thermal demagnetization protocol when two opposite chirality Type I vertex regions merge (up), and formation of a 'domain wall' region (marked with a dashed line) with Type II and Type II vertices when two Type I vertex regions with the same chirality merge (down).

During the cooling, the distribution of T_B would lead to the nucleation and freezing of ground-state ordered regions in different portions of the sample, those with higher T_B. These initially frozen regions will be a seed of ground-state order at their boundary causing their progressive expansion as T decreases further. It can be noted by inspection of the magnetic force microscopy image in Figure 7-8(a) or Figure 7-8(b) that in the areas of ground-state ordering, Type I vertices alternates with opposite chirality along horizontal and vertical lines, as sketched in Figure 7-9. When two (or more) of these regions come together, they can merge forming a unique broader region if the chirality of the vertices at their border matches or, in case there is no matching, a boundary of Type II and/or Type III vertices is formed, as schematically shown in the lower panel of Figure 7-9. This process shares many similarities with the remagnetization process of a sample via magnetic domains formation and expansion.

The final result would be a series of ground-state 'domains' of Type I vertices separated by 'domain walls' made predominantly by Type II vertices with some 'defects' of Type III, as can indeed be recurrently observed in the obtained MFM images. The quite broad domain size distribution observed in the MFM images could be due to the fact that the freezing temperature window is very narrow, so that during the cooling the system might not have enough time to fluctuate out the smaller domains.

7.3. Conclusions

After applying two different demagnetizing protocols to the square artificial spin ice sample it is interesting to compare the resulting statistical analysis of the vertex populations in both cases, which can be observed in Figure 7-10.

The vertex populations plot shown in Figure 7-10 state that the reliability of the thermal demagnetization protocol is much higher compared to what is observed in the same sample after applying demagnetization protocols involving externally applied fields already proposed in literature.

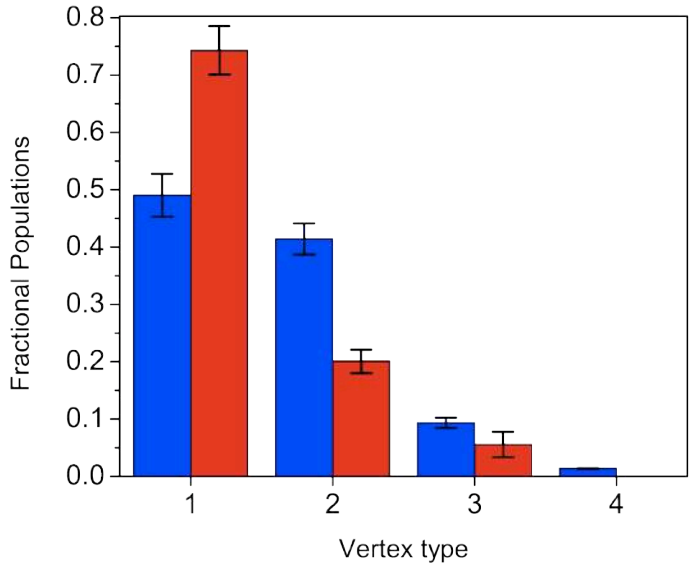

Figure 7-10: bar plot showing the vertex populations for each demagnetization protocol. The resulting vertex populations from the in-plane AC magnetic field rotating demagnetization protocol are shown in blue, and the resulting vertex populations from the thermal annealing demagnetization protocol are shown in red.

Following this methodology proposed here with this new thermal annealing demagnetization protocol it is now possible, for example, to provide a solid experimental base for theoretical studies performed on the thermalization of artificial spin ice patterns [20]. Also, by varying the cooling rate or by performing several minor temperature loops, changing for instance the maximum temperature reached at each loop, one can investigate the formation and the structure of the Type II and III 'domain wall' boundaries between ground-state ordering domains as well as domain size distribution versus cooling rate.

Another possible experiment to be performed with this thermal demagnetization protocol is the study of how defects and vacancies of single nanomagnets in an artificial spin ice pattern lead to the formation of the ground-state ordering, as an experimental verification of what is presented in [19]. Since this approach works independently of the island volume, one can also study how the variation of the thickness of the nanomagnets, namely the strength of the dipolar interaction, affects the final ground-state ordering obtained after applying the thermal demagnetization protocol. A quick estimate of the dipolar energy term

given by $\left(M_S(T_B)\cdot t\right)^2$ as a function of the thickness indicates that the dipolar interaction strength increases as the thickness is increased.

Novel and intringuing physical properties related to the presence of long-range ground-state ordering in artificial spin ice systems can be also studied, as this thermal demagnetization protocol gives the possibility to study how the formation of these long-range ground state areas are formed repetitively. Among these novel physical properties the physics of the formation and propagation of magnetic monopole excitations and Dirac strings [6, 21, 22] emerge as key issues to be studied.

It is worth mentioning, to conclude, that the approach described here [23] is general and not limited to the actual material employed here, viz., $Ni_{87}Fe_{13}$, but it can be implemented using other materials. For instance pure Ni has a T_C of 673K, about 100K lower than the alloy proposed here. The utilization of *Ni*, or more in general any other ferromagnetic material with a sufficiently low T_C, would allow an implementation of this approach. For specific materials, it could even allow performing the thermal demagnetization while directly observing the sample with the MFM (the MFM present in nanoGUNE is equipped with a thermal stage, being able to perform MFM imaging in samples heated up to 600K).

7.4. References

[1] L. Pauling, *J. Am. Chem. Soc*. **57**, 2680 (1935)

[2] S. T. Bramwell and M. J. P. Gingras, *Science* **294**, 1495 (2001)

[3] M. J. Harris, S. T. Bramwell, D. F McMorrow, T. Zeiske and K. W. Godfrey, *Phys. Rev. Lett.* **79**, 2554 (1997)

[4] R. F. Wang *et al., Nature* **439**, 303 (2006)

[5] L. A. S. Mól, A. R. Pereira and W. A. Moura-Melo, *Phys. Rev. B* **85**, 184410 (2012)

[6] J. P. Morgan, A. Stein, S. Langridge and C. H. Marrows, *Nat. Phys*. **7**, 75 (2011)

[7] A. Remhof, A. Schumann, A. Westphalen and H. Zabel, *Phys. Rev. B* **77**, 134409 (2008)

[8] S. Ladak, D. E. Read, G. K. Perkins, L. F. Cohen and W. R. Branford, *Nat. Phys*. **6**, 359-363 (2010)

[9] E. Mengotti, L. J. Heyderman, A. Fraile Rodriguez, F. Nolting, R. V. Hügli and H. B. Braun, *Nat. Phys.* **7**, 68-74 (2011)

[10] L. Néel, *Ann. Geophys*. **5**, 99-136 (1949)

[11] H-B Braun, *Adv. Phys*. **61**, 1 (2012)

[12] R. F. Wang *et al.*, *J. Appl. Phys*. **101**, 09J104 (2007)

[13] K. J. Miller, M. Sofman, K. McNerny and M McHenry, *J. Appl. Phys*. **107**, 09A305 (2010)

[14] E. Mengotti, L. J. Heyderman, A. Fraile Rodríguez, A- Bisig, L. Le Guyader, F. Nolting and H. B. Braun, *Phys. Rev. B* **78**, 144402 (2008)

[15] X. Ke, J. Li, C. Nisoli, P. E. Lammert, W. McConville, R. F. Wang, V. H. Crespi and P. Schiffer, *Phys. Rev. Lett.* **101**, 037205 (2008)

[16] Z. Budrikis, P. Politi and R. L. Stamps, *Phys. Rev. Lett.* **105**, 017201 (2010)

[17] J. A. Osborn, *Phys. Rev*. **67**, 351-7 (1945)

[18] OOMMF code made by NIST, http://math.nist.gov/oommf/

[19] R. C. Silva, R. J. C. Lopes, L. A. S. Mól, W. A. Moura-Melo, G. M. Wysin and R. Pereira, *Phys. Rev. B* **87**, 014414 (2013)

[20] Z. Budrikis, K. L. Livesey, J. P. Morgan, J. Akerman, A. Stein, S. Langridge, C. H. Marrows and R. L. Stamps, *New. J. Phys*. **14**, 035014 (2012)

[21] S. Ladak, S. K. Walton, K. Zeissler, T. Tyliszczak, D. E. Read, W. R. Branford and L. F. Cohen, *New. J. Phys*. **14**, 045010 (2012)

[22] F. S. Nascimento, L. A. S. Mól, W. Moura-Melo and A. R. Pereira, *New. J. Phys*. **14**, 115019 (2012)

[23] J. M. Porro, A. Bedoya-Pinto, A. Berger and P. Vavassori, *New. J. Phys.* **15**, 055012 (2013)

8. Domain wall displacement in nanostripes for the generation of ultrafast magnetic field pulses

8.1. Introduction

8.1.1. Domain wall displacement in nanostripes

In recent years the magnetization reversal processes and their dynamics at the nanoscale have been intensively studied in nanostructured magnetic materials. This development can be achieved mainly due to the new nanofabrication and characterization methods that allow accessing new regimes in size and time resolution scales. At the same time, our limited knowledge of the magnetization dynamics in these regimes needs to be expanded to implement magnetic devices. Despite all past and present research efforts there are still many open questions and challenges that need to be solved in order to fully understand and control magnetism on very small length and very fast time scales. In static magnetic properties many different well-developed techniques are available that can provide very detailed results, against which theoretical models and their predictions can be tested. In dynamic magnetic phenomena direct experimentation can be expected to stimulate the development of future refined theoretical descriptions. Besides this, in applications such as magnetic data storage the fundamental and technical limitations that control the ultimate time scale for reading and writing magnetic information by means of nanoscaled device elements need to be further developed.

When studying thin-film magnetic nanostructures, which are the main interest for applications, high-speed measurements of the magnetization dynamics can be performed by means of sub-nanosecond magneto-optic sampling techniques [1,2]. Nevertheless, generating intense and fast magnetic field pulses to be used in such studies is still a difficult experimental challenge. Up to now the

experiments performed on this field are based in short electrical pulses injected in microstrip transmission lines made of materials such as Au, Cu or Al, fabricated by means of optical lithography [3-10] or focused ion-beam lithography [11]. A straight strip-line generates a magnetic field in the plane of the sample perpendicular to the current direction. If the strip-line is nanofabricated so that it forms micro-coils, it creates a magnetic field perpendicular to the sample plane, as the one observed in Figure 8-1.

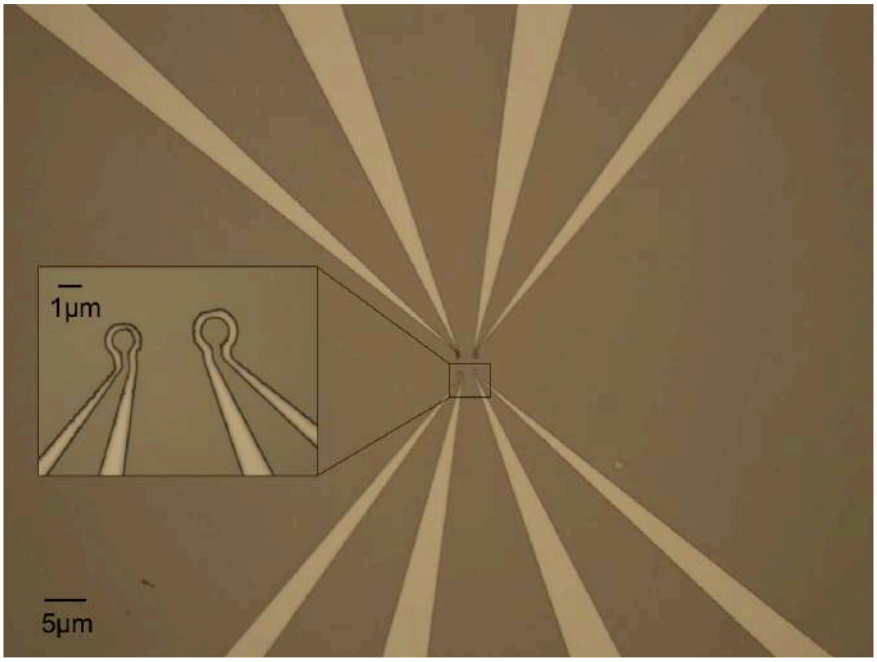

Figure 8-1: Optical microscope image of microcoils made of Permalloy to generate or sense magnetic fields perpendicular to the coils plane.

Generally, these strip-line magnetic devices are able to generate in-plane and out-of-plane fast and weak magnetic fields: field pulse durations below 100ps have been reported, with a estimated maximum field amplitude of 1 kOe, even though the values reported in the literature are always below 0.2 kOe. This kind of magnetic field pulses, with that intensity and speed, can be used to excite a detectable magnetization dynamic process in soft magnetic nanoelements, but they are not able to trigger a magnetization dynamics process in hard magnetic nanoelements, which are of key importance for applications. The absence of high intensity magnetic field pulses sources is a big problem, due to the fact that only hard magnetic materials retain their ferromagnetic nature at decreasing length

scales, because the lower activation barrier for magnetization reversal events in soft magnetic materials will lead to a superparamagnetic regime at the nanoscale.

In this chapter a different pathway to generate intense and fast magnetic field pulses to study the magnetization dynamics of nanostructures is proposed. Planar conduits (nanostripes) are used to propagate domain walls, whose displacement creates magnetic field pulses that affect the magnetization of magnetic nanoparticles that are placed in the proximities of the nanostripe, as can be observed in Figure 8-2.

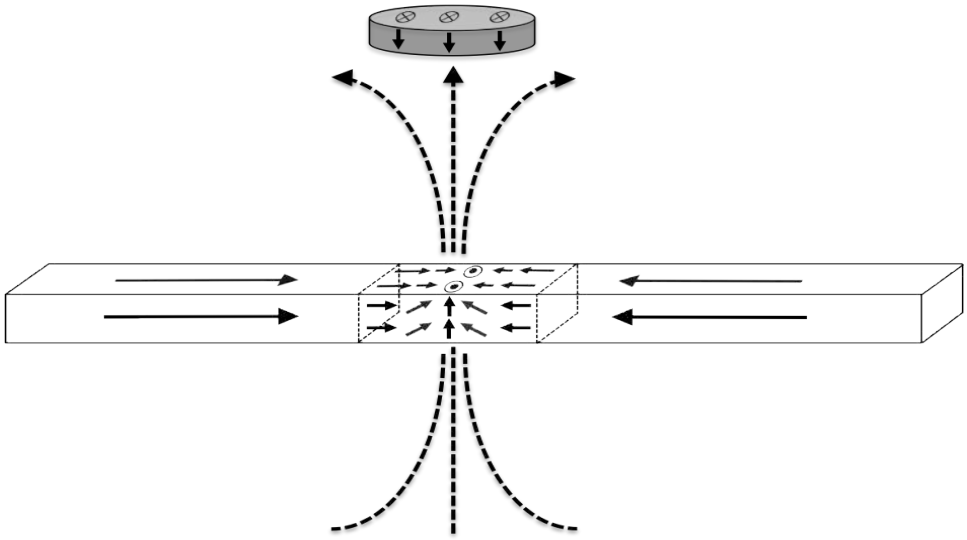

Figure 8-2: a domain wall in the center of a nanostripe being displaced from one edge towards the opposite one while it generates an intense magnetic field pulse in its proximities, which can be used to induce a magnetization reversal process in neighboring magnetic nanoparticles.

The approach exploits the fact that the magnetic domain walls can produce magnetic field pulses as intense as up to 2 KOe. Due to their extremely confined geometry and the fast displacement velocities that can be obtained with these confined geometries, intense magnetic field pulses in the sub-nm regime are produced by the domain walls. The movement of magnetic domain walls in geometrically confined nanostripes in which the magnetization structure of a domain wall can be controlled via the lateral dimensions and thickness of the nanostripe has been the objective of many recent theoretical [12-19] and experimental [20-26] studies.

The so-called domain wall conduits are defined as thin magnetic stripes in which the magnetic field required to depin a domain wall (H_D, depinning field), previously nucleated at a certain position in the conduit, is bigger than the field required to create the domain wall inside the nanostripe (H_N, nucleating field). Usually these nanostructured materials are micro and nanostripes, where the domain walls can be generated using different geometries. One example is a stripe with an injection pad on one edge [27, 28], as is the case of the nanostripes observed in Figure 8-3, where the differences on the switching fields of the injection pad and the stripe allow to generate a domain wall in between them by applying external fields. Another possibility is to directly nucleate the domain wall in a pre-defined location of the stripe by using externally applied magnetic fields [29, 30] using the geometry of the stripe. After the domain wall is nucleated, it can be displaced between pinning points defined by the geometry of the stripe, so that a full control over the displacement of the domain wall is achieved.

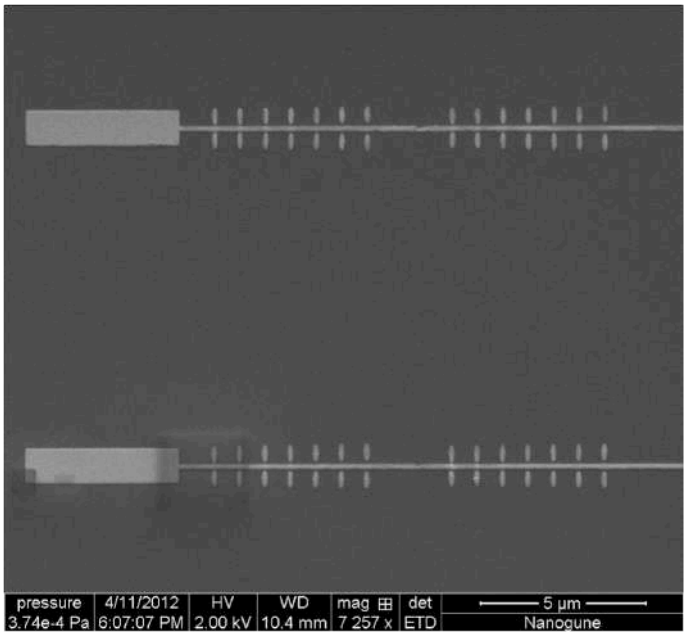

Figure 8-3: SEM image of two domain wall conduits with rectangular injection pads at their left edges, with a pinning point (geometrical indentation) in the center of the conduits, and with neighboring nanoislands in their proximities.

The main interest shown by the scientific community studying domain walls in magnetic nanostripes has been to understand the magnetization dynamics of the domain walls themselves, together with the possibility to have the domain walls easily injected in a nanostripe and to manipulate them between pinning points determined by the geometry of the nanostructure using externally applied magnetic fields and/or spin-polarized currents. All these key points are also related to the enormous potential that this field has to implement domain wall-based devices in technological applications that include magnetic ramdom access memories (MRAM) [31] and logic devices [32]. Besides these, domain wall conduits have also been used in biomagnetic systems, where the controlled motion of a domain wall in a nanostripe is used to deliver biomolecules with a magnetic radical, which are attached to the domain wall due to the field pulse that is generated by the domain wall [33, 34]. This kind of systems has also been implemented in flexible substrates, such as PDMS, allowing bending of the nanostripes without changing their properties [35,36].

8.2. Description of the experiment

8.2.1. Sample description, domain wall injection & displacement

As previously described, the aim of this experiment is to displace a magnetic domain wall through a planar nanostripe in order to study the effect produced by the stray field generated by the domain wall on the magnetization of ferromagnetic nanoislands located in the proximities of the nanostripe. In order to study this effect a perfect control over the domain wall displacements occurring in the nanostripe, often called domain wall conduit (when fulfilling the previously discussed condition for domain wall conduits) in this research field, is needed. For that purpose, different geometries for the domain wall conduit have been studied. The first studied nanostructured domain wall conduit consisted of planar and straight domain wall conduits with a big rectangular injection pad on one edge, so that this injection pad reverses its magnetization while applying an external magnetic field that leaves the magnetization in the rest of the conduit

unaltered. In this way, a domain wall is nucleated in the junction between this rectangular injection pad and the narrow domain wall conduit. The magnetic field needed to depin and displace the domain wall over the long conduit is reduced compared to the magnetic field required to reverse the magnetization in a domain wall conduit without the injection pad, according to [12]. Domain wall conduits 150nm wide, 13nm thick and 12μm long with an injection pad 4μm long and 1μm wide made of Permalloy were fabricated, and the resulting nanostructures can be observed in Figure 8-4.

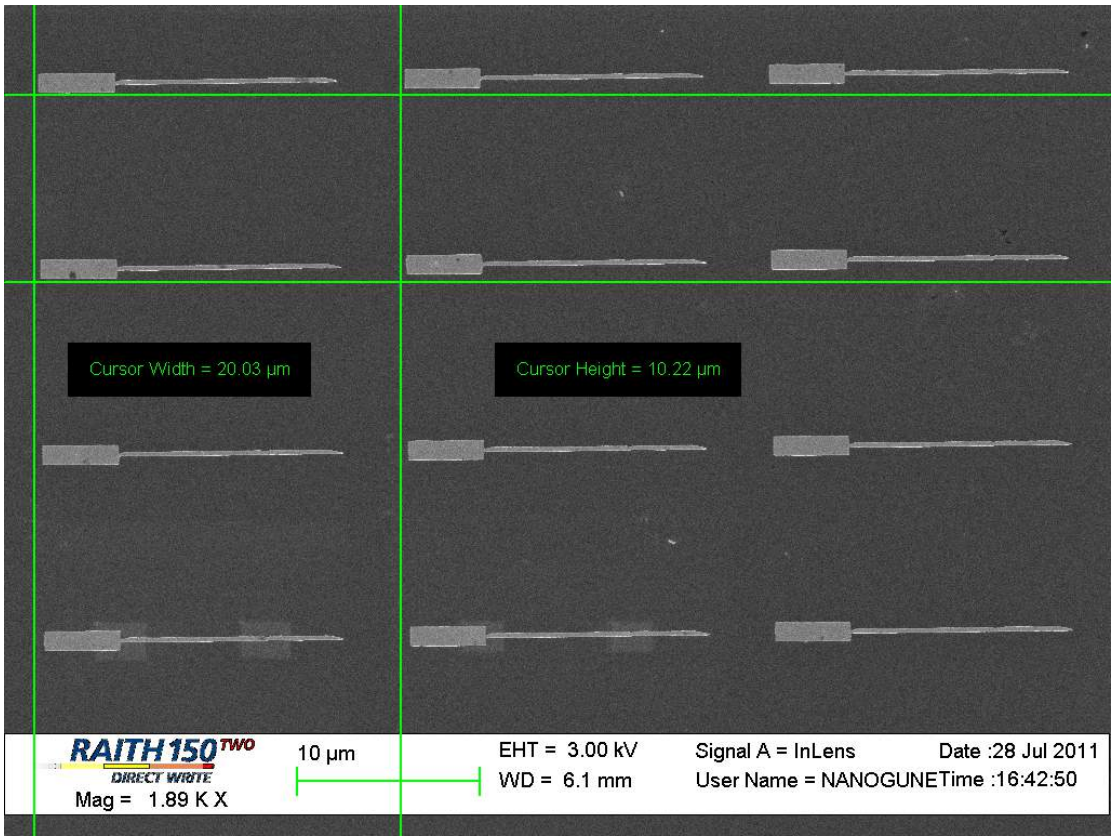

Figure 8-4: Domain wall conduit with an injection pad at one of its edges.

For these nanostructures the injection and displacement of a domain wall was studied, finding that, according to what is observed in our samples and previously reported in [12], when analyzing the magnetization reversal process it is observed that it takes place in well-defined steps, schematized in Figure 8-5(a). Firstly, when applying an external field parallel to the long axis of the conduit, starting from negative saturation, the domain wall conduit is uniformly magnetized following the external field (situation 1 in Figure 8-5(a)). At a certain

field value a domain wall is nucleated in the boundary between the big rectangular injection pad and the narrow nanostripe (situation 2 in Figure 8-5(a)). Finally, the domain wall depinning event from that position occurs by increasing the externally applied field, magnetizing uniformly the domain wall conduit again (situation 3 in Figure 8-5(a)). In the specific case of the nanostructures studied here, the domain wall nucleation event takes place when the external magnetic field reaches a value of 45 Oe, whereas the depinning event happens for a magnetic field value of 75 Oe. This magnetic behavior was analyzed using a Kerr effect microscope with sub-micrometer spatial resolution, which allows recording hysteresis loops from a desired region of the sample by making use of the 'region of interest' tool, as described in Chapter 5 of this thesis. The hysteresis loop recorded from one of the nanostripes shown in Figure 8-4 is shown in Figure 8-5(b), which is just one hysteresis loop recorded out of many more made on different nanostructures that show similar injection and depinning magnetic field values.

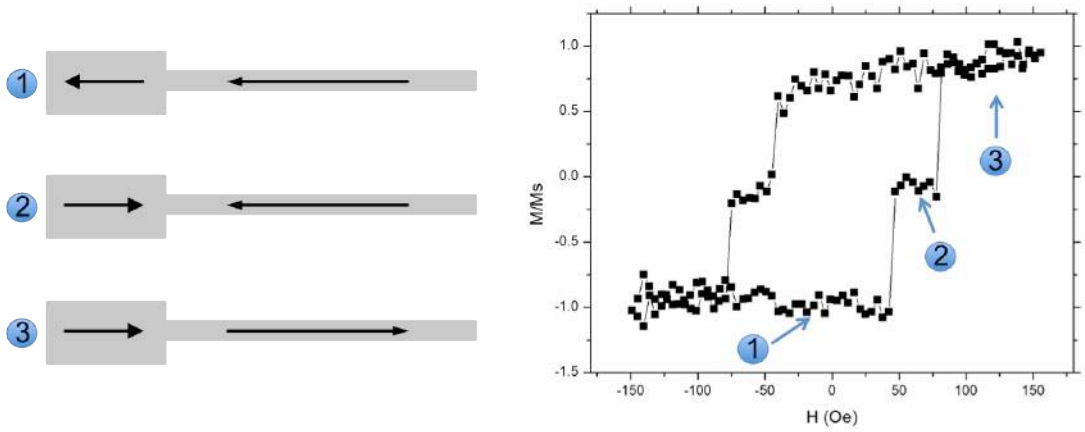

Figure 8-5: magnetization behavior in the nanostructure schematized with arrows indicating magnetization direction (left), with the hysteresis loop recorded on one of the nanostructures shown in Figure 8-4 (right).

The first big jump in the hysteresis loop when coming from positive or negative saturation is due to the magnetization reversal of the injection pads (corresponding to the previously mentioned 45 Oe, situation 2 in Figure 8-5(b)), whereas the second big jump gives account for the depinning event of the domain wall, being displaced from one edge towards the other one, hereby reversing the magnetization of the narrow domain wall conduit (at a magnetic

field of 75 Oe, (situation 3 in Figure 8-5(b)) and completing the magnetization reversal process in the nanostripe.

Besides this geometry for the domain wall conduits, a different one has also been studied. It consists of a similar narrow domain wall conduit but, instead of using a rectangular injection pad, a curved conduit with the same width of the domain wall conduit is attached to one of its edges. One of the nanostructures fabricated with this shape can be observed in Figure 8-6.

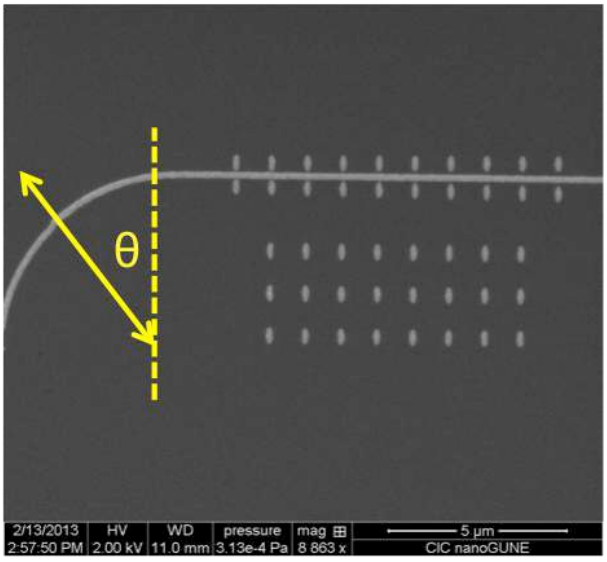

Figure 8-6: Domain wall conduit with a curved section used to nucleate the domain wall in the conduit by applying an external field at an angle from the dashed line. The nanoislands adjacent to the conduit are placed at a distances ranging from 50nm to 100nm from it, and the nanoislands far below the conduit are used as "control nanoislands" whose magnetization is only affected by the externally applied fields.

In this domain wall conduit the nucleation of a domain wall is performed by applying an external field (H_N) at an angle θ from the vertical direction (see sketch in Figure 8-6); if the externally applied field is negative (applied downwards), a tail-to-tail domain wall will be nucleated in the curved conduit whereas if the applied field is positive (applied upwards) a head-to-head domain wall will be nucleated (sketched in Figure 8-7(c)). Due to the curvature of the conduit [37] the nucleated domain wall will remain at the position where it has been nucleated until an external magnetic field is applied along a suitable direction to displace it (H_D).

There are many differences between the two proposed domain wall conduits (rectangular injection pad and curved domain wall conduit section). The main one is that in the case of the rectangular injection pad, the nucleation and depinning of the domain wall occur at the same position (frontier between the narrow conduit and the injection pad), and the depinning field is unique, defined in each conduit. On the contrary, in the curved conduit the angle θ at which the external field is applied determines both the nucleation position of the domain wall and the depinning field intensity needed to displace the domain wall from that position. Depending on the angle at which the nucleating field is applied, the depinning field changes. An analysis of the dependence of the depinning field with the angle at which the nucleating field is applied in the conduit is shown in Figure 8-6.

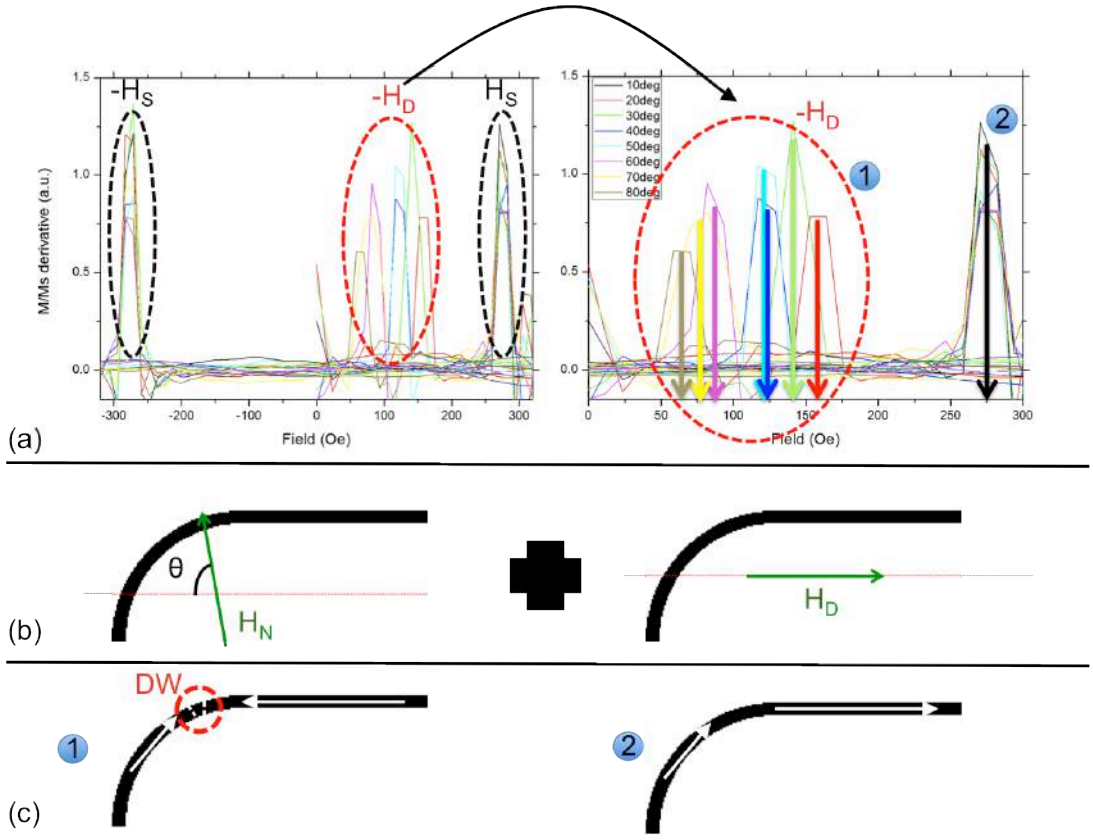

Figure 8-7: (a) dM/dH curves, as a function of H, of the domain wall conduits recorded applying an external field starting from zero field towards positive saturation, negative saturation, back to positive saturation. The black dotted lines are the magnetization jumps due to the magnetization reversal of the conduit when no domain wall has been nucleated (first step in (b) did not occur), and the red dotted line (zoomed in on the right hand side of the figure) correspond to the depinning fields of the domain wall after nucleating it at an angle θ. (b) Field sequence: nucleating field at an angle θ+depinning field. (c) Sketches of the magnetization states 1 ($H_N<H<H_D$) and 2 ($H>H_D$).

In order to analyze the nucleation and depinning events on the curved conduit hysteresis loops have been recorded with the 'region of interest' tool of the Kerr microscope. A nucleation field H_N=*600 Oe* is applied at an angle θ, directed as inficated in Figure 8-7(b), and after nucleating the domain wall hysteresis loops on the straight part of the domain wall conduit are measured with the following field sequence: starting from zero field positive saturation is reached, then the field is decreased towards negative saturation, and the measurement is finished by coming back to positive saturating external fields. This sequence has been repeated 10 times after applying the nucleating field at different angles from 10° to 80°. Due to the fact that the measurements are performed on individual domain wall conduits, whose dimensions are below the optical resolution limit for the Kerr microscope, the recorded hysteresis loops are noisy and, in order to observe the magnetization jumps better, *dM/dH* has been computed and the resulting curves *dM/dH* as a function of *H* are shown in Figure 8-7(a).

One can easily observe that each of the *dM/dH* curves has three peaks (sketched with the two black and the red dotted lines in the left panel of Figure 8-7(a)): the first peak corresponds to a magnetization jump (red dotted line) observed when the external field reaches the depinning field value (H_D) The different values of H_D obtained changing θ confirm that the depinning field value depends on the angle at which the nucleation field is applied. It is the transition point between points 1 and 2 sketched in Figure 8-7. The second and third magnetization jumps (black dotted line) correspond to the magnetization switching fields (H_S) of the straight conduit when no domain wall has been previously nucleated in the conduit.

Having a deeper look into the depinning fields marked with the red dotted line (a zoomed-in region of that part of the hysteresis loops is shown in the right panel of Figure 8-7(a)), it is observed that the depinning field values decrease when the angle at which the nucleating field is applied increases, meaning that the external field required to depin the domain wall is minimized when the domain wall has been nucleated close to the straight part of the domain wall conduit, as

expected. Therefore, the situation with the smallest depinning field value corresponds to the case when the nucleation field is applied at θ=80°.

A second analysis has been carried out: how the depinning field value changes, after applying the nucleating field at an angle of 80°, when the depinning field is applied at an angle from the parallel to the straight part of the domain wall conduit (sketched in the lower panel of Figure 8-8). Again, this analysis has been performed by using the Kerr microscope, with the 'region of interest' tool focused on the straight part of the domain wall conduit, and the results are shown in Figure 8-8.

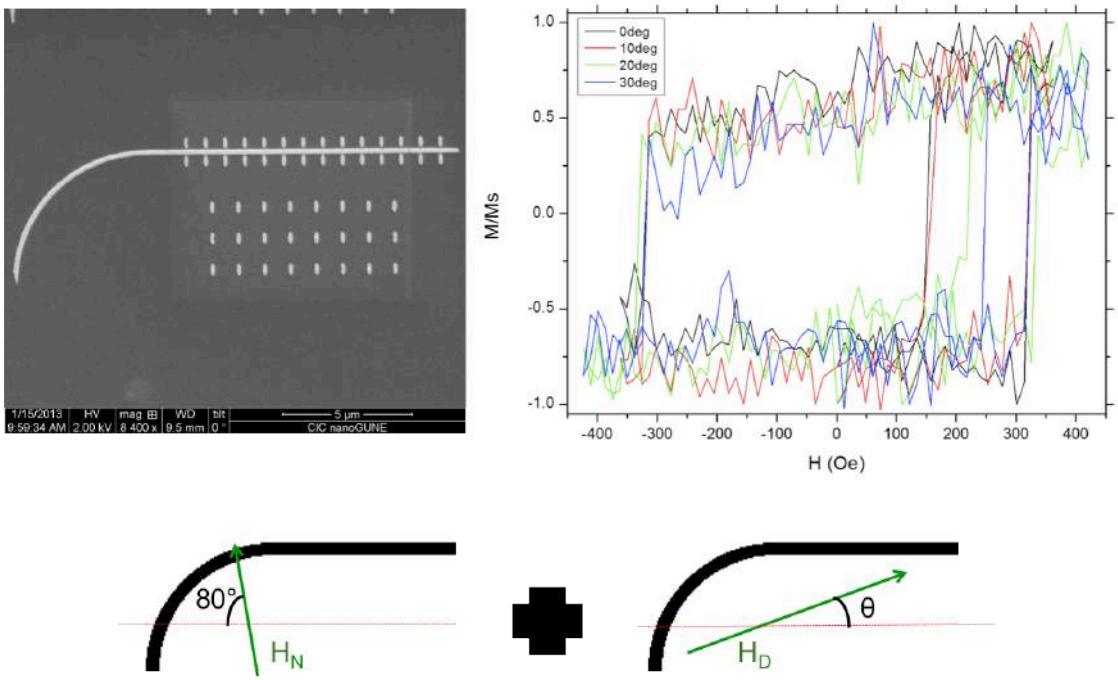

Figure 8-8: SEM image of the sample used for the analysis of the depinning field values, presented in the right panel, when the depinning external field is applied at an angle θ as sketched in the lower panel, after the nucleating field has been applied at an angle of 80° in the conduit shown on the left.

This analysis shows that the depinning field value increases with the angle at which the external field for the depinning event is applied, as observed from the external field values (ranging from H_D*=140 Oe* when the external field angle is 0° to H_D*=250 Oe* when the external field angle is 30°) at which the first jump in the magnetization takes place, which corresponds to the depinning of the domain wall leading to the full magnetization reversal of the conduit.

Note that the depinning field values observed in Figure 8-7 and Figure 8-8 when the depinning field is applied parallel to the conduit are different. This is due to the fact that the results shown in Figure 8-7 have been measured in the conduit of Figure 8-6, and the results of Figure 8-8 correspond to the conduit shown in that image, which is thinner than the previous one, with which the whole set of results shown in the rest of the chapter have been obtained. The sample in Figure 8-6 was fabricated with the distances of the neighboring nanoislands varying from 50 to 100nm, during the nanofabrication process of the final sample, in order to study the smallest possible gap between the nanoislands and the conduit. In the conduit shown in Figure 8-8 all the nanoislands are placed at a distance of 50nm from the conduit.

8.2.2. Nanoislands behavior

Apart from the behavior of the domain wall conduit, knowing the magnetic behavior of the nanoislands that are placed in the proximities of the conduits is a fundamental requirement. For that purpose arrays of non-interacting ferromagnetic nanoislands were fabricated by means of electron-beam lithography, and the magnetic behavior studied by means of MOKE magnetometry and magnetic force microscopy. As discussed in previous chapters, a magnetic nanoellipse may present different magnetization states at remanence; i.e. single domain, vortex, etc. Therefore, in order to simplify the understanding of the possible effects of the stray field generated by the domain wall passing by the conduit on the neighboring nanoellipses, nanoislands that present an Ising-like bistable behavior of the magnetization are used. In this way the magnetic field created by the domain wall is most likely to induce a magnetization reversal process in the nanoisland, which is the main purpose of this study.

Different sizes of elliptical ferromagnetic nanoislands made of Permalloy have been fabricated and analyzed, looking for nanoislands with a bistable behavior of

the magnetization and with a relatively small switching field (so that a magnetization reversal process is more likely to be induced by the stray field of the domain wall). This optimized behavior was found for nanoislands with dimensions 425nm long, 170nm wide and 13nm thick. The nanolithographed pattern of elliptical nanoislands can be observed in the left panel of Figure 8-9.

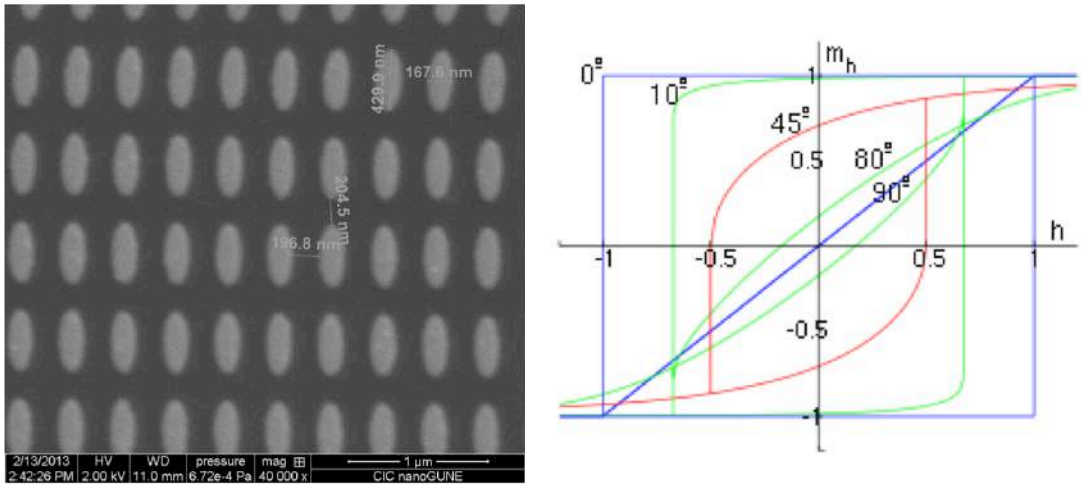

Figure 8-9: SEM image of an array of elliptical ferromagnetic nanoislands made of Permalloy with dimensions 425x170x13nm³(left), and hysteresis loops of a nanoisland following the Stoner-Wohlfarth model when the external field is applied at different angles from its easy axis (right).

In order to understand the magnetization reversal process of ferromagnetic nanoellipses the so-called Stoner-Wohlfarth model [38] is one of the simplest models for studying bistable Ising-like magnetic systems. This model assumes a coherent rotation of the magnetization (which can be represented by a magnetic moment vector for the whole nanoellipse) induced by the external magnetic field, meaning that the exchange energy term will be zero irrespective of the direction at which the external field is applied in the magnetization reversal process. Therefore, for the individual magnetic nanoellipse two energy terms will be contributing to the total free energy of the ellipse, anisotropy (shape) and Zeeman, and the expression for the free energy is:

$$E_{SW} = Ksin^2\alpha - \mu Hcos(\theta - \alpha) \qquad (8\text{-}1)$$

where $\vec{\mu}$ is the magnetization vector of the nanoisland, α is the angle between the $\vec{\mu}$ vector and the easy axis of the nanoisland, θ is the angle between the applied

field direction and the easy axis, *H is* the value of the applied external field and $K = \frac{1}{2}\mu_0 \mu^2 \Delta N$ the anisotropy constant. These angles have been sketched in the bottom right panel of Figure 8-10. This equation is valid for a magnetization vector lying in the plane of the vector of the applied field and the easy axis. The origin of the anisotropy term here is purely shape anisotropy, as the material composing the nanoisland, permalloy, has negligible magnetocrystalline anisotropy.

The Stoner-Wohlfarth model predicts that, in a magnetization reversal process of an Ising-like magnetic nanoellipse, when a saturating external magnetic field is applied at an angle from the easy axis of the nanoellipse, the magnetic moment will rotate towards the applied field. Upon reduction of the applied external field towards zero field value the magnetic moment will rotate towards the easy axis of the nanoellipse and eventually, at zero field, the magnetic moment will be aligned with the easy axis. If the externally applied field is further reduced towards negative saturation values the magnetic moment will start moving away from the easy axis driven by the applied field and, at a certain point, the $\vec{\mu}$ vector undergoes a sudden jump to align parallel to the externally applied field. When negative saturation field values are reached the magnetic moment will align with the external field, finishing in this way the magnetization reversal process.

The magnetization reversal process of the nanoislands shown in Figure 8-9 has been analyzed by means of MOKE microscopy, using the region of interest tool. Besides the experimental analysis of the magnetization reversal, also micromagnetic simulations of this process have been performed by means of OOMMF in a single nanoisland with dimensions 425x170x13nm and 5nm cell size, smaller than the exchange length of Permalloy (5.3nm). A plot of the calculated hysteresis loops for different orientations of the external field can be observed in Figure 8-10, together with the recorded hysteresis loops in the pattern of Figure 8-9. By comparing the hysteresis loops calculated from the Stoner-Wohlfarth model with the simulated (by means of OOMMF) and the experimentally measured ones, it can be concluded that the coherent

magnetization reversal behavior is the one qualitatively observed in the nanoellipses studied here.

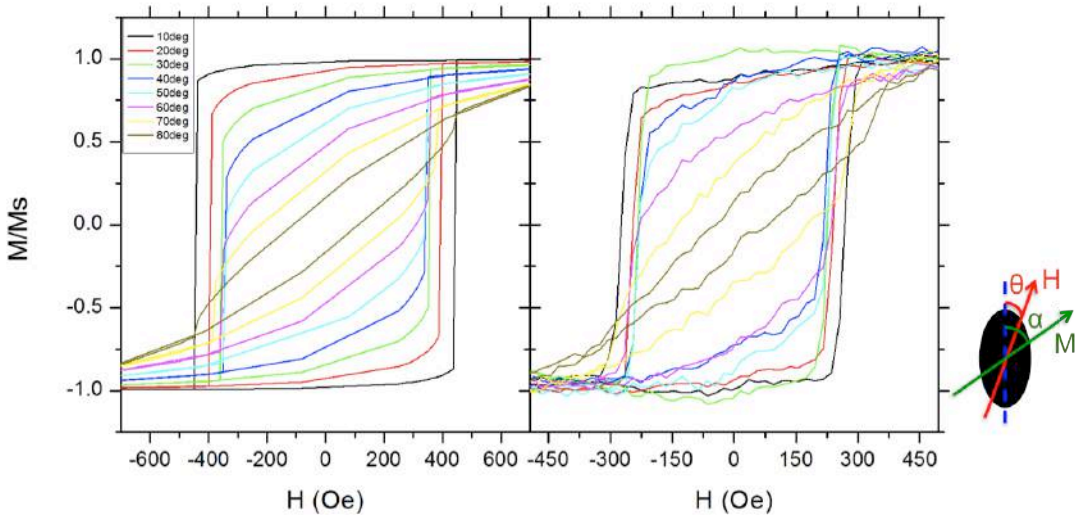

Figure 8-10: Calculated (left) and measured (right) hysteresis loops for the array of ferromagnetic nanoellipses shown in Figure 8-9 for external fields applied at angles varying from 0° to 80° away from the easy axis. The bottom right panel shows an sketch of the angles' orientation used in Eq.(8-1) of the Stoner-Wohlfarth model.

The magnetization reversal process of the nanoellipses forming the array shown in Figure 8-9 follows what is expected from the Stoner-Wohlfarth model. The switching field values (field values at which there is a discontinuous jump of the magnetization) decrease continuously from $\theta=0°$ to $\theta=45°$, when it takes its minimum value, and increase again from $\theta=45°$ to $\theta=90°$. The coercive field (the magnetic field at which the magnetization is zero) and the switching field have the same value when $0°\leq\theta\leq45°$, whereas when $45°<\theta\leq90°$ the coercive field is smaller than the switching field. Based on the qualitative agreement with the Stoner-Wohlfarth model, it can be concluded that the dominant magnetization reversal mechanism is coherent rotation, and the switching field values for the nanoislands studied here are not too high for the implementation of the experiment to be performed with the domain wall conduits and the nanoislands.

8.2.3. Effect of the DW pulse on nanoislands' magnetization

After revising the domain wall displacement processes in the planar magnetic conduit (with a curved section that serves as an injector for the domain wall into the conduit), and the magnetization reversal of nanoislands with the same size of the ones that will be placed in the proximities of the conduit, an analysis of the characteristics of the magnetic field pulses created by the domain wall is the next step. For that purpose, micromagnetic simulations have been performed by means of OOMMF, whose working principles are explained in Chapter 5 of this thesis.

Similar domain wall conduits to the ones presented in Figure 8-6 have been used in the simulations. The conduits have a width of 150nm and a thickness of 13nm, and a cell size of 5nm is used. The shape of the domain wall conduit reproduces that of Figure 8-6, with a curved section used to nucleate the transverse domain wall on it. The magnetic field sequence applied in the simulation follows exactly the one used in the experiment discussed previously in this chapter: a nucleating field $H_N=600\ Oe$ is applied at an angle $\theta=80°$ (as sketched in Figure 8-6), so that the domain wall is nucleated in a specific position of the curved section of the conduit, and afterwards a depinning field $H_d=150\ Oe$ is applied almost parallel (not perfectly parallel, in order to simulate a real experiment in which a perfect alignment is almost impossible) to the conduit, forcing the transverse domain wall nucleated in the previous field step to depin from its position, and displace towards the other end of the straight part of the conduit.

The domain wall conduit shown in Figure 8-6 has nanoellipses located in the proximities of its straight section, whose closer edges are located at a distance of 50nm from the domain wall conduit. Their dimensions are similar to the ones studied in the previous section: 425nm long, 170nm wide and 13nm thick. In order to analyze the effect of the stray field created by the domain wall on its neighboring nanoislands, the strength, spatial and temporal distribution, and time profile of the field pulse during the displacement have been analyzed with micromagnetic simulations. The analysis of the intensity and temporal shape of

the field pulse on the neighboring nanoellipses has been performed dividing the nanoellipse in three regions (lower, center, upper), as well as calculating the time-resolved average stray field magnitude (the average of the field intensity in a determined region at a given time) in each of them. The obtained results are shown in Figure 8-11, where the three regions in which the horizontal and vertical components of the field pulse have been analyzed are also sketched.

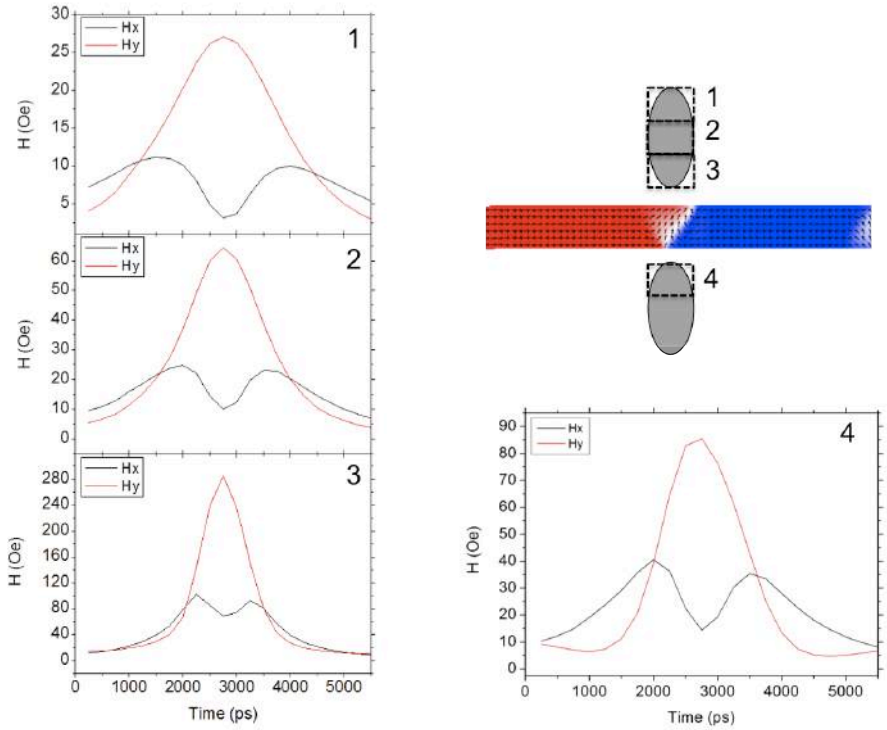

Figure 8-11: plots of the vertical (red curves) and horizontal (black curves) components of the stray field generated by a transverse domain wall, when passing through a nanostripe 150nm wide and 13nm thick in four different regions of nanoislands with dimensions 425x170x13nm³, placed at 50nm distance from the conduit, as sketched on the top right panel of the figure.

Each single point in the plots of Figure 8-11 is the average, at the corresponding time, of the magnetic field pulse intensity over the marked areas 1, 2, 3 and 4. An inspection of the plots of the stray field pulses displayed in Figure 8-11 shows a remarkable decay of the strength of the field pulses with the distance; at a distance from 50 to 190nm from the conduit (lower part of the neighboring nanoellipse) the peak of the vertical component of the average field pulse intensity in that region has a value of 285 Oe, whereas this peak intensity is reduced to 65 Oe at a distance from 190 to 330nm, and to less than 30 Oe at a distance from 330 to 475nm. This means that the vertical component of the

average stray field generated by the domain wall acting on the total surface of the nanoparticle is around 120 Oe when the nanoparticle is facing the side of the conduit in which the domain wall generates a stronger magnetic field (wide side of the domain wall). In the case of a nanoisland located at 50nm from the conduit, facing the narrow side of the domain wall (position 4 in Figure 8-11), the vertical component of the average stray field generated by the domain wall has a peak intensity of 80 Oe at a distance from 50 to 190nm, three times smaller than that sensed by a nanoisland placed in the opposite side of the conduit. It is remarkable that the field pulse has a non negligible horizontal component with its own time evolution.

A vector plot of the time evolution combining both components of the field pulse created by the transverse domain wall, acting on a nanoparticle with dimensions 425x170x13nm located 50nm away from the wide side of the domain wall, is presented in the top panel of Figure 8-12 together with the average vertical and horizontal components of the field pulse. It is interesting to note that the time profile of the field pulse exhibits a rotating magnetic field pulse vector, whose intensity is bigger when the horizontal component has a local minimum.

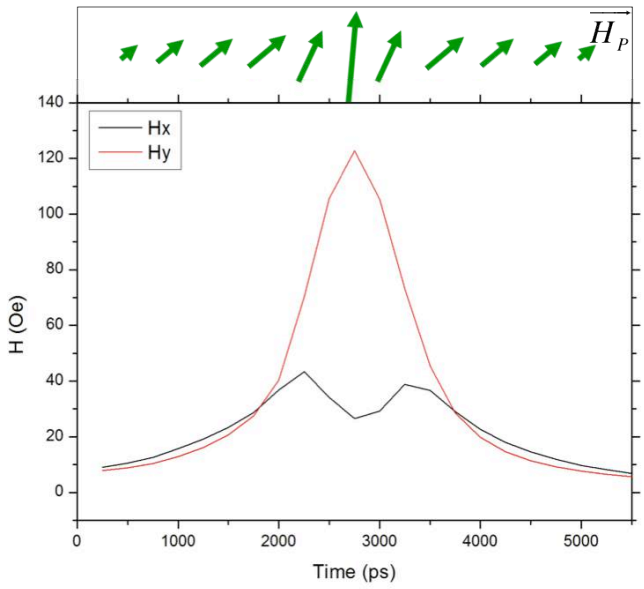

Figure 8-12: Horizontal (black curve) and vertical (red curve) components of the average intensity of the field pulse created by a transverse domain wall, when being displaced in a domain wall conduit 150nm wide and 13nm thick, in the space occupied by a nanoisland with dimensions 425x170x13nm located at a distance of 50nm from the conduit. The green vector plot at the top is the time evolution of the vector of the field pulse created by the domain wall that is propagating.

When analyzing the possibility to reverse the magnetization of a nanoellipse (dimensions 425x170x13nm^3) located in the proximities of a nanostripe through which a transverse domain wall is being displaced, it is not only the magnetic field pulses generated by the domain wall what affects the magnetization of the nanoellipse; the total external magnetic field $\overrightarrow{H_{TOT}} = \overrightarrow{H_D} + \overrightarrow{H_P}$ applied to depin the domain wall from the nucleation point also affects its magnetization. Therefore, these two sources of magnetic field interact with the magnetization of the nanoparticle: a uniform and constant magnetic field, necessary to depin the domain wall, and a time-varying (in intensity and direction, as observed in the vector plot in Figure 8-12) non-uniform magnetic field source given by the displacing transverse domain wall.

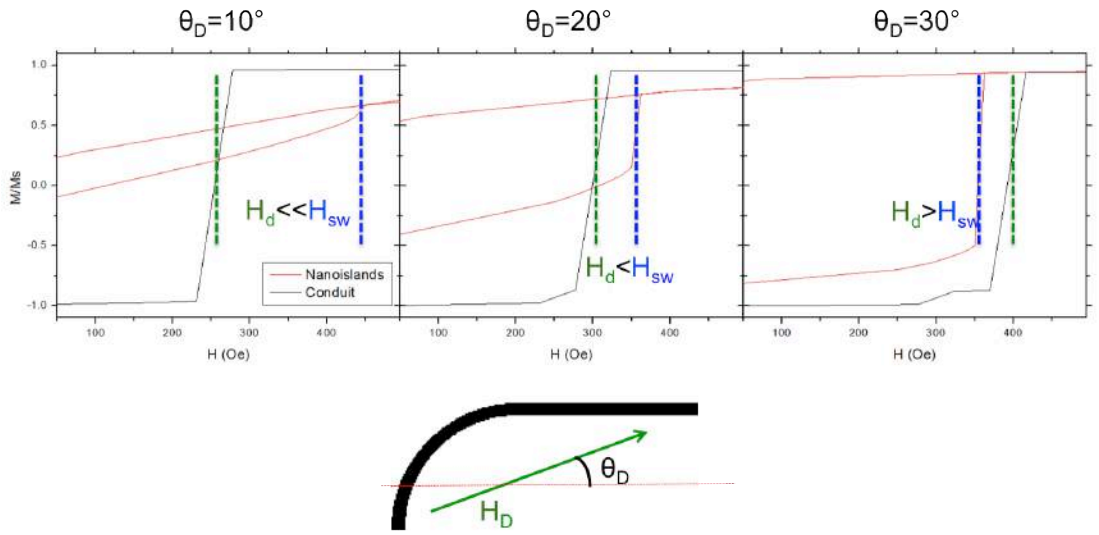

Figure 8-13: Simulations of the depinning event of the domain wall at angles θ=10°, θ=20° and θ=30° (black curves), compared to the switching fields of the nanoislands at these angles (red curves). The depinning fields of the domain walls and the switching fields of the nanoislands are marked in green and blue dotted lines, respectively.

The analysis of the depinning fields of the domain wall, when the domain wall is nucleated at an angle of 80° from the direction parallel to the conduit (see Figure 8-8) has been previously presented in this chapter. Micromagnetic simulations of the depinning event in that situation have also been performed. The depinning field changes with θ_D: bigger depinning fields are needed when the external field is applied at an increasing angle from the long axis of the conduit. The results of

the simulations of the depinning fields as a function of the angle at which the field is applied are shown in Figure 8-13.

Each of the three panels composing Figure 8-13 shows a zoomed-in region of the simulated hysteresis loops for the domain wall conduit (black curves), after nucleating a domain wall by applying a field at an angle of 80° (as sketched in the lower panel of Figure 8-8). The jump in the magnetization corresponds to the depinning event of the domain wall. Apart from the black curves, the superimposed red plots correspond to the zoomed-in region of the hysteresis loops of the nanoislands when the external field is applied at the angles sketched in the figure. These simulations show that the depinning field value increases with the angle at which the external field is applied, reproducing the same results obtained in experiments and presented previously in this chapter. Besides this information, the switching fields of the nanoislands and the depinning fields are compared in each case, observing a decrease in the difference of both field values when the angle at which the field is applied increases, up to a situation in which the depinning field is smaller than the switching field at θ=30°, which means that the nanoislands will reverse their magnetization before the domain wall depinning takes place.

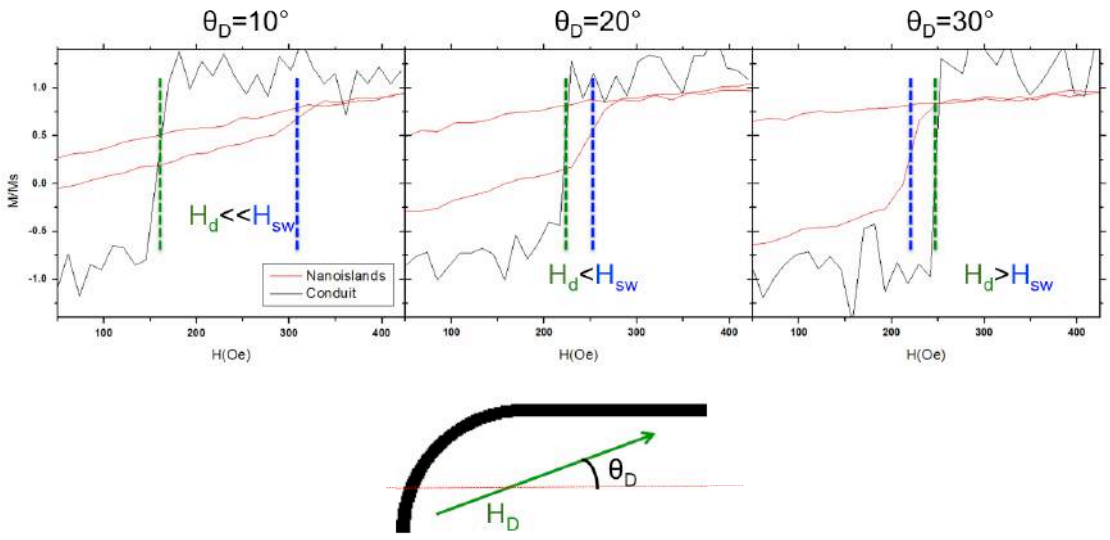

Figure 8-14: Zoomed-in regions of the hysteresis loops for the domain wall conduit after the domain wall has been nucleated (black) and nanoellipses (red) when the depinning field is applied at 10°, 20° and 30° from the parallel direction to the conduit. The jump in the domain wall conduit hysteresis loop corresponds to the depinning field. The depinning fields of the domain walls and the switching fields of the nanoislands are marked in green and blue dotted lines, respectively.

The comparison between the depinning fields of the domain wall and the switching fields of the nanoislands, when the external field is applied at different angles, has also been performed experimentally and is shown in Figure 8-14.

The simulations and experimental results on the domain wall depinning and switching fields of the nanoislands give similar results. Note the difference in magnetic field values at which the different events happen; even if the differences between the switching field and depinning field values are similar in the simulations and experiments in each case, the external field values at which these events take place are different in simulations and experiments. This is mainly due to the fact that the simulations show the results for perfect nanostructures, whereas the real nanostructures may present shape defects and variations.

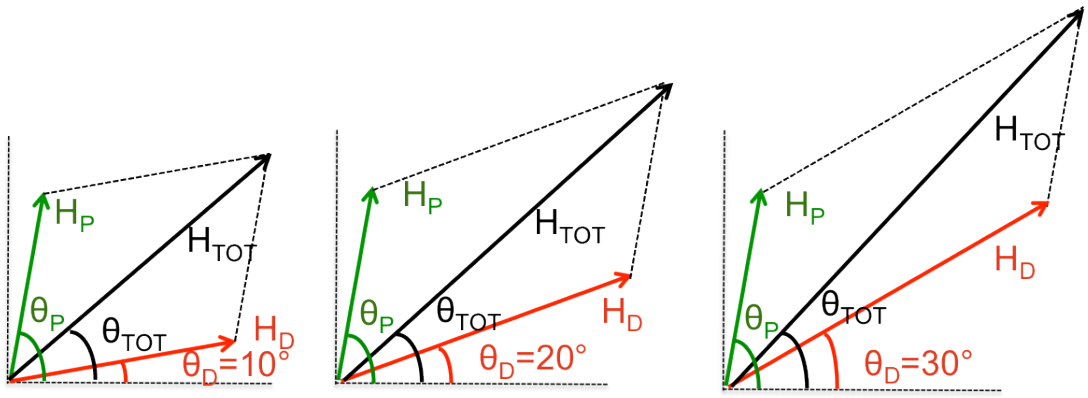

Figure 8-15: Vector representation of the total field (black) as a sum of the depinning field (red) and field pulse created by the domain wall (green) for the three different orientations of the depinning field studied.

Three different scenarios appear when analyzing the results shown in Figure 8-13, Figure 8-14 and Figure 8-15. The situation that would eventually lead to a magnetization reversal process in the nanoislands placed at a distance of 50nm from the conduit, corresponds to that in which the externally applied field used to depin the domain wall, added to the magnetic field pulse created by the displacing domain wall, is bigger than the switching field of the nanoislands. In the first scenario, when the external field is applied at θ_D=10°, the total field

vector acts at an angle θ_{TOT}=40° and has an intensity of 208 Oe. The switching field of the nanoislands at that angle is bigger than 208 Oe, so that the addition of the field pulse created by the domain wall to the applied depinning field would not be enough to reverse the magnetization of the nanoislands. In the second scenario, when the external field is applied at θ_D=20°, the total field vector acts at an angle of θ_{TOT}=43° and with an intensity of 248 Oe. In this case, the switching field of the nanoislands at that angle is around 235 Oe, and therefore the addition of the field pulse created by the domain wall to the externally applied field could end up in a magnetization reversal process of the neighboring nanoislands. The third scenario corresponds to the case in which the external field is applied at θ_D=30°. In this case, the depinning field intensity is strong enough to induce a magnetization reversal process in the nanoislands. They will reverse their magnetization before the depinning event takes place, so that the field pulse created by the domain wall would be irrelevant.

The three situations have been reproduced experimentally, and will be described in the next pages in this chapter. The first step, common to the three situations, is to apply a 'reset' field in order to nucleate the domain wall in the conduit: a magnetic field of 600 Oe is applied at an angle of 80° (as sketched in Figure 8-16) from the straight part of the conduit. The magnetic configuration of the domain wall conduit with the adjacent nanoislands can be observed in the MFM image shown in Figure 8-16. Note that below the conduit with the adjacent nanoislands there is an array of 30 nanoislands whose magnetization is not affected by the stray field created by the domain wall, which will be used as 'control' nanoislands: they are located far from the conduit so that the only field source affecting their magnetization is an externally applied field.

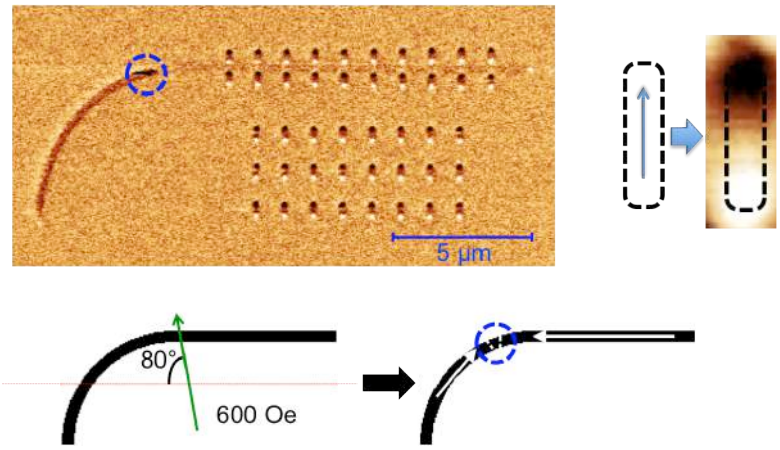

Figure 8-16: MFM image of the conduit with the nanoislands after applying a reset field of 600 Oe. The dotted blue circle denotes the position of the domain wall. The lower inset represents the applied magnetic field direction and the resulting magnetization configuration in the conduit after it. The inset on the right shows a MFM image of a single nanoisland magnetized downwards, in order to identify easily the magnetization configuration of the sample.

After applying the reset field, the nanoislands are magnetized upwards, but in order to check if the magnetic field pulses created by the domain wall affect the magnetization of the nanoislands they should be magnetized downwards (opposite to the direction of the magnetic field pulse). For this purpose, after the reset field the ellipses are magnetized downwards by applying an external field of 250 Oe at the same angle than the reset field but downwards, which leaves the magnetization in the domain wall conduit unaltered but the magnetization of the nanoislands is now pointing downwards. The last step is to apply the depinning field. This magnetic field sequence is sketched in the lower panel of each of the MFM figures (Figure 8-17, Figure 8-18 and Figure 8-19) that will be shown for each of the three situations discussed previously (Figure 8-13, Figure 8-14 and Figure 8-15).

In the first case, when the external field is applied at 10° off the horizontal (parallel to the conduit) it is necessary to apply a field of 160 Oe in order to depin the domain wall from the nucleation position. At the same time, the switching field of the nanoellipses in that case is around 310 Oe. The displacing domain wall creates an average magnetic field pulse in the nanoparticle that, added to the external field applied to depin the domain wall, is not strong enough to alter the magnetization configuration of the nanoparticle, which remains unaffected after the displacement of the domain wall. The resulting

magnetization in the sample after applying the aforementioned depinning field can be observed in Figure 8-17. The field sequence applied is sketched in the lower panel of the figure. After this field sequence is applied the magnetization of the nanoislands is not altered: all of them (the 'control' nanoislands far below from the conduit, and the ones located nearby) remain unaltered.

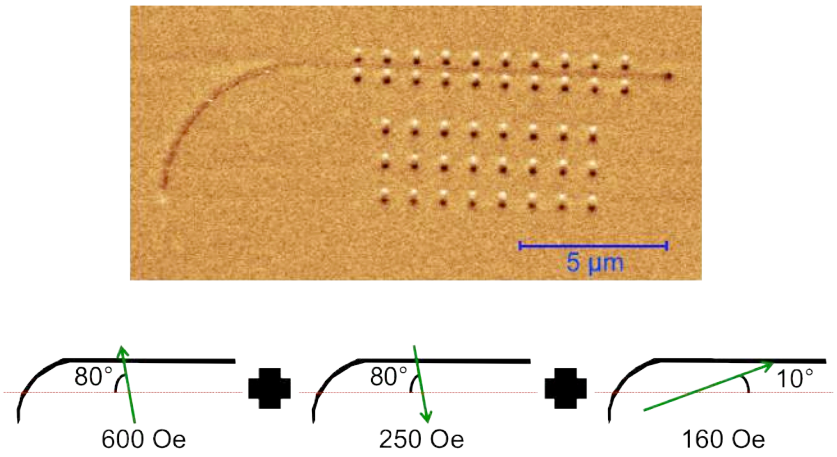

Figure 8-17: MFM image of the sample after applying the depinning field at 10°. The complete magnetic field sequence (domain wall nucleation, magnetization of the nanoislands and depinning field) is sketched in the lower panel.

The stray field generated by the uniformly magnetized neighboring nanoislands, when their magnetic moments are pointing towards the conduit, is not strong enough to pin the domain wall at that position, as observed both with micromagnetic simulations and when doing the experiment: after the depinning field was applied when θ_D=10°, where all the neighboring nanoislands above the conduit have their magnetization pointing downwards towards the conduit, the domain wall was never pinned at any position of the straight part of the conduit. Furthermore, when measuring the hysteresis loops of the domain wall conduits with the neighboring nanoislands pointing towards the conduit, the magnetization reversal takes place in a single-step, giving another evidence that there is no pinning event in the conduit due to the stray field of the nanoislands.

When the external field is applied at 20°, the depinning field value increases to 210 Oe. The average magnetic field pulse created by the transverse domain wall, added to the depinning field, has an intensity that is bigger than the switching field of the nanoislands at the angle at which the total field is applied (as

discussed previously). Therefore this situation could, in principle, lead to a magnetization reversal event on the neighboring nanoislands.

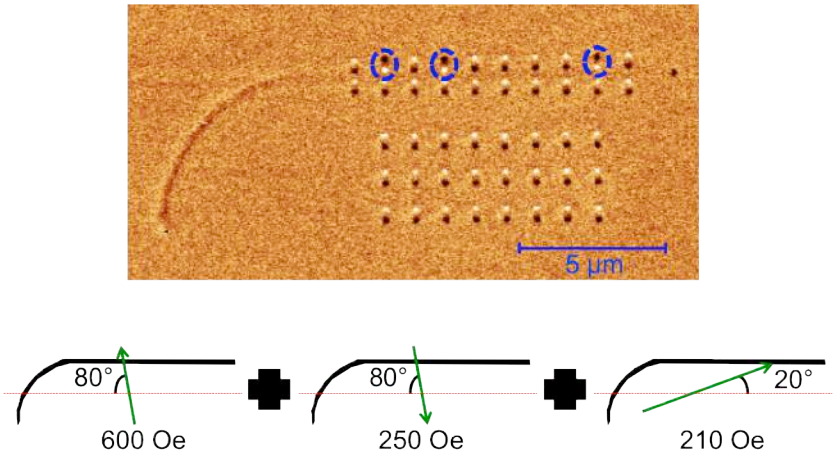

Figure 8-18: MFM image of the sample after applying the depinning field at 20°. The complete magnetic field sequence (domain wall nucleation, magnetization of the nanoislands and depinning field) is sketched in the lower panel. The blue dotted lines indicate the nanoislands that have reversed their magnetization after the domain wall has passed through the domain wall conduit.

The resulting magnetic force microscopy image of the conduit and nanoislands after the application of a depinning field at 20° is shown in Figure 8-18, with the applied magnetic field sequence in its lower panel. In that image it is observable that three nanoislands that are close to the upper side of domain wall conduit have reversed their magnetization, whereas none of the ones close to the lower side have reversed, as well as none of the 'control' nanoislands. Note that not all the nanoislands located in the upper side (where the stray field of the domain wall is stronger) have reversed their magnetization; this fact is probably due to intrinsic nanofabrication defects such as different dimensions for each nanoisland (leading to different switching fields) and defects or deformations of the domain wall conduit that reduce the strength of the stray field generated by the transverse domain wall.

Apart from the nanofabrication defects on the domain wall conduit that affect the displacement of the domain wall, it is well known that the domain wall shape can change during its displacement through a nanostripe [39, 40]. In the case presented here, due to the vertical component of the applied depinning field, the domain wall is not transformed from a transverse to a vortex wall, but the

transverse domain wall shape is distorted. This changes the shape and intensity of the time profile of the field pulse created by the domain wall. This effect, added to the intrinsic nanofabrication defects on the domain wall conduit, gives an oscillatory behavior to the transverse domain wall that leads to a situation in which the addition of the field pulse to the depinning field might not be enough to reverse the magnetization of the neighboring nanoislands during the whole displacement process of the domain wall. This adds more light into the fact that not all the neighboring nanoislands reverse their magnetization in the case when θ_D=20°.

Finally, if the external field is applied at 30° the minimum depinning field value will be 245 Oe. In this case the magnetization reversal process of the nanomagnets will occur independently from the depinning event of the domain wall, as the nanoellipses will have their magnetization reversed before the depinning of the domain wall occur.

This behavior can be observed in the magnetic force microscopy image shown in Figure 8-19, where the conduit and nanoislands have undergone the field sequence sketched in the lower panel of the figure, and after applying the depinning field of 245 Oe at an angle of 30° many of the nanoislands, both adjacent and far from the conduit, have reversed their magnetization. The fact that not all the nanoislands have reversed their magnetization can be attributed to the differences in the sizes of the nanoellipses and also to possible minor deviations from the perfect 30° angle and 245 Oe applied field in the experimental process.

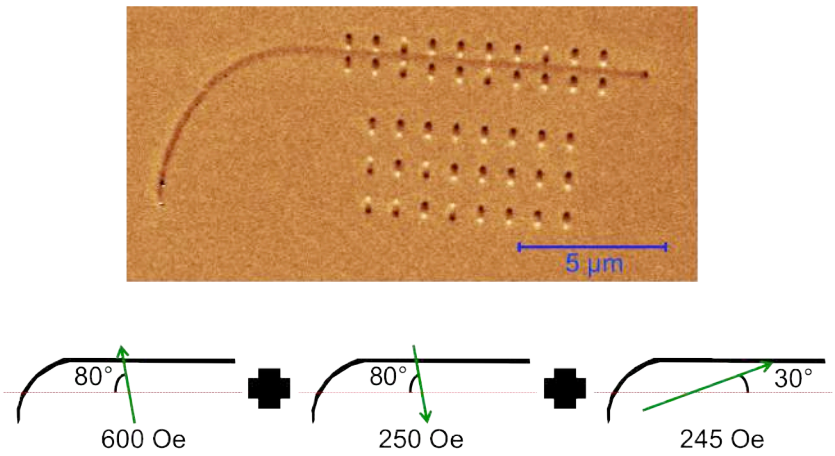

Figure 8-19: MFM image of the sample after applying the depinning field at 30°. The complete magnetic field sequence (domain wall nucleation, magnetization of the nanoislands and depinning field) is sketched in the lower panel.

8.3. Conclusions

In this chapter the effect of the magnetic field pulses generated by a transverse domain wall being displaced in a planar nanostripe on neighboring ferromagnetic nanoellipses has been analyzed. For this purpose, MOKE magnetometry and microscopy, together with magnetic force microscopy imaging tools have been used, supported by micromagnetic simulations.

In a first step, the magnetic behavior of planar domain wall conduits (nanostripes) has been investigated. Two different geometries for the part of the nanostripes were the domain wall is nucleated (i.e. injection pads) were proposed, nanofabricated and whose magnetic behavior analyzed: a rectangular injection pad, bigger than the nanostripe size, and a curved nanostripe with the same width than the straight part of the conduit. The second type of domain wall conduit has been chosen to inject and displace a transverse domain wall, mainly due to the fact that the geometry of the transverse domain wall can be controlled: the nucleation of the domain wall occurs with the wide part of the transverse domain wall pointing outwards from the curvature of the conduit, whereas this cannot be directly controlled with the rectangular injection pad. The nucleation and depinning magnetic field values for the transverse domain walls have been defined in the proposed domain wall conduits, and these two

events take place in a controlled and reproducible fashion in the nanofabricated nanostripes.

The magnetization reversal process of arrays of ferromagnetic nanoellipses has also been analyzed, both theoretical and experimentally, studying the dependence of the switching fields of the nanoellipses with the direction of the external applied field. A Stoner-Wohlfarth-like magnetic behavior of the nanoellipses has been found to occur in the array of non-interacting ferromagnetic nanoislands fabricated by means of electron beam lithography. The nanoellipses with dimensions 425x170x13nm3 have an Ising-like bistable behavior of the magnetization, with single-domain magnetization states at remanence that switch from positive to negative magnetization states via coherent rotation of the magnetic moments at well-defined switching fields.

The temporal profile and strength of the magnetic field pulses created by the transverse domain wall in its proximities has been analyzed. The time evolution of the average horizontal and vertical components of the field pulses has been calculated in different regions of the adjacent space to the conduit, finding that their intensity decays strongly with the distance at which the pulse is sensed. The effect of this stray field on nanoellipses placed at 50nm from the domain wall conduit is not enough to reverse their magnetization even if the externally applied domain wall depinning field, which also affects the magnetization of the nanoellipses, is added to the magnetic field pulse acting on the nanoellipses at an angle of 10° from the domain wall conduit, favouring the magnetization reversal process on the nanoellipses. When the depinning field is applied at 20° the addition of this external field to the magnetic field pulse generated by the domain wall might be sufficient to trigger a magnetization reversal process in the neighboring nanoellipses, whereas nanoellipses located far away subjected to the same external fields do not reverse their magnetization. Finally, when the depinning field is applied at 30° the depinning event of the domain wall occurs at a field value that is bigger than the switching field of the nanoellipses, which reverse their magnetization without the need of the magnetic field pulse generated by the domain wall.

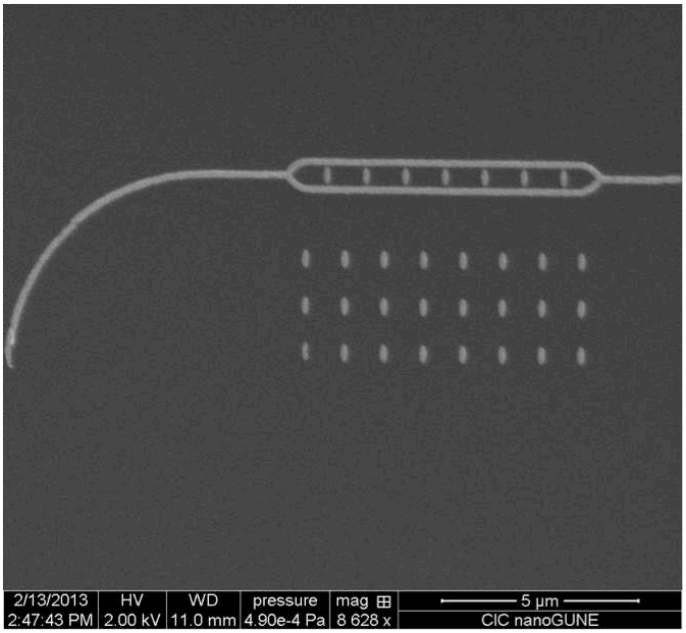

Figure 8-20: domain wall conduit with a bifurcation of the straight part of the nanostripe into two sections through which the domain walls in each conduit travel parallel, generating a more intense magnetic field pulse between the two straight sections of the nanostripe.

As an outlook, domain wall conduits with different geometries can be studied, as that proposed in Figure 8-20, leading to a more intense total magnetic field pulse in localized neighboring regions.

8.4. References

[1] Y. Acremann, *et al., Science* **290**, 492 (2000)

[2] S. B. Choe, Y. Acremann, A. Scholl, A. Bauer, A. Doran, J. Stöhr, and H. A. Padmore, *Science* **304**, 420 (2004)

[3] K. Mackay, M. Bonfim, D. Givord, and A. Fontaine, *J. Appl. Phys*. **87**, 1996 (2000)

[4] B. C. Choi, M. Belov, W. K. Hiebert, G. E. Ballentine, and M. R. Freeman, *Phys. Rev. Lett.* **86**, 728 (2001)

[5] M. Bonfim, G. Ghiringhelli, F. Montagne, S. Pizzini, N. B. Brookes, F. Petroff, J. Vogel, J. Camarero, and A. Fontane, *Phys. Rev. Lett*. **86**, 3646 (2001)

[6] D. Atkinson, D. A. Allwood, M. D. Cooke, and R. P. Cowburn, *J. Phys. D: Appl. Phys*. **34**, 3019 (2001)

[7] M. R. Freeman and J. F. Smyth*, J. Appl. Phys*. **79**, 5898 (1996).

[8] T. J. Silva, C. S. Lee, T. M. Crawford, and C. T. Rogers, *J. Appl. Phys*. **85**, 7849 (1999)

[9] W. K. Hiebert, A. Stankiewicz, and M. R. Freeman, *Phys. Rev. Lett*. **79**, 1134 (1997).

[10] C. M. Schneider, A. Kuksov, A. Krasyuk, A. Oelsner, D. Neeb, S. A. Nepijko, G. Schönhense, I. Mönch, R. Kaltofen, J. Morais, C. de Nadaï, and N. B. Brookes, *Appl. Phys. Lett.* **85**, 2562 (2004).

[11] A. Y. Ellezzabi, M. R. Freeman, and M. Johnson, *Phys. Rev. Lett*. **77**, 3220 (1996)

[12] S. Zhang, P. M. Levy, and A. Fert, *Phys. Rev. Lett*. **88**, 236601 (2002)

[13] G. Tatara and K. Kohno, *Phys. Rev. Lett*. **92**, 086601 (2004)

[14] S. E. Barnes and S. Maekawa, *Phys. Rev. Lett*. **95**, 107204 (2005)

[15] E. Martinez, L. Lopez-Diaz, L. Torres, C. Tristan, and O. Alejos, *Phys. Rev. B* **75**, 174409 (2007)

[16] A. Thiaville, Y. Nakatani, J. Miltat, and N. Vernier, *J. Appl. Phys*. **95**, 7049 (2004)

[17] J. Shiabata, G. Tatara, H. Hohno, and Y. Otani*, IEEE Trans. Magn*. **41**, 2595 (2005)

[18] Z. Li, J. He, and S. Zhang, *J. Appl. Phys*. **99**, 08Q702 (2006)

[19] Peng-Bin He, X. C. Xie, and W. M. Liu, *Phys. Rev. B* **72**, 172411 (2005)

[20] D. Ravelosona, D. Lacour, J. A. Katine, B. D. Terris, and C. Chappert, *Phys. Rev. Lett.* **95**, 117203 (2005).

[21] T. Ono, H. Miyajima, K. Shigeto, K. Mibu, N. Hosoito, and T. Shinjo, *Science* **284**, 468 (1999)

[22] D. A. Allwood, Gang Xiong, M. D. Cooke, C. C. Faulkner, D. Atkinson, N. Vernier, and R. P. Cowburn, *Science* **296**, 2003 (2002)

[23] G. S. D. Beach, C. Nistor, C. Knutson, M. Tsoi, and J. L. Erskine, *Nat. Mater*. **4**, 741 (2005)

[24] D. Atkinson, D. A. Allwood, G. Xiong, M. D. Cooke, and R. P. Cowburn, *Nat.*

Mater. **2**, 85 (2003)

[25] M. Laufenberg, D. Backes, W. Buhrer, M. Klaui, U. Rudiger, C. A. F. Vaz, J. A. C. Bland, L. J. Heyderman, F. Nolting, S. Cherifi, A. Locatelli, R. Belkhon, S. Heun, and E. Bauer, *Appl. Phys. Lett*. **88**, 052507 (2006)

[26] A. Yamaguchi, T. Ono, S. Nasu, K. Miyake, K. Mibu, and T. Shinjo, *Phys. Rev. Lett*. **92**, 077205 (2004)

[27] T. Shigeto, T. Shinjo, and T. Ono, *Appl. Phys. Lett*. **75**, 2815 (1999)

[28] R. P. Cowburn,D. A. Allwood, G. Xiong, and M. D. Cooke, *J. Appl. Phys*. **91**, 6949 (2002)

[29] J. Rothman, M. Kläui, L. Lopez-Diaz, C. A. F. Vaz, A. Bleloch, J. A. C. Bland, Z. Cui, and R. Speaks, *Phys. Rev. Lett*. **86**, 1098 (2001).

[30] M. Kläui, J. Rotthman, L. Lopez-Diaz, C. A. F. Vaz, J. A. C. Bland, and Z. Cui, *Appl. Phys. Lett*. **78**, 3268 (2001)

[31] S. S. P. Parkin, U.S. Patent No. 6,834,005 (21 December 2004)

[32] D. A. Allwood, G. Xiong, C. C. Faulkner, D. Atkinson, D. Petit, and R. P. Cowburn, *Science* **309**, 1688 (2005)

[33] M. Donolato, M. Gobbi, P. Vavassori, M. Leone, M. Cantoni, V. Metlushko, B. Ilic, M. Zhang, S. X. Wang and R. Bertacco, *Nanotechnology* **20**, 385501 (2009)

[34] M. Donolato, P. Vavassori, M. Gobbi, M. Deryabina, M. F. Hansen, V. Metlushko, B. Ilic, M. Cantoni, D. Petti, S. Brivio and R. Bertacco, *Advanced Materials* **22** (24), 2706-2710 (2010)

[35] M. Donolato, F. Lofink, S. Hankemeier, J. M. Porro, H. P. Oepen and P. Vavassori, *J. Appl. Phys*. **111**, 07B336 (2012)

[36] M. Donolato, C. Tollan, J. M. Porro, A. Berger and P. Vavassori, *Advanced Materials* **25** (4), 623-629 (2013)

[37] E. R. Lewis, D. Petit, L. Thevenard, A. V. Jausovec, L. O'Brien, D. E. Read and R. P. Cowburn*, Appl. Phys. Lett*. **95**, 152505 (2009)

[38] E. C. Stoner and E. P. Wohlfarth, Philosopical *Transactions of the Royal Society A: Mathematical, Physical and Engineering Sciences* **240**, 599 (1948)

[39] M. Hayashi, L. Tomas, C. Rettner, R. Moriya, and S. S. P. Parkin, *Nat. Phys*. **3**, 21-25 (2007)

[40] A. Bisig *et al.*, *Nat. Comm*. **4**, 2328 (2013)

9. Conclusions and outlook

In general, this thesis deals with the tuning of magnetic dipolar interactions in ferromagnetic samples artificially nanostructured and their exploitation for addressing a variety of fundamental aspects of magnetism. For this purpose, high quality magnetic nanostructures have been fabricated by means of electron-beam lithography. Hereby, a well-defined and controlled process for the nanofabrication of periodic magnetic nanostructures with sub-50nm gaps between them, in a fully reproducible fashion, has been developed, pushing to the limit the capabilities of the electron-beam lithography tool. The acquired advanced control and knowledge on this lithography technique have served to fabricate all the nanostructures issue of study in the present thesis.

The role and utilization of magnetic dipolar interactions in nanostructured samples have been investigated in three different cases: i) tuning of the magnetization reversal process in asymmetrically coupled nanomagnets, via magnetostatic dipolar interactions; ii) accommodation of frustration in arrays of dipolarly-coupled nanomagnets; iii) utilization of domain wall conduits to generate ultrafast magnetic field pulses that induce magnetization reversal events in neighboring nanomagnets.

Concerning case i), this thesis reports on the analysis of the magnetization reversal process of an array of interacting ferromagnetic nanoislands, which are magnetically coupled via spatially inhomogeneous and asymmetric magnetostatic dipolar interactions. The magnetization reversal process has been found to change dramatically depending on the orientation of the externally applied field, due to the asymmetric magnetostatic dipolar field coupling and the dynamic processes through which the magnetization reversal of the nanomagnets takes place. It has been demonstrated that the presence of the asymmetric dipolar interactions can be used to induce and observe at remanence non-uniform magnetization states, which are energetically extremely unfavored and do not occur under the action of an uniform magnetic field. These non-

uniform magnetization states have been imaged at remanence by means of magnetic force microscopy in nanomagnets with different lateral dimensions and thicknesses.

About case ii), this thesis reports on the accommodation of frustration in arrays of nanomagnets forming so-called artificial spin ice structures. A novel demagnetizing protocol involving thermalization of the sample has been proposed and studied in order to achieve a better ground-state ordering than what has been so far achieved in literature. For this purpose, ferromagnetic-superparamagnetic-paramagnetic phase transitions have been induced in the artificial spin ice samples. These transitions allow the magnetic moments of the nanoislands to arrange in such a way that the magnetization state of the artificial spin-ice sample is close to a full ground-state ordering, which has not been reported in literature yet.

This thermal demagnetizing protocol in artificial spin-ice samples opens a new pathway to verify predictions of the many theoretical modeling efforts available in literature. Furthermore, the parameters of the cooling process through the Curie and Blocking temperatures can be varied at will, exploring in this way the role of disorder and entropy in presence of frustration. Another outlook is the study of the formation of excitation lines that separate the long-range ground state areas observed in the experiments and predicted by theory, whose nucleation and subsequent evolution are expected to be conceptually similar to the formation and propagation of magnetic monopole excitations and Dirac strings.

Finally, concerning to case iii), this thesis deals with the study of the effect of the magnetic field pulses generated by a transverse domain wall being displaced in a planar nanostripe on neighboring ferromagnetic nanoellipses. Different domain wall conduit shapes have been studied and scrutinized in order to achieve fully controlled domain wall nucleation and depinning processes. At the same time, the magnetization reversal process of arrays of ferromagnetic nanoellipses has

been analyzed, studying the dependence of the switching fields of the nanoellipses with the direction of the external applied field.

The temporal profile and strength of the magnetic field pulses created by the transverse domain wall during its displacement over the conduit has been analyzed in detail. The effect of such field pulses on nanoellipses placed at 50nm from the domain wall conduit has been studied, finding specific situations in which a field pulse assisted magnetization reversal is observed in neighboring nanoellipses. Extensions on this work may lead, for example, to the fabrication of domain wall conduits with more complex shapes, where the combined displacement of several domain walls can be used to increase the field pulse intensity as well as for shaping the field pulse, beyond what was achieved using simply shaped conduits.

10. List of publications

- J.M. Porro, A.Berger, P.Vavassori, *"Inducing magnetization reversal processes in nanomagnets by ultrafast magnetic field pulses created by transverse domain walls"*, Manuscript in preparation

- J.M. Porro, A.Berger, V.Metlushko, P.Vavassori, *"Tailoring the magnetization reversal in nanomagnets via asymmetric dipolar couplings"*, Manuscript in preparation

- T.V.A.G de Oliveira, M. Gobbi, J.M. Porro, L.E. Hueso, A.M. Bittner, *"Charge and spin transport in PEDOT:PSS nanoscale lateral devices",* Nanotechnology ***24*** 475201 (2013)

- E. Nikulina, O. Idigoras, J.M. Porro, P. Vavassori, A. Chuvilin and A. Berger, *"Origin and control of magnetic exchange coupling in between focused electron beam deposited cobalt nanostructures",* Applied Physics Letters **103** 123112(2013)

- J.M.Porro, A.Bedoya-Pinto, A.Berger, P.Vavassori, *"Exploring thermally-induced states in square artificial spin-ice arrays",* New Journal of Physics **15** 055012 (2013)

- M.Donolato, C.Tollan, J.M.Porro, A.Berger, P.Vavassori, *"Flexible and stretchable polymers with embedded magnetic nanostructures"*, Advanced Materials ***25*** 623-629 (2012)

- J.M. Porro, A.Berger, M.Grimsditch, V.Metlushko, B.Ilic, P.Vavassori, *"Effect of spatially asymmetric dipolar interactions in the magnetization reversal of closely-spaced ferromagnetic nanoisland arrays",* Journal of Applied Physics **111**, 07B913 (2012)

- M.Donolato, F.Lofink, S.Hankemeier, J.M.Porro, H.P.Oepen, P.Vavassori, *"Characterization of domain wall based traps for magnetic beads separation",* Journal of Applied Physics **111**, 07B336 (2012)

- O.Idigoras, A.K.Suszka, P.Vavassori, P.Landeros, J.M.Porro, A.Berger, *"Collapse of hard axes behaviour in uniaxial Co films",* Physical Review B **84**, 132403 (2011)

- D. Tripathy, P. Vavassori, J.M. Porro, A. Adeyeye, N. Singh, *"Magnetization reversal and anisotropic magnetoresistance behavior in bicomponent antidot nanostructures",* Applied Physics Letters **97**, 042512 (2010)

- O. Idigoras, P. Vavassori, J.M. Porro, A. Berger, *"Kerr microscopy study of magnetization reversal in uniaxial Co-films",* Journal of Magnetism and Magnetic Materials **322**, L57-L60 (2010)

11. Acknowledgements

First of all, I would really like to express my gratitude to Prof. Paolo Vavassori, for being a patient supervisor, helping me throughout all these years in the nanomagnetism lab, and pushing me to the final goal of writing this thesis. I owe him everything I know about magnetism and many of the different experimental techniques that I learnt during my stay in nanoGUNE. I am especially thankful to Dr. Andreas Berger, for giving me the opportunity to join the nanomagnetism group since its very beginning, and for the many stimulating discussions we had about my work. He has always been available to give his advices and suggestions whenever I required them.

I would also like to thank Prof. Vitali Metlushko for hosting me in his laboratory in the University of Illinois at Chicago, where I learnt some of the basics on the electron-beam lithography technique. Many thanks to Dr. Marcos Grimsditch for all the scientific discussions we had during his stay in the nanomagnetism group, and for helping me with the MOKE magnetometry techniquein the laboratory.

This thesis would not have come to an end without the great support of all the nanomagnetism group members with whom I have been lucky to share great moments during my stay at nanoGUNE. Their support has been essential to finish the work presented here. I am very thankful to all of them: Olatz, with whom I started this scientific adventure, has always been by my side helping me with any problem or doubt I had. The postdocs Ondrej, Ania, Marco Donolato, Ananda and Juanito, who assisted me stimulating my scientific thinking with uncountable discussions. Cesar, the technician, the 'do-it-all' man, always ready to help in the laboratory. Jon Ander, Andrea, Lorenzo, Nicolo, thanks for your friendship and support in the good and bad moments, both inside and outside the labs.

Many thanks also for the present and past colleagues here in nanoGUNE, making it so easy to work in this nice place, and particularly to Raúl Zazpe: these afternoons in Gros helped me to overcome many issues, both personal and laboratory related: eskerrik asko benetan. And also Marco Gobbi, who was

always ready to help and made my life easier during my stay in Donostia. Thanks also to Gorka Pazos, Gorka Arregi and Ralph Gay for their help with the laboratory, informatics and cleanroom equipment.

I would like to thank Prof. Txema Pitarke for the opportunity to work and carry out my experiments at CIC nanoGUNE Consolider. I acknowledge the financial support of my PhD studies from the "Programa de Formación de Personal Investigador" promoted by the Department of Education, Universities and Research of the Basque Government. I also acknowledge the financing from CIC nanoGUNE Consolider during the first year of my PhD.

Eskerrik asko nanoguneko kide guztioi, giro ezinhobean pasatu ditugun momentuak beti izango ditut gogoan. Tesiaren ibilbide guztia elkarrekin egin dugunez zuen laguntza, behar izan dudanean, maiz prestatu didazuelako. Eta tesiaren apartez, ere lagundu didazue hainbeste maitatzen dudan hizkuntz eder hau ikasten eta hobetzen urte hauetan zehar: hau ere ordainezina da. Benetan, mila esker guztioi.

Muchísimas gracias a mis amigos, mi cuadrilla, sin los cuales todo esto nunca habría sido posible. Ellos han estado siempre ahí cuando las cosas se torcían: Rocío, Jona, Jagoba, Plunkett, Nelson, Josu, Edu, Albar, Lander, Güemes, Aitz…y un largo etcétera: gracias a todos.

Cómo no, con el amparo incondicional de mi familia, mis padres Antonio y Mª Luisa y mi hermana Mercedes, el trabajo que ha supuesto hacer esta tésis ha sido muchísimo más llevadero . Vosotros me infundasteis la educación, la ética y el rigor que guían mi vida. Sin vosotros todo esto carecería de sentido.

Por ultimo, agradecer todo su apoyo a una persona muy especial que he conocido en el ultimo tramo de esta aventura. Contigo a mi lado todo ha sido mucho más fácil. Gracias por todos estos momentos que hemos pasado juntos, por las desconexiones más que necesarias, y por todos los momentos que vendrán de ahora en adelante. Muchísimas gracias, Aintzane.